Development of antimony-containing catalysts and semiconductors for (photo)electrochemical fuel production

By

Taylor A. Evans

A dissertation submitted in partial fulfillment of

the requirements for the degree of

Doctor of Philosophy

(Chemistry)

at the

UNIVERSITY OF WISCONSIN-MADISON

2020

Date of final oral examination: 7/28/2020

The dissertation is approved by the following members of the Final Oral Committee:

Kyoung-Shin Choi, Professor, Chemistry
Robert Hamers, Professor, Chemistry
Ive Hermans, Professor, Chemistry
John Berry, Professor, Chemistry

Abstract

The development of renewable and environmentally friendly processes to generate fuels and chemicals necessary for modern human society is paramount as the continued consumption of finite fossil fuels is felt environmentally and economically. Using renewably sourced electricity, electrochemistry can both store energy in chemical bonds for use as a fuel, such as hydrogen, as well as synthesize commodity chemicals that are precursors to a wide array of modern products, such as ammonia. At the heart of these electrochemical systems are electrode materials that must fulfill three key requirements. They must be robust enough to survive the potentially harsh conditions of a target reaction for long periods of time, active enough to drive the target reaction to completion at a reasonable rate and are not prohibitively expensive. Many materials have been investigated for a wide array of renewable energy applications to meet the above requirements; however, many modern systems still rely upon expensive noble metal catalysts to achieve reasonable rates and long catalyst lifespans, limiting the growth and sustainability of renewable energy development. This necessitates the cultivation and investigation of new materials using elements and compounds that have not been previously studied for a particular process.

Antimony (Sb), a p-block semi metal, is a relatively under-studied element for use in electrochemical systems, stemming from the difficulty in working with an element that evaporates before it melts and can form a volatile gas in a reducing environment. However, its position as a semi-metal, with both properties of non-metals like selenium and phosphorous, as well as metallic properties like iron or cobalt, leads to a rich array of potential chemistry that can be investigated for use as materials in sustainable electrochemical systems. The work reported herein is focused on the investigation of Sb containing compounds as water oxidation catalysts in acidic media,

quaternary metal oxides for photoelectrochemical water splitting, and nitrogen reduction catalysts for electrochemical ammonia synthesis.

Acknowledgements

For me, graduate school has been the most difficult part of my life so far with many twists, turns, uphill slogs and downhill sprints. Which is why I am eternally grateful to those that have supported me during my time in graduate school. There are many people who have been there for me in a tremendous variety of ways, however, I would like to specifically acknowledge several different groups of them for their outstanding support during my time in graduate school.

My mother, Victoria, and my two younger sisters, Brooke and Morgan, may now all live in different states across the country, but they have always been there for me whether it be a text to ask how I am doing, a short visit over the weekend, or us seeing each other over the holidays. Without their support I may have not even gone to graduate school. I would especially like to thank my mother for supporting me throughout my entire education and always being there at my highest highs and lowest lows. Thank you Mom, I could not have done it without you. I also wish to give thanks to Ashley Luehrs for all the love and support she has given me during some of the hardest times I have gone through in graduate school. Thank you for being there for me and I hope to continue to share my life's journey with you in the future.

I would also like to thank my numerous peers who provided daily healthy social interactions and support throughout graduate school. In particular, I would like to thank Garrett Wheeler who was always happy to chat about whatever new problem I had run into in lab or the latest video games we were both playing. I still recall us spending maybe too much time chatting about the latest Pokemon game we happened to be playing. I also greatly enjoyed the Food Cart Fridays that he coordinated almost every Friday; they were a great way to separate myself from work but still get to hang out with coworkers in a less formal setting every week. After Garrett graduated in 2018, Ann Lindberg and I continued the tradition of going out for lunch every Friday

to take a short break from work and chat about how we both were doing, whether it be about our research or how our lives in general were going. Most importantly, I would like to thank Chris Papa, who graduated the year I joined, for leaving me a sunny lab bench to do science at and a nice alcove desk to work from. Besides my coworkers, there were many others that helped and supported me throughout my time in graduate school. The many members of the chemistry department staff that provided guidance, let me hold informational interviews with them, said hello every morning in the hallway, and just chatted about their lives with me really helped to make me feel at home. Thank you Jeff, Bruce, Cheri, Arietta, Desiree, Matt, Heike, Ilia, Blaise, Steve, Mike, Sue, and many others!

But even with all the support of those above, I could not have made it through graduate school without my research advisor Kyoung-Shin Choi. She has been patient, considerate, and provided weekly guidance on how to become a better scientist. For that I am eternally grateful and believe that not only have I matured as a scientist because of her thoughtful guidance, but also as a person. Thank you Kyoung-Shin, I hope to stay in contact with you in the coming years!

Table of Contents

Chapter One: What can be done with antimony?

1.1 Introduction

The planet Earth is an incredible place. It is the only known planet that can sustain life as we know it and has a tremendous amount of diversity in its living organic creatures and non-living geological features. However, this diversity is relatively delicate and the rapid growth of humanity has caused unintended side effects upon the environment of the wonderful blue marble we call home. As these environmental effects of human expansion become more and more prevalent, there are many people who seek to live a more sustainable and less environmentally taxing lifestyle by taking actions like recycling, using less wasteful products, driving electric cars, etc. For me, the desire to contribute to a more sustainable future has led me down the path of scientific research, in particular to the field of materials development for use in renewable energy applications. The primary goal of scientific research is to help people understand the past, live safely in the present, and protect the future. This illustrates the importance of sharing what scientists actually discover and that everyone should be able to understand the work done by scientists. I, therefore, appreciate the assistance and directive of the Wisconsin Initiative for Science Literacy at the University of Wisconsin-Madison during the writing of this chapter meant for non-scientific audiences.

Before we get into how the element antimony fits into my research, let us first check out the element itself. Looking at the periodic table, we find antimony in a relatively quiet neighborhood, with a few well-known neighbors like lead and tin, in the lower right region of the table (**Figure 1**). We can notice that the chemical symbol for antimony (Sb) does not follow the typical method of naming that we see in other elements like carbon (C) and hydrogen (H) that use the first (or first two) letter(s) of their full names as their chemical symbol shorthand. The letters "Sb" actually originate from the Latin name for antimony, "stibium." Several other elements have this method of naming including more well-known elements like iron (Fe, ferrum), lead (Pb,

plumbum), and gold (Au, aurum). Therefore, so we don't have to spell out "antimony" every time I want to mention the element, I will use the shorthand "Sb" instead.

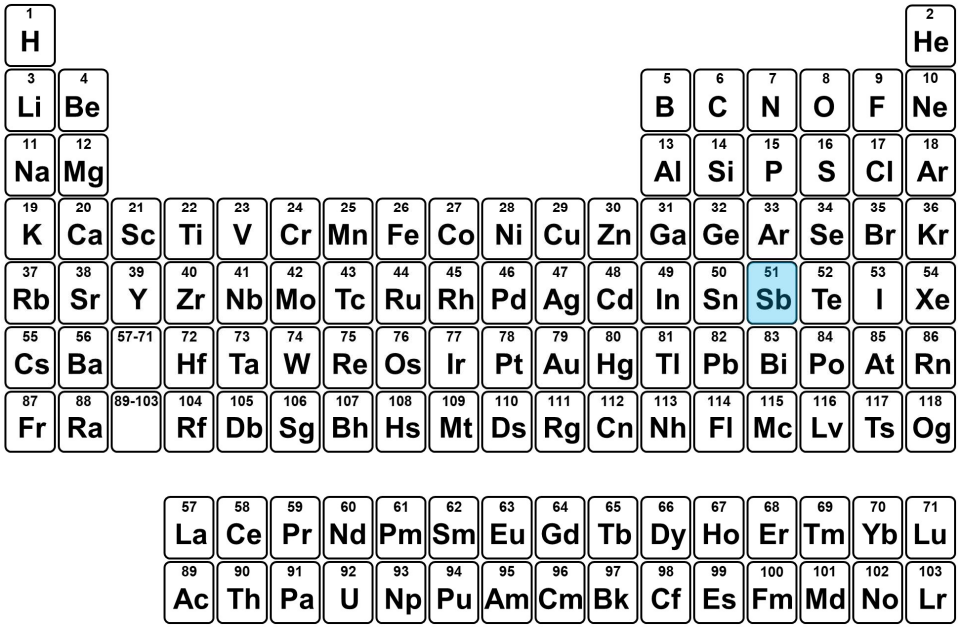

Figure 1. The periodic table of elements with antimony (Sb) highlighted in blue.

Sb as a pure element is a semi-metal, meaning it acts somewhere between a metal, like iron, and a non-metal, like sulfur. It can conduct electricity like a metal, but also melts and evaporates at relatively low temperatures like a non-metal. This gives it unique properties but also makes it more challenging to work with as you cannot treat it wholly as a metal or wholly as a non-metal. This is part of the reason Sb is relatively unexplored as a material or part of a material for modern applications. That doesn't mean it isn't used for some things though! It has a few relatively niche uses including as an alloy with lead in lead acid batteries in cars and as a part of flame retardants in clothing, children's toys, and car seat covers.

Because of this relative obscurity, I didn't even think about Sb when I entered graduate school. By happenstance, as a second-year graduate student in 2016, I worked on a project using Sb, although this initial project did not develop enough to be included within my thesis. However,

I was intrigued by this element I had heard almost nothing about and wondered what else I could do with it. Over the next couple of years and working with my research advisor, Professor Kyoung-Shin Choi, we developed a series of projects to investigate Sb and Sb-containing compounds for a variety of renewable energy applications. This thesis is the result of that work.

The primary tool I used to synthesize and investigate the Sb materials in the following sections was electrochemistry. Electrochemistry can be thought of as chemistry that is done with electricity, and you likely come into contact with a material made by it or one that uses it many times a day! For example, when someone says "chrome-plating" for their tire rims, what they are referring to is the process of electrochemically plating chromium (the shiny metal) onto the tire-rim to protect it. Many important metals for our modern society, like copper and aluminum, are purified using electrochemistry and every single battery in a laptop, phone, pacemaker, and hearing aid relies upon electrochemistry to function.

The heart of electrochemistry is the electrochemical cell which contains several important components that are required for the cell to function (**Figure 2**), kind of like how an animal or plant cell has several parts that are required for them to function. Every electrochemical cell contains two electrodes, an anode and cathode. These electrodes sit inside a conductive solution composed of water and ions dissolved in the water. Having some ions in solution is important, because pure water by itself is actually not conductive! Many cells also contain a third electrode, called a reference electrode, that is used to measure the voltage at our anode or cathode electrodes, but it itself doesn't participate in any reactions. All of these electrodes are hooked up to a device called a potentiostat labelled P. The potentiostat can control the current or voltage at our electrodes and measure the response from our electrochemical cell.

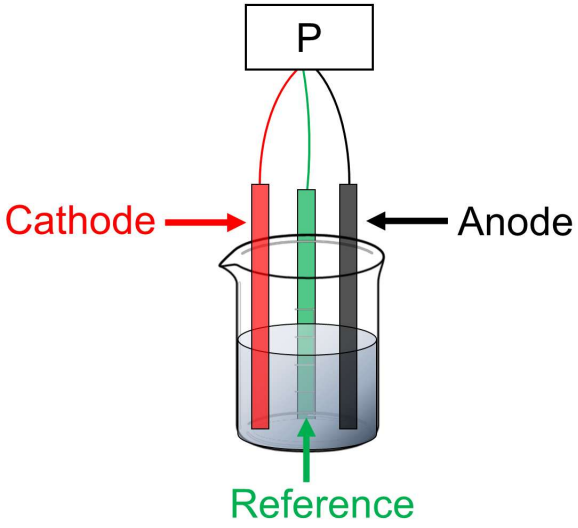

Figure 2. A model electrochemical cell with the three electrodes (cathode, anode, reference) hooked up to a potentiostat (P) while immersed in a water solution containing dissolved ions.

Having the two electrodes (anode and cathode) immersed in a conductive solution is important because electrochemistry is all about moving charges, i.e. electrons, from one place to another, in this case moving electrons from the anode to the cathode. This means that at the anode we are doing oxidation, or the removal of electrons from something in solution (or water itself). Electrons are negatively charged, so by removing them from our target compound (or water) we are making our target compound more positive, i.e. more "oxidized". These electrons then travel to the cathode where they reduce a compound (or water) dissolved in solution. Because we are adding electrons that means this compound is now more negative, i.e. more "reduced." A common mnemonic to remember this is OIL RIG "**O**xidation **I**s **L**oss, **R**eduction **I**s **G**ain," where oxidation is loss of electrons and reduction is gain of electrons.

Thinking back to the example of chrome-plating, the un-plated car rim is used as a cathode in a water solution containing dissolved chromium ions. Using a stainless steel anode, water is oxidized into oxygen gas producing electrons. The electrons are then sent to the un-plated rim cathode to reduce the positively charged chromium ions to neutrally charged chromium metal.

This metal uniformly coats the rim and leaves a nice shiny layer on the surface! While more complicated analysis can be done to understand what might be happening in greater detail at the different electrodes, the simple dual process of oxidation and reduction defines all electrochemical experiments.

Now that a basic understanding of electrochemistry has been developed, we can return to the work I have done with antimony (Sb). There are three primary fields of renewable energy materials that I investigated, which will be overviewed in the following three sections. Each section is a little bit different and will therefore contain introductions to their respective field of study and explanations on the different terminology used within each section. Section 1.2 describes the work I have done on developing Sb-containing oxide materials for water oxidation in acidic solutions. Section 1.3 is about how I developed a method to create quaternary Sb-containing metal oxides to split water using sunlight. Section 1.4 explores the results of using Sb and bismuth (Bi) to produce ammonia from nitrogen gas.

1.2 Antimony oxides for water oxidation in acid

This section contains a brief summary of the work I have done for chapters two and three of my thesis. Specifically, it focuses on developing acid stable electrodes for water oxidation. "Acid stable electrodes" means that the electrodes (cathode or anode) are stable and do not corrode in acid. When you think of corrosion in acid, think about how your stomach acid is full of hydrochloric acid that dissolves your food. The electrodes I made can resist being dissolved in those kinds of harsh conditions. As mentioned in the chrome plating example above, "water oxidation" is performed by oxidizing water at our anode. This final process produces the fully oxidized form of water, oxygen gas (O_2). The air we breathe is already 21% oxygen gas, so what is the point of making more? To answer that concern, think about hydrogen fueled cars, which use

hydrogen gas (H_2) to produce energy to run the car. Well, to make that hydrogen we needed to reduce water (add in electrons) at a cathode. But those electrons had to come from somewhere right? That somewhere is the reaction happening at the anode, the oxidation of something. And when we are reducing water at the cathode, the easiest reaction to perform at the anode is the oxidation of water!

So we are oxidizing water at the anode in acid to make hydrogen gas at the cathode. Making hydrogen gas is relatively easy in acidic solutions as there are a number of stable and active materials that can reduce water in these conditions. However, making a stable anode to use for water oxidation in acid is not easy as many elements, compounds, and materials are not stable under such harsh conditions. The only materials that are stable are rare and expensive noble metals like iridium and ruthenium. This is where Sb comes in. Antimony oxide (Sb_2O_5) is one of the very few compounds that is stable under the oxidizing, acidic conditions used in this type of electrochemical cell. Antimony oxide is so inert that it cannot even oxidize water when used as the anode! It needs some help by combining it with another element that is able to oxidize water but is not stable on its own in acid, such as cobalt (Co) or manganese (Mn). These ternary (containing three elements) compounds, cobalt antimony oxide ($CoSb_2O_6$) and manganese antimony oxide ($MnSb_2O_6$), oxidized water and showed stable performance for 24 hours in a solution more acidic than your stomach acid! Considering most compounds dissolve in a couple of minutes or hours, lasting for 24 hours is an incredible result.

Figure 3 is the keystone figure to show the stability for these two ternary compounds. On the bottom axis (x-axis) is time in hours, on the left axis (y-axis) is the potential in volts we are measuring at our anode. This potential or voltage can be thought of as, but not directly related to, how much energy we need to put into the system to oxidize water at the anode. If the electrodes

were corroding over time and then eventually had completely dissolved, the lines would spike up to a really high value. The system would then shut off because the electrochemical cell wouldn't have an anode to produce electrons for the cathode. The flat lines indicate the electrodes are still there and able to oxidize water.

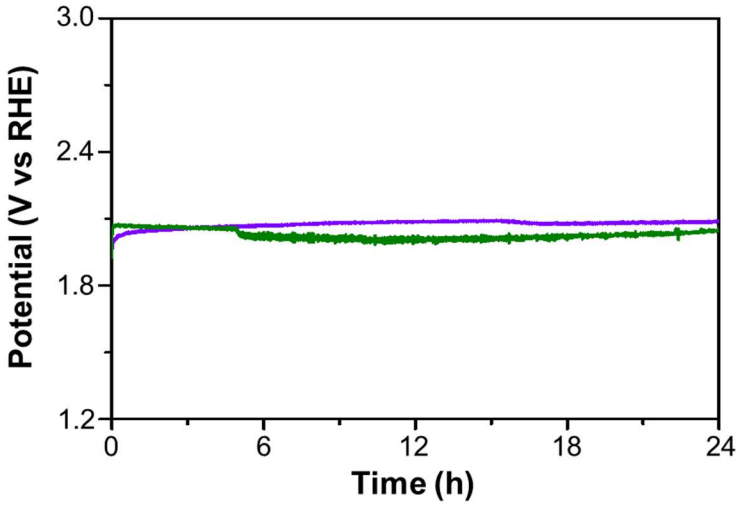

Figure 3. A voltage over time plot of $CoSb_2O_6$ (purple) and $MnSb_2O_6$ (green) performing water oxidation in sulfuric acid.

These two materials are not perfect though. While both $CoSb_2O_6$ and $MnSb_2O_6$ are able to oxidize water for 24 hours, they both have too high of a potential to oxidize water in order to compete with the rare and expensive noble metals. The $MnSb_2O_6$ also slowly dissolves over time and if we ran the experiment in **Figure 3** longer, it would eventually show that big spike in voltage and then shut off. That doesn't mean this discovery isn't important though! The work done on ternary materials containing Sb is an important milestone in developing new and interesting materials to oxidize water in acidic conditions. It can lead to new discoveries that may one day be able to replace the expensive noble metals with abundant, inexpensive catalysts that might contain a little bit of antimony oxide for that extra stability it can provide!

1.3 Antimony oxides and sunlight to split water

This section describes the work I have done in chapter 4 on developing quaternary metal oxides containing antimony (Sb) and bismuth (Bi) to use as photoelectrochemical electrodes. As before, let's break this down into bite sized chunks. "Quaternary metal oxides" means that we are forming metal oxides, which are compounds that contain both oxygen and metal elements, containing four different elements within them. "Containing Sb and Bi" means that two of those elements are antimony (Sb) and bismuth (Bi). These quaternary metal oxides are being used as "photoelectrochemical electrodes." Breaking that into three parts we see photo- meaning "light", electro- meaning "electricity" and chemical meaning "a compound" generally. These quaternary metal oxides are being used to absorb light, to convert that light into electricity (like a solar panel), which is then used to create a chemical compound directly at the surface of the electrode. This chemical compound is usually hydrogen, which is made by reducing water at our cathode, or oxygen, which is made by oxidizing water at our anode. What makes a photoelectrochemical (PEC) electrode different from a regular electrode, such as the $CoSb_2O_6$ described in section 1.2, is that a PEC electrode uses sunlight directly to create hydrogen gas or oxygen gas, instead of relying upon a powerplant to provide electricity.

There are *many* compounds and materials out there being investigated for use as PEC electrodes and they all have varying levels of success. A lot of work is going into trying to optimize known materials to improve their performance and stability, but researchers are also investigating brand new materials to use as PEC electrodes. This is inherently challenging as many of the binary metal oxides, which are composed of one metal and oxygen, have been extensively investigated. A large portion of the possible ternary metal oxides (two metals and oxygen) also have cursory results reported. For this reason, I chose to investigate even more complex compounds containing three metals and oxygen, i.e. quaternary metal oxides.

To help understand the complexity of synthesizing a quaternary material, think about mixing colors while painting a picture. In this analogy, a color is like a metal and the little bit of water you add to help the paint flow is oxygen. If you just add water to one of the colors, you are making a binary oxide, so just one metal and oxygen. Now what if you combined two colors, say red and blue to create purple, in this case you are making a ternary metal oxide. You need the exact same amount of red and blue with some water to create a perfect purple, otherwise you will have some excess blue or excess red which doesn't make that perfect purple. What if you wanted to create the perfect brown (quaternary) by adding in yellow to the purple. Now you need the exact right combination of yellow, red, and blue paints. If you add in a little extra red and blue, it might form some purple (ternary) or maybe the red and blue (binaries) will stay separate. Or if you add in some extra yellow it might form some yellow spots mixed in the brown paint. You can see where this is going. Without very careful care, a material can contain a lot of different impurities and be a big mixture instead of one homogeneous compound. One of the most important parts of doing good science is being able to make observations and draw conclusions using a pure material, because those little impurities could have a big effect!

To make a homogeneous pure quaternary compound I developed a method of first depositing Sb and Bi together using electrochemistry. I applied a negative potential to reduce (adding electrons to) dissolved metal ions at a cathode creating the perfect one to one mixture of Sb and Bi on top of an inert glass slide as a thin film. Think of it like mixing blue and red first in a perfect manner to create flawless purple. To add in the third metal (the yellow paint), I placed a solution that contains the dissolved metal ions of our third metal on top of the Sb and Bi and then heated it up really hot (over 600 °C). The solvent evaporated leaving behind the third metal which then mixed with the Bi and Sb while it was really hot. Oxygen was also able to join the party from

the surrounding air. Once the film cooled down, I washed away any remaining residue from the solution on top using a soaking solution that depended on which of the quaternary materials I was making. After this washing step, the desired quaternary metal oxide phase was successfully synthesized!

Figure 4. The quaternary phase $Cu_2Bi_3Sb_3O_{14}$ on a glass slide after removal of excess residue from the heating process.

Figure 4 shows an example of one of the synthesized quaternary compounds on a glass slide. This particular compound is copper bismuth antimony oxide ($Cu_2Bi_3Sb_3O_{14}$) and was the material I investigated the most as a PEC electrode. Its performance was not close to that of state of the art PEC electrodes unfortunately, but being able to make such a complex material in a relatively easy manner is still an important development towards finding the perfect brown color, or no wait, finding the perfect PEC electrode to split water!

1.4 Antimony and bismuth for ammonia synthesis

Here we are going to deviate slightly from the work I have described thus far. The two sections above have dealt with Sb combined with oxygen to form a metal oxide with some other elements thrown in. For this section, which describes chapter five of my thesis, the work has been done using Sb as an element and not as an oxide. This is different in that we are going to be really

looking at what Sb is like by itself, or combined with another metal, instead of being combined with oxygen. But before we dive into the results of this work, I would first like to describe why ammonia (NH_3) is important.

Ammonia is made up of one nitrogen (N) atom and three hydrogen (H) atoms, so it is a relatively simple molecule. However, the only reliable source of naturally occurring NH_3 is from specialized bacteria that live in soil and on plant roots. These bacteria use powerful (but relatively slow) enzymes that can break the strong triple bond between the two nitrogen atoms in nitrogen gas (N_2) from Earth's atmosphere. This process is relatively efficient and is how a vast majority of life on earth obtains the critical nitrogen needed to make proteins and membranes. However, it was too slow for the growing number of humans on the planet one hundred years ago. Therefore, in the early 1900's, two chemists developed a process to artificially synthesize NH_3 using very high temperatures and very high pressures. This artificial synthesis method is called the Haber-Bosch process after the two scientists that developed it. The NH_3 produced via this process is used to make fertilizers for our food, plastics for our foam mattresses and clothing, cleaners for our houses, etc.

While this has been great for humanity, it has been quite taxing on the environment. The hydrogen we need to combine with nitrogen to make NH_3 comes from natural gas, a limited fossil fuel. This process releases almost two tons of CO_2 for every ton of NH_3 made, contributing a significant portion of the CO_2 emissions humans produce every year. The Haber-Bosch process also requires really high temperatures and pressures which can be quite dangerous and necessitates complex systems to produce this simple molecule safely. However, electrochemistry provides us with a safer and more sustainable solution! By applying a reducing potential at a cathode (remember this is where we add in electrons), we can break apart the strong triple bond in N_2 gas

and then use hydrogen from water to create NH_3. This can all be done at room temperature, atmospheric pressure, and doesn't need large complex machinery to make it all work.

So why isn't it already all over the place? The difficulty with electrochemically producing NH_3 lies in an issue with selectivity. When we apply a reducing potential to our cathode in water with N_2 gas dissolved inside, NH_3 is produced but we also produce hydrogen gas (H_2)! NH_3 is the target molecule for our electrochemical cell but it has to compete with the production of H_2 at the cathode in water. This is difficult because H_2 is easier to make than NH_3 as it is a simpler molecule. Expensive noble metals like gold and palladium have shown interesting properties to improve the selectivity towards NH_3. However, they are expensive for a reason, they are very scarce and not a suitable electrode material for a future sustainable process. This requires investigating other elements to use as our cathode for NH_3 production.

Looking at the periodic table (**Figure 1**), there are a lot of elements and relatively limited work done on a vast majority of them for making NH_3 electrochemically. One that has been investigated semi-recently is bismuth (Bi), another semi-metal right below Sb on the periodic table. This had me thinking, what about Sb? It is right above Bi, it is also a semi-metal and has similar properties to Bi. This curiosity prompted a collaboration with Dr. Youn Jeong Jang, a postdoctoral scholar in our research group who has extensive knowledge in the field of NH_3 synthesis. We therefore worked together to develop and investigate Bi and Sb containing materials to use as cathodes for electrochemically making NH_3.

Figure 5 highlights the results we obtained for Sb alone, Bi alone, and then Sb and Bi combined. The bottom axis is looking at potential, or volts, so like in section 1.2 it is related to the energy we put into the system. The more negative the number, the more reducing potential we are applying to our cathode to reduce nitrogen to NH_3. The left axis is the efficiency of the reaction,

which is telling of how selective our electrodes are for producing NH_3. The higher the number, the more selective the electrode is. Now, the results for Bi and Sb alone are not very interesting, both show relatively low efficiency and thus low selectivity. This is not too surprising as again, H_2 production is just so much easier than NH_3 production. However, by combining the two, we see a significant enhancement in the efficiency that is greater than either Bi or Sb alone.

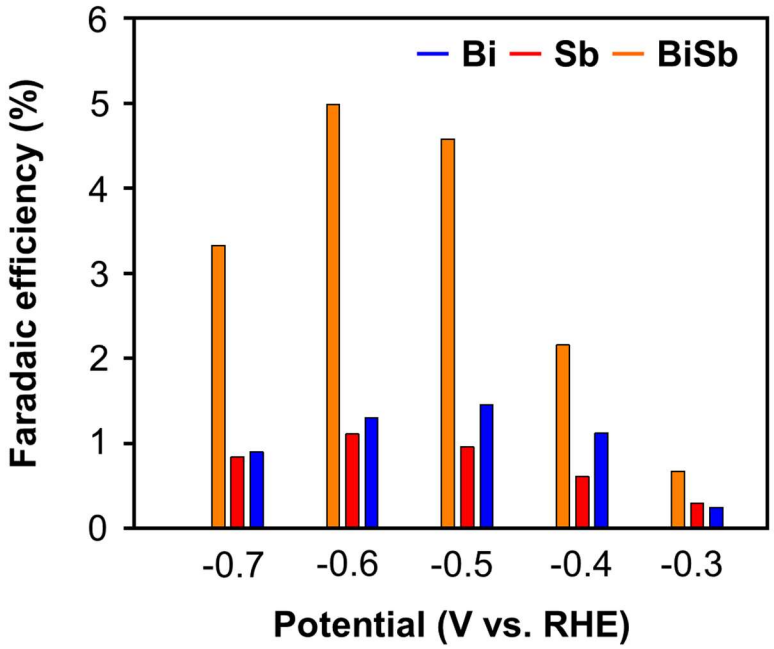

Figure 5. The efficiency (related to selectivity) of ammonia production at different potentials for Bi (blue), Sb (red), and BiSb (orange).

While the overall efficiency is still low for the BiSb combination, it still provides us with new knowledge about making NH_3. Something unique is happening by putting the two elements together that wasn't happening when they were separate. What is happening at the atomic level here? What interesting new information could we learn by exploring this further? Could we use this to make a better material? That is my favorite part about science; finding one new discovery opens the door to a number of new questions that lead to new discoveries and new questions. It is a chain reaction of learning and knowledge. While we have not yet fully elucidated the mechanism

behind this fascinating discovery, we will be continuing to search for answers, because that is what scientists do!

Chapter Two: Electrochemical Synthesis and Investigation of Stochiometric, Phase-Pure $MnSb_2O_6$ Electrodes for the Oxygen Evolution Reaction in Acidic Media

2.1 Introduction

Electrochemical water splitting using electricity generated by renewable sources offers an environmentally benign and sustainable route for H_2 production.[1-3] The electrical energy required for water splitting is determined not only by the thermodynamic potential requirement for water splitting but also by the kinetic overpotential requirements for the hydrogen evolution reaction (HER) and oxygen evolution reaction (OER). Thus, a significant effort has been made for the development of efficient, stable, and inexpensive catalysts for the HER and OER. Oxygen evolution catalysts (OECs), in particular, have been intensively investigated as the OER typically requires more overpotential due to its kinetically more complex four-electron process.[4,5]

While metal-oxide OECs for use in alkaline media have been well established with regards to high performance, long lasting stability, and low cost,[6,7] the progress in the development of practical OECs that work in acidic media has been slow. This is because not many elements or compounds are stable in acidic media (pH < 1) and under the strongly anodic conditions (> 1.2 V vs. RHE) required for the OER. As a result, the only well-established materials that are able to perform the OER in acidic media are expensive noble metal oxides, namely IrO_x and RuO_x.[8-10] However, even these materials are not stable over extended periods of time.[11-13] Considering that proton exchange membrane (PEM) electrolyzers that operate in acidic media have distinctive advantages over alkaline electrolyzers, which include higher current densities and low gas crossover,[14] the development of inexpensive and stable OECs for use in acidic media is of great interest.

In order to develop OECs for acidic media, phases that can be stable in acidic media and under anodic biases need to be identified first. According to Pourbaix diagrams, Sb_2O_5 is one of the few oxides that are thermodynamically stable in acidic media and under anodic biases.[15]

However, Sb_2O_5 is a wide bandgap insulator with overall poor conductivity.[16-18] Furthermore, Sb_2O_5 itself has never been shown to have catalytic activity for any electrochemical oxidation reactions. Thus, I turned to Sb^{5+}-based ternary oxides, whereby the stability of an antimony(V) oxide matrix in acid may be combined with first-row transition metals that are well known for their catalytic activity for the OER to form acid-stable OECs.

Recent work has reported that Sb-containing oxides with a formula of MSb_2O_6 (M = Mn, Ni, and Co) that have a rutile structure can perform the OER in acidic media.[19-21] For example, Moreno-Hernandez *et al.* reported that $Ni_{2-x}Mn_xSb_{1.6-1.8}O_y$ prepared by sputter coating can perform the OER in 1 M H_2SO_4.[19] However, the authors reported severe losses of the constituent metal ions by dissolution after a prolonged stability test. For example, $Ni_{0.5}Mn_{0.5}Sb_{1.7}O_y$ lost more than 50% of Mn by dissolution during a stability test performed at 10 mA/cm^2 for 150 h.

It is important to note that the compounds used in this study did not have the stoichiometric M:Sb ratio (1:2). Instead, they are M-rich or Sb-poor compounds (i.e. $MnSb_{1.6}O_x$ and $Ni_{0.5}Mn_{0.5}Sb_{1.6}O_x$). In this case, it is not clear whether the observed OER performance and the dissolution loss of the compounds during the OER are the intrinsic properties of pure MSb_2O_6 phases or whether they are due to the presence of a defective Mn-rich phase formed on the surface of MSb_2O_6. In fact, a study by Zhou *et al.,* which prepared a library of a Mn-Sb-O system with varying Mn:Sb ratios using physical vapor deposition reported that phases with higher Mn content (i.e. Mn/Sb = 1) showed higher current densities for the OER but they lost more Mn by dissolution during the OER.[20] Zhou *et al.* also reported that enhanced OER activity of the Mn-rich phase is due to the increased presence of Mn^{3+} centers. Considering that Mn^{3+}-containing amorphous binary oxides or hydroxides are known to be catalytic for the OER,[22,23] but not stable in strongly acidic media (pH < 2), it is possible that the OER performance and stability of Mn-rich $MnSb_2O_6$ reported

in the previous studies may not be mainly governed by $MnSb_2O_6$ but by Mn^{3+}-rich defected phases or Mn^{3+}-containing amorphous binary phases at the surface.

The results above demonstrate that MSb_2O_6-based oxide systems may hold promise for the OER in acidic media. However, understanding how the pristine material behaves for the OER is critical in guiding decisions about developing future materials as minor impurities induced by the non-stoichiometry of the electrodes in the above studies may be influencing the overall observed results. Therefore, the purpose of this chapter is to prepare stoichiometric, phase-pure $MnSb_2O_6$ to examine its activity and stability for the OER in a strongly acidic medium. This will greatly complement the results obtained from previous investigations and increase our general understanding of the properties of MSb_2O_6 compounds. To achieve this goal, I prepared a new electrodeposition method to synthesize highly uniform, nanocrystalline $MnSb_2O_6$ electrodes and investigated their OER properties in 0.5 M H_2SO_4.

2.2 Experimental

2.2.1 Materials.

Manganese chloride ($MnCl_2 \cdot 4H_2O$, >99%), potassium antimony tartrate ($K_2Sb_2(C_4H_2O_6)_2 \cdot H_2O$, 99%), TraceCERT antimony ICP standard, TraceCERT manganese ICP standard, and sulfuric acid (H_2SO_4, 95-98%) were purchased from Sigma-Aldrich, and potassium nitrate (KNO_3, 99%) was purchased from Alfa Aesar. All chemicals were used without further purification after purchase. Fluorine doped tin oxide (FTO) on borosilicate glass (Solaronix) was used as the working electrode for electrodeposition. The platinum counter electrode was prepared by depositing 20 nm of titanium as an adhesion layer, followed by 100 nm of platinum on clean glass slides via e-beam evaporation. All solutions were prepared using deionized (DI) water with a resistivity of 18.2 MΩ·cm. FTO substrates were cleaned before deposition by gently rubbing the

surface with soap and water followed by sonication in isopropyl alcohol, acetone, and then twice in water, with each solvent step taking 15 minutes, then being dried under a stream of air.

2.2.2 Synthesis of $MnSb_2O_6$.

In order to prepare $MnSb_2O_6$, a film composed of $Mn(OH)_2$ and Sb was first electrodeposited as the precursor film. Electrodeposition was carried out using a VMP2 multichannel potentiostat (Princeton Applied Research) in an undivided 3 electrode cell composed of a FTO working electrode, a Ag/AgCl (4 M KCl) reference electrode and a Pt counter electrode. The FTO electrode was masked off to a geometric surface area of 0.5 cm^2 with insulating tape (3M, electroplating tape 470).[24] This had the outcome of removing edge effects and improving the uniformity of the film. The aqueous plating solution contained 26 mM $MnCl_2 \cdot 4H_2O$, 11 mM $K_2Sb_2(C_4H_2O_6)_2 \cdot H_2O$, and 800 mM KNO_3. The precursor film was deposited at -1.35 V vs Ag/AgCl by passing 0.04 C/cm^2. The as-deposited amorphous precursor films were converted to crystalline $MnSb_2O_6$ by annealing at 700 °C for 3 hours in air (ramping rate = 2.3 °C/min). After the three hours of anneal time, the films were left to cool down to room temperature for approximately three hours within the furnace.

2.2.3 Characterization.

The sole presence of the AB_2O_6 crystalline phase was confirmed via powder X-ray diffraction (PXRD, D8 Discover, Bruker, Ni-filtered Cu Kα radiation, λ = 1.5418 Å). The surface morphology and elemental composition of the electrodes was characterized with scanning electron microscopy (SEM; LEO Supra55 VP) and energy dispersive spectroscopy (EDS; Noran System Seven, Thermo-Fisher, ultra-dry silicon drift detector) using an accelerating voltage of 2 keV for SEM and 20 keV for EDS. The elemental ratios were calculated using the Thermo Scientific NSS software package (Filter without Standards Quant Fit method and the Proza correction method).

Since the Lα signal of Sn (3.443 keV) from the FTO substrate partially overlaps with the Lα signal of Sb (3.604 keV) from the samples preventing accurate quantification of the sample compositions, powder samples obtained by scrapping the as-deposited films off the FTO substrate were attached to carbon tape and used for EDS analysis. The elemental analyses of the samples were also performed using inductively coupled plasma mass spectrometry (ICP-MS) (Shimadzu ICP Mass Spectrometer-2030) using the solutions obtained by dissolving the as-deposited films in 0.5 M H_2SO_4. Calibration curves were created using the manganese and antimony ICP standards diluted with 0.5 M H_2SO_4. ICP-MS was also used to quantify metal ions dissolved in the electrolyte during a 24 V-t measurement to evaluate the electrochemical stability of the samples. Surface elemental compositions were determined with X-ray photoelectron spectroscopy (XPS) using a Thermo Scientific Kα X-ray photoelectron spectrometer equipped with an Al Kα excitation source. The peak binding energies were calibrated to the adventitious C_{1s} peak at 284.8 eV. The surface elemental ratios were calculated using the Thermo Avantage Software package (ALThermo1 library for sensitivity factors, TPP-2m IMFF for energy correction, and a modified Shirley background for background correction).

2.2.4 Electrochemical characterization.

Electrochemical measurements were performed using either a VMP2 multichannel potentiostat (Princeton Applied Research) or an SP-200 potentiostat/EIS (Bio-Logic Science Instrument). The working electrode of $MnSb_2O_6$, was masked with epoxy (Devcon) to a working geometric surface area of ~0.15 cm^2. An undivided three-electrode cell containing a working electrode of $MnSb_2O_6$, a Ag/AgCl (4 M KCl) reference electrode, and a Pt counter electrode was used for characterization unless otherwise noted.

Linear sweep voltammetry's (LSVs) were performed at a scan rate of 10 mV/s by sweeping the potential in the positive direction from the open circuit potential. All LSVs shown in this study were corrected for the uncompensated solution resistance (R_u) after each experiment, which ranged from 2 and 5 Ohms. The R_u was determined by electrochemical impedance spectroscopy (EIS) where impedance was measured at 1.85 V vs RHE with a frequency range of 100 kHz to 1 Hz and a sinusoidal amplitude of 10 mV with a planar Pt electrode.[19,25,26] Galvanostatic water oxidation was performed at 10 mA/cm^2. All electrochemical experiments were performed in 0.5 M H_2SO_4 (pH 0.3) unless otherwise noted and without agitation (except for the galvanostatic water oxidation experiments where stirring was used to assist in removal of bubbles forming on the electrode surface).

The Faradaic efficiency (FE) for O_2 evolution was determined using a custom designed, air tight, two compartment, glass cell with a smaller Ag/AgCl (3 M NaCl) reference electrode. O_2 gas generated was detected using an Ocean Optics fluorescence-based oxygen sensor (Neofox FOSPOR-R). The oxygen sensor measured the O_2 content in the headspace as mole %. This was converted to μmol after first adjusting for the O_2 dissolved in solution using Henry's Law. The overall FE for O_2 evolution was calculated by the following equation:

$$\text{FE } (\%) = \frac{4 \text{ x } n_{O_2}(\text{mol}) \text{ x } F \text{ (C mol}^{-1})}{\text{Total charged passed (C)}} \text{ x } 100$$

While a Ag/AgCl reference was used in each experiment performed, all results within this report are presented against the reversible hydrogen electrode (RHE) for direct comparison to other reports in aqueous solution but that contain different pH values. The conversion between Ag/AgCl and RHE reference electrode values can be done via the following equation:

$$E_{(vs\ RHE)} = E_{(vs\ Ag/AgCl)} + E_{(Ag/AgCl)}(reference) + 0.0591\ V \times pH(at\ 25\ °C)$$

$$E_{Ag/AgCl}(reference, 4\ M\ KCl) = 0.1976\ V\ vs\ NHE\ at\ 25\ °C$$

$$E_{Ag/AgCl}(reference, 3\ M\ NaCl) = 0.209\ V\ vs\ NHE\ at\ 25\ °C$$

2.3 Results and Discussion

2.3.1 Synthesis, Characterization, and OER performance of $MnSb_2O_6$.

The $MnSb_2O_6$ electrodes used for this study were synthesized via an electrochemical co-deposition of manganese hydroxide and antimony metal using a plating solution composed of potassium antimony tartrate, manganese chloride, and potassium nitrate. The Mn was co-deposited not as Mn metal but as $Mn(OH)_2$ because the reduction potential of Mn^{2+} to Mn^0 is more negative than that of Sb^{3+} to Sb^0.[15] Under the potential used to deposit Sb, nitrate is reduced to nitrite as shown by the equation below:[27]

$$NO_3^- + H_2O + 2e^- \rightleftharpoons NO_2^- + 2OH^-$$

The OH^- produced by this reaction increases the local pH at the WE surface, decreasing the solubility of Mn^{2+}, and results in the precipitation of Mn^{2+} as $Mn(OH)_2$. The deposition potential and the Mn:Sb ratio in the plating solution were adjusted such that the Mn:Sb ratio in the as-deposited film is exactly and uniformly 1:2 throughout the films, which was confirmed by energy dispersive X-ray spectroscopy (EDS). The bulk Mn:Sb ratio of the as-deposited film was additionally confirmed to be 1:2 using inductively coupled plasma mass spectrometry (ICP-MS) of the solution obtained by the dissolution of the entire as-deposited film in 0.5 M H_2SO_4.

The as-deposited amorphous films were converted to crystalline $MnSb_2O_6$ by annealing in air for three hours at 700 °C (**Figure 1**). Using EDS, the Mn:Sb ratios were confirmed to remain

as 1:2 after annealing. The X-ray diffraction (XRD) pattern of the resulting $MnSb_2O_6$ films are shown in **Figure 1**.

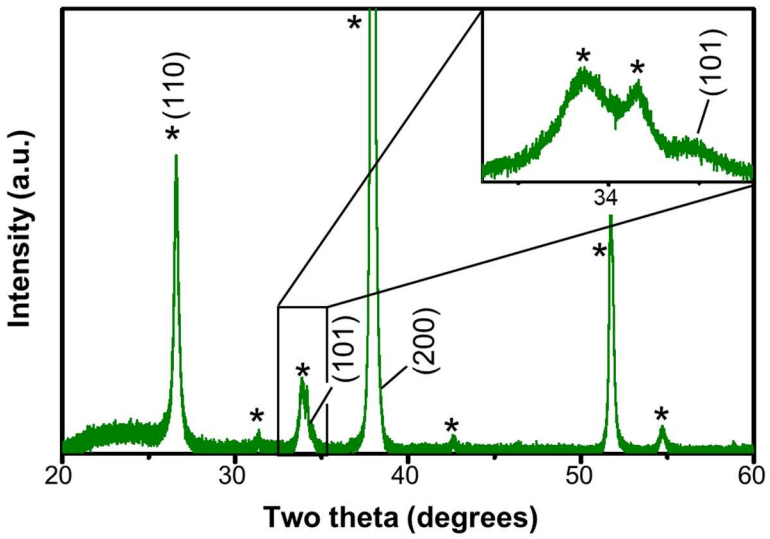

Figure 1. XRD pattern of the post annealed $MnSb_2O_6$. The (hkl) indices are assigned from the PDF card for $MnSb_2O_6$ (04-011-4962). The peaks corresponding to the FTO substrate are denoted by an asterisk.

Since these films are very thin (~200 nm for $MoSb_2O_6$) and are composed of nanocrystals (**Figure 2**), the intensities of the peaks generated by these films were very low compared with those from the FTO substrate. I would like to note that any attempt to grow a thicker film resulted in the formation of films with less uniform Mn:Sb ratios throughout the films. The crystalline phase of $MnSb_2O_6$ could not reliably be confirmed by XRD due to two reasons. First, since the $MnSb_2O_6$ film is extremely thin and nanocrystalline, the peak intensities were very low compared with those from the FTO substrate. Second, since both the FTO and $MnSb_2O_6$ have the same rutile structure with similar cell parameters, the peaks from $MnSb_2O_6$ overlap closely with those from the FTO substrate. Thus, in order to confirm the structure type of $MnSb_2O_6$, I grew a thicker $MnSb_2O_6$ film on a non-rutile phase substrate (i.e. indium tin oxide (ITO)). Compared with the

~200 nm thin film, the stoichiometry of this thicker $MnSb_2O_6$ film was not as uniform throughout the film. However, its XRD pattern shows peaks only from $MnSb_2O_6$ and confirmed that $MnSb_2O_6$ produced using my new method has a rutile structure (**Figure 3**).

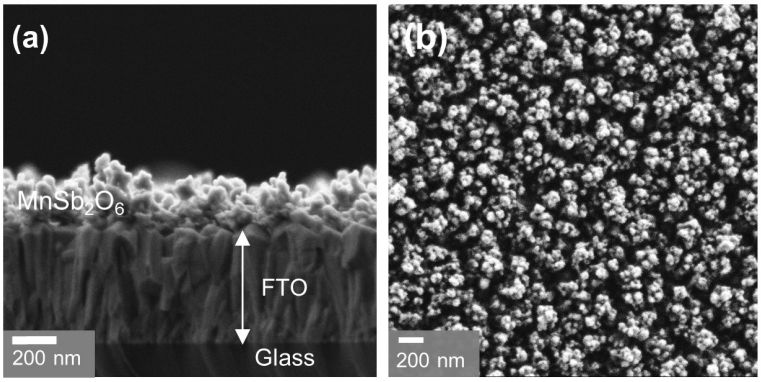

Figure 2. (a) Side view and (b) top down SEM images of $MnSb_2O_6$ after annealing.

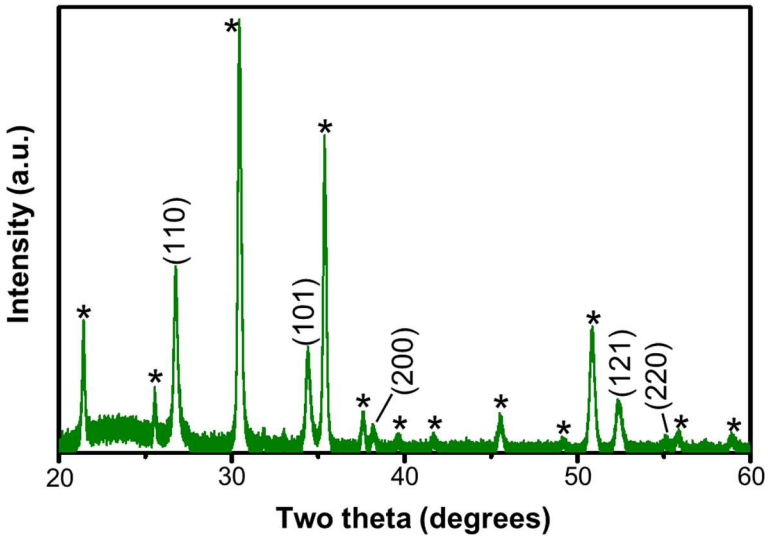

Figure 3: The XRD pattern of thicker $MnSb_2O_6$ deposited onto an ITO substrate in order to observe more of the peaks associated with the rutile-type phase of $MnSb_2O_6$. The peaks corresponding to the ITO substrate are denoted by an asterisk.

The water oxidation performance of $MnSb_2O_6$ electrodes was investigated using linear sweep voltammetry (LSV) in 0.5 M H_2SO_4 (pH 0.3). In order to show the unambiguous effect of incorporating Mn^{2+} into the Sb oxide matrix on the OER performance, the LSV of Sb_2O_4

($Sb^{3+}Sb^{5+}O_4$) is also shown for comparison (**Figure 4**). Sb_2O_4 is the oxide that is obtained when antimony metal electrodeposited on FTO alone is annealed in the air using the same conditions to obtain crystalline $MnSb_2O_6$ electrodes. The LSV of Sb_2O_4 shows no anodic current when the potential was swept to 2.2 V vs. RHE, suggesting that it is inactive for the OER. On the other hand, $MnSb_2O_6$ generated considerable anodic current due to the OER, suggesting that its OER activity truly originates from the presence of Mn in the compound. The overpotential required to achieve 10 mA/cm^2 was ~0.940 V for $MnSb_2O_6$.

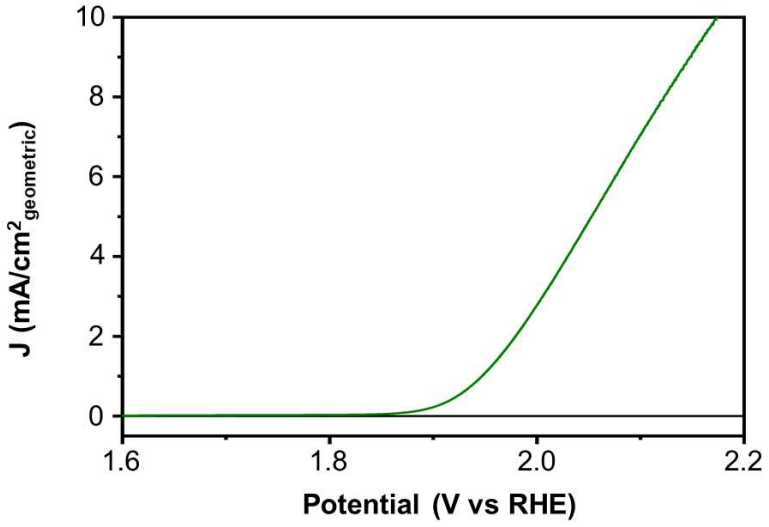

Figure 4. LSVs of $MnSb_2O_6$ (green) and Sb_2O_4 (black) in 0.5 M H_2SO_4 (pH 0.3) with the current density determined using the geometric surface area of the electrode.

The stability of $MnSb_2O_6$ during the OER in acidic media was first examined under galvanostatic water oxidation at 10 mA/cm^2 by recording the change in the potential required to maintain this current density over 24 h (**Figure 5a).** The result shows negligible change in the required potential for $MnSb_2O_6$ to achieve 10 mA/cm^2. I confirmed that the current generated during this experiment was truly associated with O_2 production by calculating the Faradic efficiency (FE) for O_2 production by comparing the amount of O_2 detected and the amount O_2

theoretically calculated assuming 100 % FE (**Figure 5b**). The FE for O_2 production of $MnSb_2O_6$ was 95% at 300 min. I note that the overpotentials required to achieve 10 mA/cm^2 by $MnSb_2O_6$ is significantly higher than that of state-of-the-art catalysts in acidic or basic conditions.[25,28] For example, iridium oxide-based OER catalysts can achieve 10 mA/cm^2 with an overpotential of 0.20V - 0.35 V.[25,29-31]

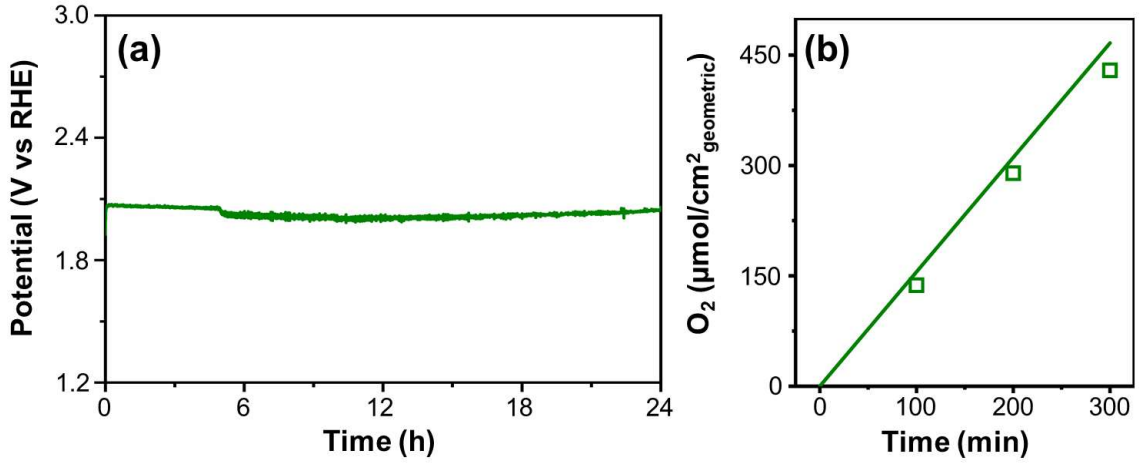

Figure 5. (a) The V-t plot of $MnSb_2O_6$ obtained for galvanostatic water oxidation at 10 mA/cm^2 in 0.5 M H_2SO_4 (pH 0.3). (b) Oxygen produced by $MnSb_2O_6$ electrodes during galvanostatic water oxidation at 10 mA/cm^2 in 0.5 M H_2SO_4 (pH 0.3) (open squares). The theoretically expected amount of oxygen assuming 100% FE is shown as a solid line.

2.3.2 Post OER Analysis.

Although the V-t plots suggested the stability of $MnSb_2O_6$ during the OER, the work by Moreno-Hernandez *et al.* clearly demonstrated that stable V-t performance does not necessarily mean that the catalyst is stable. Their sample, $Ni_{0.5}Mn_{0.5}Sb_{1.7}O_y$, lost more than 50% of its Mn by dissolution during the V-t measurement but this severe corrosion did not affect the required potential to generate 10 mA/cm^2 over 150 h.[19] Thus, I performed careful post analysis of the $MnSb_2O_6$ films using various techniques after the 24 h V-t measurement at 10 mA/cm^2 to examine for any possible signs of corrosion.

Figure 6 shows the XRD patterns before and after the V-t measurement, with insets showing the intensity change of the most representative and intense peak for $MnSb_2O_6$. The (101) peak of $MnSb_2O_6$ showed an evident decrease in intensity, indicating possible loss of $MnSb_2O_6$ during the V-t measurement. SEM images of these electrodes taken after the V-t measurement (**Figure 7**) agree well with the XRD patterns; the void space between the nanoparticles became larger due to the pitting caused by the loss of $MnSb_2O_6$ by dissolution. The EDS analysis of $MnSb_2O_6$ showed that the Mn:Sb ratio remained 1:2, suggesting that the corrosion involved the dissolution of both Mn and Sb and not the preferential leaching of Mn or Sb.

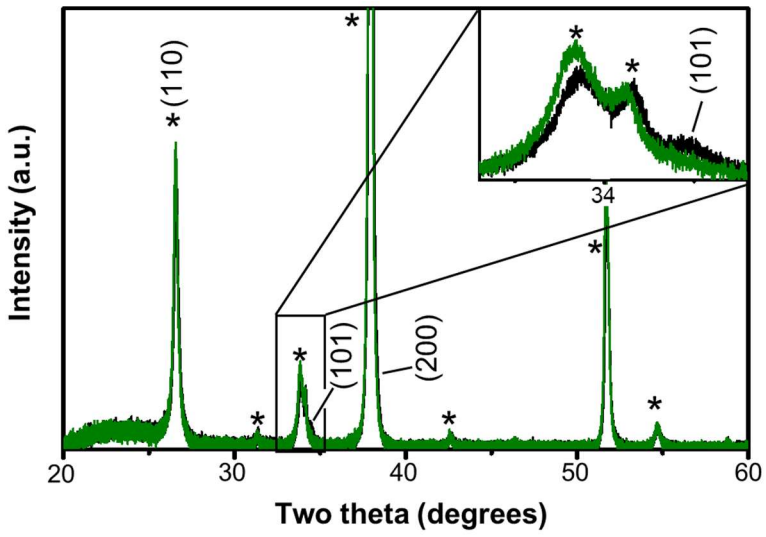

Figure 6. XRD pattern of $MnSb_2O_6$ electrodes after a 24 h V-t measurement at 10 mA/cm^2. The XRD pattern of the corresponding film before the V-t measurement is shown in black for comparison. An inset is provided to show the change in peak intensity after the V-t measurement. The peaks corresponding to the FTO substrate are denoted by an asterisk.

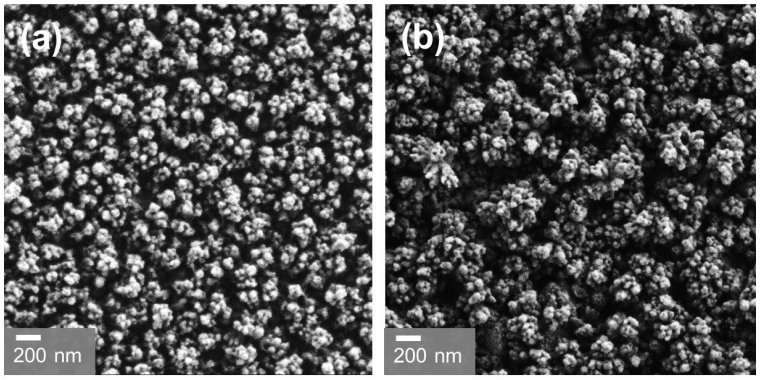

Figure 7. Top-view SEM images of $MnSb_2O_6$ (a) before and (b) after the galvanostatic water oxidation at 10 mA/cm^2 for 24 h.

I also performed X-ray photoelectron spectroscopy (XPS) before and after the V-t measurement to probe for changes in the oxidation states of the constituent elements on the $MnSb_2O_6$ electrode surface.

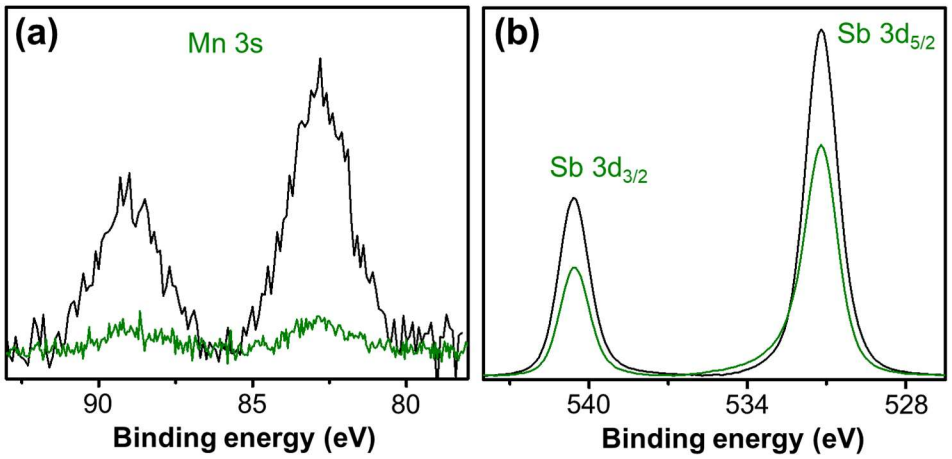

Figure 8. XPS of the (a) Mn 3s and (b) Sb 3d regions of $MnSb_2O_6$ before (black) and after (green) the V-t measurement at 10 mA/cm^2 for 24 h.

Figure 8a shows the Mn 3s region of the $MnSb_2O_6$ electrode containing the doublet associated with the 3s electrons. The splitting of the Mn 3s peak into a doublet arises from the coupling between the non-ionized 3s electrons and the valence electrons in the 3d orbitals.[32] This splitting provides a useful way to examine the Mn oxidation state, as the distance between the two

peaks can provide information on the surface oxidation state, where higher oxidation states show a smaller binding energy difference and lower oxidation states show a larger binding energy difference. The trend of increasing oxidation state leading to a decrease in the distance between the two peaks is agreed upon and a range of values for each oxidation state can be found within the literature. For MnO the distance between the two peaks is reported between 5.7-6.3 eV, for Mn_2O_3 it is 5.2-5.4 eV and for MnO_2 it is 4.5-4.7 eV.[32-35] For the pristine $MnSb_2O_6$, I observed the Mn 3s splitting to be 6.1 eV, which lies firmly within the range of differences in binding energies associated with Mn^{2+}. After the 24-hour V-t measurement, I saw a large decrease in signal intensity for Mn in the Mn 3s region. This was expected because the XRD and SEM results showed the corrosion of $MnSb_2O_6$ during the V-t measurement. The distance of the doublet did not appear to change significantly, suggesting Mn^{2+} remained as the major Mn species at the surface. A significant decrease was also observed in the Mn 2p region (**Figure 9**), further confirming the loss of Mn from the surface.

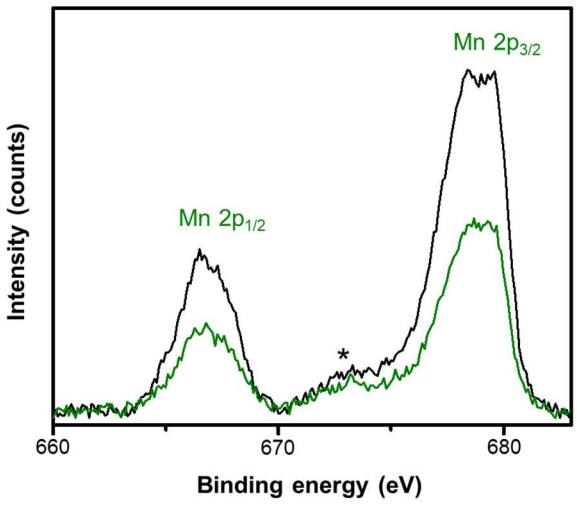

Figure 9. XPS spectra of the Mn 2p region for the $MnSb_2O_6$ electrode before (black) and after (green) the V-t measurement at 10 mA/cm^2 for 24 h. The asterisk denotes a satellite peak for the Mn $2p_{3/2}$ peak.

The Sb 3d region of $MnSb_2O_6$ is shown in **Figure 8b**. The $3d_{5/2}$ peak in this plot overlaps with the O 1s peak.[36,37] Thus, the Sb $3d_{3/2}$ peak was used to examine the oxidation state of Sb on the $MnSb_2O_6$ surface. For the Sb $3d_{3/2}$ peak, Sb^{3+} oxides show a peak at a binding energy of 539.6 eV, Sb^{5+} oxides at 540.6 eV, and an even mixture ($Sb^{3+}Sb^{5+}O_2$) at a binding energy in-between at 540.0 eV. The Sb $3d_{3/2}$ peak for $MnSb_2O_6$ before the V-t measurement shows a maxima at a binding energy of 540.6 eV, which is the binding energy of Sb^{5+} in Sb_2O_5, indicating the surface is Sb^{5+} in character with little to no Sb^{3+} present.[36,37] The Sb $3d_{3/2}$ peak position did not change after the V-t measurement was performed, suggesting that the oxidation state of Sb did not change during the OER. However, the intensity decreased for both the Sb $3d_{3/2}$ peak and the Sb $3d_{5/2}$ peak, due to the loss of $MnSb_2O_6$ by dissolution, decreasing the coverage of the substrate by $MnSb_2O_6$ as shown in **Figure 7**. The surface Mn:Sb ratio before the V-t measurement was 1:2.65, indicating an Sb rich surface. After the V-t measurement, the surface Mn:Sb ratio was 1:2.82. The fact that the surface ratio remained more or less the same, although a considerable loss of $MnSb_2O_6$ by dissolution during the V-t measurement was revealed by XRD and SEM, suggests that comparable amounts of Mn and Sb were dissolved during the V-t measurement. This could also be confirmed by the ICP-MS analysis of the electrolyte used for the V-t measurement. I observed 61.4% of the Mn and 63.9% of the Sb in the $MnSb_2O_6$ electrode were dissolved into the solution during the V-t measurement.

The post OER analysis shows $MnSb_2O_6$ is not stable in the long term under OER conditions in a strongly acidic medium even when it is prepared as a stoichiometric, phase-pure compound. As I mentioned previously, the performance of $MnSb_2O_6$ is also not good enough to replace state-of-the-art OER catalysts in acidic media, as to achieve realistic OER current densities that are used in state-of-the-art electrolyzers (>100 mA/cm^2) even higher voltages are required (**Figure 10**).

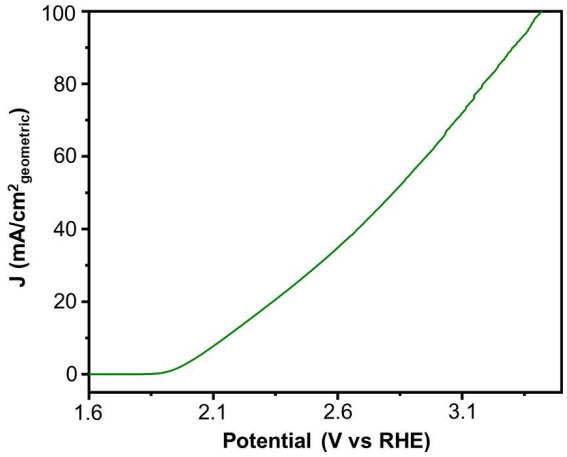

Figure 10. LSV of $MnSb_2O_6$ in 0.5 M H_2SO_4 (pH 0.3) demonstrating the required potential to reach 100 mA/cm^2 for the electrode, with the current density determined using the geometric surface area of the electrode.

2.4 Conclusion

I have developed a new electrochemical method to synthesize stoichiometric, phase-pure $MnSb_2O_6$ electrodes for investigation of their ability to oxidize water in acidic media. $MnSb_2O_6$ showed stable V-t performance during the OER at 10 mA/cm^2 over the course of a 24-hour V-t measurement. However, careful post OER analysis that examined changes in morphology, crystallinity, and surface composition revealed that $MnSb_2O_6$ is not stable and gradually dissolves over time, indicating it is not, even when used as a stoichiometric pure phase compound, a good candidate to replace current state-of-the-art IrO_x and RuO_x catalysts in acidic media. However, considering the scarcity of inexpensive oxide matrices that are stable while active for the OER, Sb^{5+} containing metal oxides may offer a promising matrix for further composition tuning to develop OECs for use in acidic media.

2.5 References

1. Crabtree, G. W.; Dresselhaus, M. S., The Hydrogen Fuel Alternative. *MRS Bull.* **2011**, *33*, 421-428.

2. Formal, F. L.; Bourée, W. S.; Prévot, M. S.; Sivula, K., Challenges towards Economic Fuel Generation from Renewable Electricity: The Need for Efficient Electro-Catalysis. *Chimia* **2015**, *69*, 789-798.

3. Levene, J. I.; Mann, M. K.; Margolis, R. M.; Milbrandt, A., An analysis of hydrogen production from renewable electricity sources. *Sol. Energy* **2007**, *81*, 773-780.

4. Dau, H.; Limberg, C.; Reier, T.; Risch, M.; Roggan, S.; Strasser, P., The Mechanism of Water Oxidation: From Electrolysis via Homogeneous to Biological Catalysis. *ChemCatChem* **2010**, *2*, 724-761.

5. Man, I. C.; Su, H.-Y.; Calle-Vallejo, F.; Hansen, H. A.; Martínez, J. I.; Inoglu, N. G.; Kitchin, J.; Jaramillo, T. F.; Nørskov, J. K.; Rossmeisl, J., Universality in Oxygen Evolution Electrocatalysis on Oxide Surfaces. *ChemCatChem* **2011**, *3*, 1159-1165.

6. Jamesh, M.-I.; Sun, X., Recent progress on earth abundant electrocatalysts for oxygen evolution reaction (OER) in alkaline medium to achieve efficient water splitting – A review. *J. Power Sources* **2018**, *400*, 31-68.

7. Jung, S.; McCrory, C. C. L.; Ferrer, I. M.; Peters, J. C.; Jaramillo, T. F., Benchmarking nanoparticulate metal oxide electrocatalysts for the alkaline water oxidation reaction. *J. Mater. Chem. A* **2016**, *4*, 3068-3076.

8. Lee, Y.; Suntivich, J.; May, K. J.; Perry, E. E.; Shao-Horn, Y., Synthesis and Activities of Rutile IrO2 and RuO2 Nanoparticles for Oxygen Evolution in Acid and Alkaline Solutions. *J. Phys. Chem. Lett.* **2012**, *3*, 399-404.

9. Abbott, D. F.; Lebedev, D.; Waltar, K.; Povia, M.; Nachtegaal, M.; Fabbri, E.; Coperet, C.; Schmidt, T. J., Iridium Oxide for the Oxygen Evolution Reaction: Correlation between Particle Size, Morphology, and the Surface Hydroxo Layer from Operando XAS. *Chem. Mater.* **2016**, *28*, 6591-6604.

10. Reier, T.; Oezaslan, M.; Strasser, P., Electrocatalytic Oxygen Evolution Reaction (OER) on Ru, Ir, and Pt Catalysts: A Comparative Study of Nanoparticles and Bulk Materials. *ACS Catal.* **2012**, *2*, 1765-1772.

11. Cherevko, S.; Zeradjanin, A. R.; Topalov, A. A.; Kulyk, N.; Katsounaros, I.; Mayrhofer, K. J. J., Dissolution of Noble Metals during Oxygen Evolution in Acidic Media. *Chemcatchem* **2014**, *6*, 2219-2223.

12. Jovanovič, P.; Hodnik, N.; Ruiz-Zepeda, F.; Arčon, I.; Jozinović, B.; Zorko, M.; Bele, M.; Šala, M.; Šelih, V. S.; Hočevar, S.; Gaberšček, M., Electrochemical Dissolution of Iridium and Iridium Oxide Particles in Acidic Media: Transmission Electron Microscopy,

Electrochemical Flow Cell Coupled to Inductively Coupled Plasma Mass Spectrometry, and X-ray Absorption Spectroscopy Study. *J. Am. Chem. Soc.* **2017**, *139*, 12837-12846.

13. Hodnik, N.; Jovanovič, P.; Pavlišič, A.; Jozinović, B.; Zorko, M.; Bele, M.; Šelih, V. S.; Šala, M.; Hočevar, S.; Gaberšček, M., New Insights into Corrosion of Ruthenium and Ruthenium Oxide Nanoparticles in Acidic Media. *J. Phys. Chem. C* **2015**, *119*, 10140-10147.

14. Carmo, M.; Fritz, D. L.; Mergel, J.; Stolten, D., A comprehensive review on PEM water electrolysis. *Int. J. Hydrog. Energy* **2013**, *38*, 4901-4934.

15. Pourbaix, M., *Atlas of Electrochemical Equilibria in Aqueous Solutions.* 2 ed.; National Association of Corrosion Engineers: Houston, Texas, **1974**; p 524-532.

16. Tigau, N.; Ciupina, V.; Prodan, G., Structural, optical and electrical properties of Sb_2O_3 thin films with different thickness. *J. Optoelectron. Adv. Mater.* **2006**, *8*, 37-42.

17. Ozawa, K.; Sakka, Y.; Amano, M., Preparation and electrical conductivity of three types of antimonic acid films. *J. Mater. Res.* **1998**, *13*, 830-833.

18. Herrmann, J. M. J.; Portefaix, J. L.; Forissier, M.; Figueras, F.; Pichat, P., Electrical Behavior of Powdered Tin-Antimony Mixed-Oxide Catalysts. *J. Chem. Soc. Faraday T. 1* **1979**, *75*, 1346-1355.

19. Moreno-Hernandez, I. A.; MacFarland, C. A.; Read, C. G.; Papadantonakis, K. M.; Brunschwig, B. S.; Lewis, N. S., Crystalline nickel manganese antimonate as a stable water-oxidation catalyst in aqueous 1.0 M H_2SO_4. *Energ. Environ. Sci.* **2017**, *10*, 2103-2108.

20. Zhou, L.; Shinde, A.; Montoya, J. H.; Singh, A.; Gul, S.; Yano, J.; Ye, Y.; Crumlin, E. J.; Richter, M. H.; Cooper, J. K.; Stein, H. S.; Haber, J. A.; Persson, K. A.; Gregoire, J. M., Rutile Alloys in the Mn–Sb–O System Stabilize Mn3+ To Enable Oxygen Evolution in Strong Acid. *ACS Catal.* **2018**, *8*, 10938-10948.

21. Moreno-Hernandez, I. A.; Brunschwig, B. S.; Lewis, N. S., Crystalline nickel, cobalt, and manganese antimonates as electrocatalysts for the chlorine evolution reaction. *Energ. Environ. Sci.* **2019**, *12*, 1241-1248.

22. Wiechen, M.; Najafpour, M. M.; Allakhverdiev, S. I.; Spiccia, L., Water oxidation catalysis by manganese oxides: learning from evolution. *Energ. Environ. Sci.* **2014**, *7*, 2203-2212.

23. Takashima, T.; Hashimoto, K.; Nakamura, R., Mechanisms of pH-Dependent Activity for Water Oxidation to Molecular Oxygen by MnO_2 Electrocatalyst. *J. Am. Chem. Soc.* **2012**, *134*, 1519-1527.

24. Govindaraju, G. V.; Wheeler, G. P.; Lee, D.; Choi, K.-S., Methods for Electrochemical Synthesis and Photoelectrochemical Characterization for Photoelectrodes. *Chem. Mater.* **2017**, *29*, 355-370.

25. McCrory, C. C. L.; Jung, S.; Peters, J. C.; Jaramillo, T. F., Benchmarking Heterogeneous Electrocatalysts for the Oxygen Evolution Reaction. *J. Am. Chem. Soc.* **2013**, *135*, 16977-16987.

26. Stevens, M. B.; Enman, L. J.; Batchellor, A. S.; Cosby, M. R.; Vise, A. E.; Trang, C. D. M.; Boettcher, S. W., Measurement Techniques for the Study of Thin Film Heterogeneous Water Oxidation Electrocatalysts. *Chem. Mater.* **2017**, *29*, 120-140.

27. Kang, D.; Kim, T. W.; Kubota, S. R.; Cardiel, A. C.; Cha, H. G.; Choi, K.-S., Electrochemical Synthesis of Photoelectrodes and Catalysts for Use in Solar Water Splitting. *Chem. Rev.* **2015**, *115*, 12839-12887.

28. Hunter, B. M.; Gray, H. B.; Müller, A. M., Earth-Abundant Heterogeneous Water Oxidation Catalysts. *Chem*. *Rev*. **2016**, *116*, 14120-14136.

29. Pearce, P. E.; Yang, C.; Iadecola, A.; Rodriguez-Carvajal, J.; Rousse, G.; Dedryvère, R.; Abakumov, A. M.; Giaume, D.; Deschamps, M.; Tarascon, J.-M.; Grimaud. Revealing the Reactivity of the Iridium Trioxide Intermediate for the Oxygen Evolution Reaction in Acidic Media. *Chem. Mater.* **2019**, *31*, 5845-5855.

30. Jiang, H.; Ge, S.; Zhang, Y.; Dong, M.; Wu, S.; Wu, M.; Zhang, J.; Ge, R.; Gua, Z., Self-Supported Iridum Oxide Nanostructures for Electrocatalytic Water Oxidation in Acidic Media. *J. Phys. Chem. C.* **2020**, *124*, 2-8.

31. Seitz, L. C.; Dickens, C. F.; Nishio, K.; Hikita, Y.; Montoya, J.; Doyle, A.; Kirk, C.; Vojvodic, A.; Hwang, H. Y.; Norskov, J. K.; Jaramillo, T. F., A highly active and stable $IrO_x/SrIrO_3$ catalyst for the oxygen evolution reaction. *Science*. 2016, *353*, 1011-1014.

32. Nelson, A. J.; Reynolds, J. G.; Roos, J. W., Core-level satellites and outer core-level multiplet splitting in Mn model compounds. *J. Vac. Sci. Technol. A-Vac. Surf. Films* **2000**, *18*, 1072-1076.

33. Cerrato, J. M.; Hochella, M. F.; Knocke, W. R.; Dietrich, A. M.; Cromer, T. F., Use of XPS to Identify the Oxidation State of Mn in Solid Surfaces of Filtration Media Oxide Samples from Drinking Water Treatment Plants. *Environ. Sci. Technol.* **2010**, *44*, 5881-5886.

34. Galakhov, V. R.; Demeter, M.; Bartkowski, S.; Neumann, M.; Ovechkina, N. A.; Kurmaev, E. Z.; Lobachevskaya, N. I.; Mukovskii, Y. M.; Mitchell, J.; Ederer, D. L., Mn 3s exchange splitting in mixed-valence manganites. *Phys. Rev. B* **2002**, *65*, 113102.

35. Chigane, M.; Ishikawa, M., Manganese Oxide Thin Film Preparation by Potentiostatic Electrolyses and Electrochromism. *J. Electrochem. Soc.* **2000**, *147*, 2246-2251.

36. Garbassi, F., XPS and AES study of antimony oxides. *Surf. Interface Anal.* **1980**, *2*, 165-169.

37. Izquierdo, R.; Sacher, E.; Yelon, A., X-ray photoelectron spectra of antimony oxides. *Appl. Surf. Sci.* **1989**, *40*, 175-177.

Chapter Three: Electrochemical Synthesis and Investigation of Stoichiometric, Phase-Pure $CoSb_2O_6$ Electrodes for the Oxygen Evolution Reaction in Acidic Media

3.1 Introduction

Electrochemical water splitting using electricity generated by renewable sources offers an environmentally benign and sustainable route for H_2 production.[1-3] The electrical energy required for water splitting is determined not only by the thermodynamic potential requirement for water splitting but also by the kinetic overpotential requirements for the hydrogen evolution reaction (HER) and oxygen evolution reaction (OER). Thus, a significant effort has been made for the development of efficient, stable, and inexpensive catalysts for the HER and OER. Oxygen evolution catalysts (OECs), in particular, have been intensively investigated as the OER typically requires more overpotential due to its kinetically more complex four-electron process.[4,5]

While metal-oxide OECs for use in alkaline media have been well established with regards to high performance, long lasting stability, and low cost,[6,7] the progress in the development of practical OECs that work in acidic media has been slow. This is because not many elements or compounds are stable in acidic media (pH < 1) and under the strongly anodic conditions (> 1.2 V vs. RHE) required for the OER. As a result, the only well-established materials that are able to perform the OER in acidic media are expensive noble metal oxides, namely IrO_x and RuO_x.[8-10] However, even these materials are not stable over extended periods of time.[11-13] Considering that proton exchange membrane (PEM) electrolyzers that operate in acidic media have distinctive advantages over alkaline electrolyzers, which include higher current densities and low gas crossover,[14] the development of inexpensive and stable OECs for use in acidic media is of great interest.

In order to develop OECs for acidic media, phases that can be stable in acidic media and under anodic biases need to be identified first. According to Pourbaix diagrams, Sb_2O_5 is one of the few oxides that are thermodynamically stable in acidic media and under anodic biases.[15]

However, Sb_2O_5 is a wide bandgap insulator with overall poor conductivity.[16-18] Furthermore, Sb_2O_5 itself has never been shown to have catalytic activity for any electrochemical oxidation reactions. Thus, I turn to Sb^{5+}-based ternary oxides, whereby the stability of an antimony oxide matrix in acid may be combined with first-row transition metals that are well known for their catalytic activity for the OER to form acid-stable OECs.

In Chapter Two, I investigated the ability of stochiometric, phase-pure $MnSb_2O_6$ to oxidize water in acidic media and found that while it showed stable performance over a 24 hour V-t measurement, further characterization demonstrated the instability of the material. These results match well with those published on non-stochiometric compounds containing Mn and Sb used for the OER in acidic media.[19-21] However, when compared to other materials for the OER in acidic media that degrade in a matter of minutes, $MnSb_2O_6$ still showed comparably good stability, suggesting that a different transition metal stabilized inside an Sb^{5+} oxide matrix may hold promise. This prompted an investigation on another transition metal containing antimony oxide, $CoSb_2O_6$, for the possibility of a more stable and active compound for the OER in acidic media.

Cobalt-containing oxides are well established for their ability to oxidize water with low overpotentials and remain stable during operation in alkaline media.[7,22,23] However, it is known that the same cobalt based oxides exhibit higher overpotentials, lower faradaic efficiency and substantial corrosion in acidic media that can lead to significantly lower activity via homogeneous water oxidation.[24] There have been a few reports demonstrating enhanced stability of heterogenous cobalt oxide-based materials but all still suffer from substantial corrosion into acidic media during operation as an OER catalyst.[25-27] Therefore, to improve the stability of Co-containing catalysts in acidic media I sought to combine the catalytic ability of cobalt oxide with the stability of an antimony oxide matrix to create an active and stable OEC.

Recent work has reported that Sb-containing oxides with a formula of MSb_2O_6 (M = Mn, Ni, and Co) that have a rutile structure can perform the OER in acidic media.[19-21] Moreno-Hernandez et al. compared the activity of $CoSb_2O_6$ and $MnSb_2O_6$ for water oxidation and chloride oxidation in acidic media (4 M NaCl, pH 2) and reported that $CoSb_2O_6$ is more active for chloride oxidation than $MnSb_2O_6$ and showed almost no loss (<1%) of the catalyst over a 50 hour electrolysis at 100 mA/cm^2 for chloride oxidation.[21] I note that the $CoSb_2O_6$ used in this study was slightly Sb-rich ($CoSb_{2.2}O_x$) while the $MnSb_2O_6$ used in this study was Mn-rich ($MnSb_{1.7}O_x$). In this case, I was curious whether the observed performance difference is solely caused by the difference in the type of transition metal (Co vs. Mn) or by the type of non-stoichiometry (i.e. M-rich vs. Sb-rich) present in these compounds. This work was also done in less acidic conditions (pH 2) than traditionally used for examining the OER activity in acidic media (pH < 1), therefore, I wanted to determine if the excellent stability of the Sb rich-$CoSb_2O_6$ electrode observed by the previous authors was also an effect of the less acidic pH used in their study.

The purpose of the current study is to prepare stoichiometric, phase-pure $CoSb_2O_6$ to examine its activity and stability for the OER in a strongly acidic medium, which will greatly complement the results obtained from previous investigations and increase our general understanding of the properties of MSb_2O_6 compounds. To achieve this goal, highly uniform, nanocrystalline $CoSb_2O_6$ electrodes using a modified version of the $MnSb_2O_6$ electrodeposition method were prepared. After examining the OER performance and stability of this compound, the $CoSb_2O_6$ and $MnSb_2O_6$ performance for the chloride oxidation reaction was additionally examined, so that a more comprehensive understanding of this M-Sb_2O_6 system for electrochemical oxidation reactions in acidic media can be obtained.

3.2 Experimental

3.2.1 Materials.

Cobalt chloride ($CoCl_2 \cdot 6H_2O$, 98%), potassium antimony tartrate ($K_2Sb_2(C_4H_2O_6)_2 \cdot H_2O$, 99%), TraceCERT antimony ICP standard, TraceCERT cobalt ICP standard and sulfuric acid (H_2SO_4, 95-98%) were purchased from Sigma-Aldrich, and potassium nitrate (KNO_3, 99%) was purchased from Alfa Aesar. All chemicals were used without further purification after purchase. Fluorine doped tin oxide (FTO) on borosilicate glass (Solaronix) was used as the working electrode for electrodeposition. The platinum counter electrode was prepared by depositing 20 nm of titanium as an adhesion layer, followed by 100 nm of platinum on clean glass slides via e-beam evaporation. All solutions were prepared using deionized (DI) water with a resistivity of 18.2 MΩ·cm. FTO substrates were cleaned before deposition by gently rubbing the surface with soap and water followed by sonication in isopropyl alcohol, acetone, and then twice in water, with each solvent step taking 15 minutes, then being dried under a stream of air.

3.2.2 Synthesis of $CoSb_2O_6$.

In order to prepare $CoSb_2O_6$, a film composed of $Co(OH)_2$ and Sb was first electrodeposited as the precursor film. Electrodeposition was carried out using a VMP2 multichannel potentiostat (Princeton Applied Research) in an undivided 3 electrode cell composed of a FTO working electrode, a Ag/AgCl (4 M KCl) reference electrode and a Pt counter electrode. The FTO electrode was masked off to a geometric surface area of 0.5 cm^2 with insulating tape (3M, electroplating tape 470).[28] This had the outcome of removing edge effects and improving the uniformity of the film. An aqueous solution containing 43 mM $CoCl_2 \cdot 6H_2O$, 11.5 mM $K_2Sb_2(C_4H_2O_6)_2 \cdot H_2O$, and 400 mM KNO_3 was used as the plating solution. The precursor film was deposited at -1.35 V vs Ag/AgCl by passing 0.4 C/cm^2. The as-deposited amorphous precursor films were converted to crystalline $CoSb_2O_6$ by annealing at 700 °C for 3 hours in air (ramping

rate = 2.3 °C/min). After the three hours of anneal time, the films were left to cool down to room temperature for approximately three hours within the furnace.

3.2.3 Characterization.

The sole presence of the AB_2O_6 crystalline phase was confirmed via powder X-ray diffraction (PXRD, D8 Discover, Bruker, Ni-filtered Cu Kα radiation, λ = 1.5418 Å). The surface morphology and elemental composition of the electrodes was characterized with scanning electron microscopy (SEM; LEO Supra55 VP) and energy dispersive spectroscopy (EDS; Noran System Seven, Thermo-Fisher, ultra-dry silicon drift detector) using an accelerating voltage of 2 keV for SEM and 20 keV for EDS. The elemental ratios were calculated using the Thermo Scientific NSS software package (Filter without Standards Quant Fit method and the Proza correction method). Since the Lα signal of Sn (3.443 keV) from the FTO substrate partially overlaps with the Lα signal of Sb (3.604 keV) from the samples preventing accurate quantification of the sample compositions, powder samples obtained by scrapping the as-deposited films off the FTO substrate were attached to carbon tape and used for EDS analysis. The elemental analyses of the samples were also performed using inductively coupled plasma mass spectrometry (ICP-MS) (Shimadzu ICP Mass Spectrometer-2030) using the solutions obtained by dissolving the as-deposited films in 0.5 M H_2SO_4. Calibration curves were created using the cobalt and antimony ICP standards diluted with 0.5 M H_2SO_4. ICP-MS was also used to quantify metal ions dissolved in the electrolyte during a 24 V-t measurement to evaluate the electrochemical stability of the samples. Surface elemental compositions were determined with X-ray photoelectron spectroscopy (XPS) using a Thermo Scientific K-α X-ray photoelectron spectrometer equipped with an Al Kα excitation source. The peak binding energies were calibrated to the adventitious C_{1s} peak at 284.8 eV. The surface elemental ratios were calculated using the Thermo Avantage Software package (ALThermo1

library for sensitivity factors, TPP-2m IMFF for energy correction, and a modified Shirley background for background correction).

3.2.4 Electrochemical characterization.

Electrochemical measurements were performed using either a VMP2 multichannel potentiostat (Princeton Applied Research) or an SP-200 potentiostat/EIS (Bio-Logic Science Instrument). The working electrode of $CoSb_2O_6$ was masked with epoxy (Devcon) to a working geometric surface area of ~0.15 cm^2. An undivided three-electrode cell containing a working electrode of $CoSb_2O_6$, a Ag/AgCl (4 M KCl) reference electrode, and a Pt counter electrode was used for characterization unless otherwise noted.

Linear sweep voltammetry's (LSVs) were performed at a scan rate of 10 mV/s by sweeping the potential in the positive direction from the open circuit potential. All LSVs shown in this study were corrected for the uncompensated solution resistance (R_u) after each experiment, which ranged from 2 and 5 Ohms. The R_u was determined by electrochemical impedance spectroscopy (EIS) where impedance was measured at 1.85 V vs RHE with a frequency range of 100 kHz to 1 Hz and a sinusoidal amplitude of 10 mV with a planar Pt electrode.[19,22,29] The electrochemically active surface area (ECSA) of $CoSb_2O_6$ and $MnSb_2O_6$ electrodes was estimated using the impedance of each electrode obtained under the aforementioned conditions by fitting with a modified Randles circuit composed of a parallel combination of a resistor and a constant phase element in series with a resistor.[22]

Galvanostatic water oxidation was performed at 10 mA/cm^2. All electrochemical experiments were performed in 0.5 M H_2SO_4 (pH 0.3) unless otherwise noted and without agitation (except for the galvanostatic water oxidation experiments where stirring was used to assist in removal of bubbles forming on the electrode surface). The Faradaic efficiency (FE) for O_2

evolution was determined using a custom designed, air-tight, two compartment, glass cell with a smaller Ag/AgCl (3 M NaCl) reference electrode. O_2 gas generated was detected using an Ocean Optics fluorescence-based oxygen sensor (Neofox FOSPOR-R). The oxygen sensor measured the O_2 content in the headspace as mole %. This was converted to μmol after first adjusting for the O_2 dissolved in solution using Henry's Law. The overall FE for O_2 evolution was calculated by the following equation:

$$\text{FE } (\%) = \frac{4 \text{ x } n_{O_2}(\text{mol}) \text{ x F } (\text{C mol}^{-1})}{\text{Total charged passed } (\text{C})} \text{ x } 100$$

While a Ag/AgCl reference was used in each experiment performed, all results within this report are presented against the reversible hydrogen electrode (RHE) for direct comparison to other reports in aqueous solution but that contain different pH values. The conversion between Ag/AgCl and RHE reference electrode values can be done via the following equation:

$$E_{(\text{vs RHE})} = E_{(\text{vs Ag/AgCl})} + E_{(\text{Ag/AgCl})}(\text{reference}) + 0.0591 \text{ V x pH(at 25 °C)}$$

$$E_{\text{Ag/AgCl}}(\text{reference, 4 M KCl}) = 0.1976 \text{ V vs NHE at 25 °C}$$

$$E_{\text{Ag/AgCl}}(\text{reference, 3 M NaCl}) = 0.209 \text{ V vs NHE at 25 °C}$$

3.3 Results and Discussion

3.3.1 Synthesis, Characterization, and OER performance of $CoSb_2O_6$.

The $CoSb_2O_6$ electrodes used for this study were synthesized via an electrochemical co-deposition of cobalt hydroxide and antimony metal using a plating solution composed of potassium antimony tartrate, cobalt chloride, and potassium nitrate. The Co was co-deposited not as Co metal

but as $Co(OH)_2$ because the reduction potential of Co^{2+} to Co^0 is more negative than that of Sb^{3+} to Sb^0.[15] Under the potential used to deposit Sb, nitrate is reduced to nitrite as shown by the equation below:[30]

$$NO_3^- + H_2O + 2e^- \rightleftharpoons NO_2^- + 2OH^-$$

The OH^- produced by this reaction increases the local pH at the WE surface, decreasing the solubility of Co^{2+}, and results in the precipitation of Co^{2+} as $Co(OH)_2$. The deposition potential and the Co:Sb ratio in the plating solution were adjusted such that the Co:Sb ratio in the as-deposited film is exactly and uniformly 1:2 throughout the films, which was confirmed by energy dispersive X-ray spectroscopy (EDS). The bulk Co:Sb ratio of the as-deposited film was additionally confirmed to be 1:2 using inductively coupled plasma mass spectrometry (ICP-MS) of the solution obtained by the dissolution of the entire as-deposited film in 0.5 M H_2SO_4.

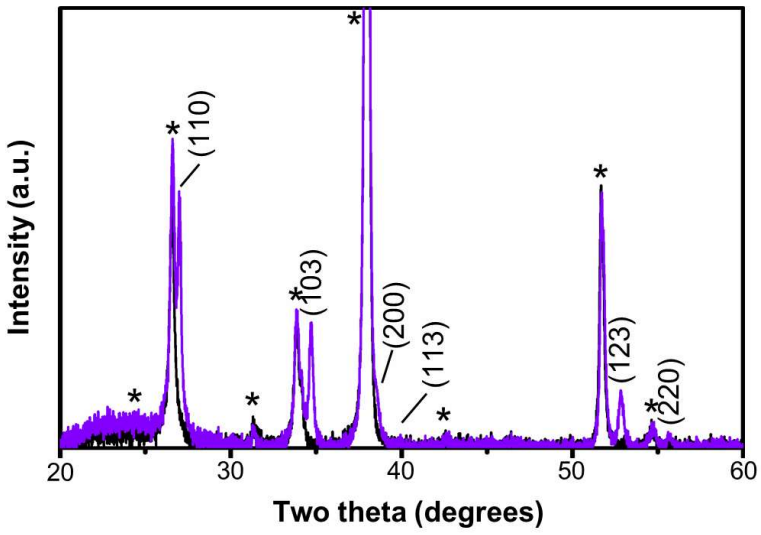

Figure 1. XRD patterns of as deposited (black) on FTO and the corresponding post annealed $CoSb_2O_6$ (purple). The (hkl) indices are assigned from the PDF card for $CoSb_2O_6$ (00-018-0403). The peaks corresponding to the FTO substrate are denoted by an asterisk.

The as-deposited amorphous films were converted to crystalline $CoSb_2O_6$ by annealing in air for three hours at 700 °C (**Figure 1**). Using EDS the Co:Sb ratios were confirmed to remain as 1:2 after annealing. The X-ray diffraction (XRD) pattern of the resulting $CoSb_2O_6$ films are shown in **Figure 1**. Since these films are very thin (~600 nm for $CoSb_2O_6$) and are composed of nanocrystals (**Figure 2a**), the intensities of the peaks generated by these films were low compared with those from the FTO substrate. I would like to note that any attempt to grow a thicker film resulted in the formation of films with less uniform Co:Sb ratios throughout the films. The SEM images show the uniform nature of the $CoSb_2O_6$ films produced by the newly developed electrodeposition method (**Figure 2b**).

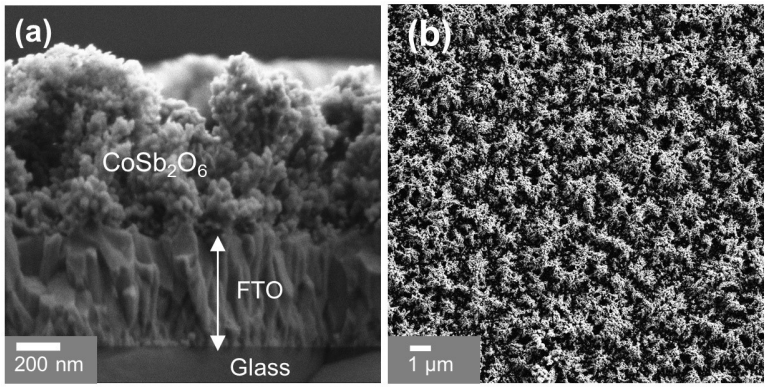

Figure 2. (a) Side view and (b) top down SEM images of $CoSb_2O_6$ after annealing.

The water oxidation performance of $CoSb_2O_6$ electrodes was investigated using linear sweep voltammetry (LSV) in 0.5 M H_2SO_4 (pH 0.3). In order to show the unambiguous effect of incorporating Co^{2+} into the Sb oxide matrix on the OER performance, the LSV of Sb_2O_4 ($Sb^{3+}Sb^{5+}O_4$) is also shown for comparison (**Figure 3**). Sb_2O_4 is the oxide that is obtained when antimony metal electrodeposited on FTO alone is annealed in the air using the same conditions to obtain crystalline $CoSb_2O_6$ electrodes. The LSV of Sb_2O_4 shows no anodic current when the potential was swept to 2.2 V vs. RHE, suggesting that it is inactive for the OER. On the other hand,

$CoSb_2O_6$ generated considerable anodic currents due to the OER, suggesting that its OER activity truly originates from the presence of Co in the compound. The overpotential required to achieve 10 mA/cm^2 was ~0.760 V for $CoSb_2O_6$.

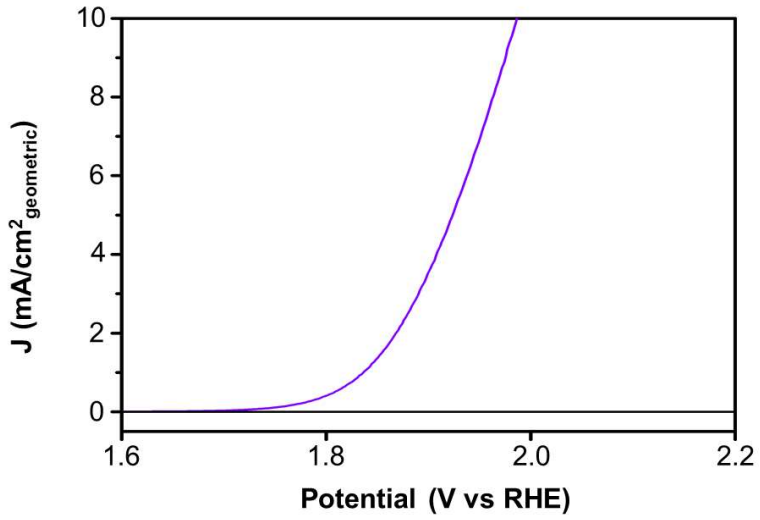

Figure 3. LSVs of $CoSb_2O_6$ (purple) and Sb_2O_4 (black) in 0.5 M H_2SO_4 (pH 0.3) with the current density determined using the geometric surface area of the electrode.

Comparing $CoSb_2O_6$ to $MnSb_2O_6$ from Chapter Two, $CoSb_2O_6$ appeared to be more active for the OER (**Figure 4a**). However, I note that the $CoSb_2O_6$ film used in this study was ~3 times thicker than the $MnSb_2O_6$ film, meaning that the surface area of the $CoSb_2O_6$ electrode is significantly higher than that of the $MnSb_2O_6$ electrode. This is because the thickness of the $CoSb_2O_6$ and $MnSb_2O_6$ electrodes used in these studies was individually optimized to obtain the purest composition for each sample. To eliminate the effect caused by the difference in surface area of these films, the electrochemically active surface area (ECSA) of the electrodes was determined using electrochemical impedance spectroscopy (EIS) and the resulting Nyquist plots (**Figure 5**).

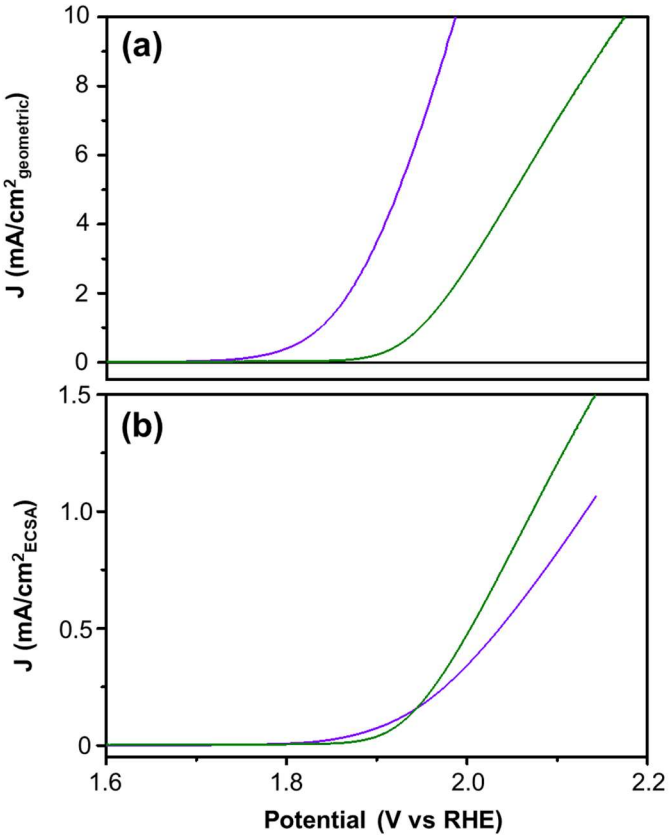

Figure 4. (a) LSVs of $CoSb_2O_6$ (purple), $MnSb_2O_6$ (green), and Sb_2O_4 (black) in 0.5 M H_2SO_4 (pH 0.3) with the current density determined using the geometric surface area of the electrode. (b) LSVs of $CoSb_2O_6$ (purple) and $MnSb_2O_6$ (green) with the current density determined using the electrochemically active surface areas.

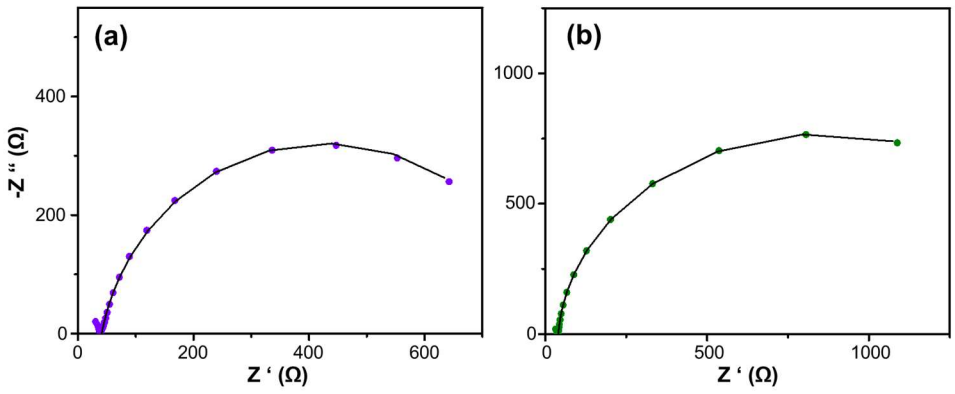

Figure 5. Nyquist plots for (a) $CoSb_2O_6$ and (b) $MnSb_2O_6$ taken in 0.5 M H_2SO_4 with the raw data displayed as colored circles and the impedance model fit as a black line. The model fit is derived from a modified Randles circuit composed of a constant phase element and resistor in parallel with each other and in series with another resistor.

The EIS results showed that the roughness factors of the $CoSb_2O_6$ and $MnSb_2O_6$ electrodes were ~18 and ~6, respectively. Using these values, the current densities were recalculated and LSVs were re-plotted in **Figure 4b**. The ECSA-adjusted LSVs show that although $CoSb_2O_6$ has a slightly earlier onset, $MnSb_2O_6$ shows a greater rise in current density as the potential is swept more positively, indicating that $MnSb_2O_6$ is intrinsically more active for the OER in the potential region to generate a sufficient amount of current. However, the data also suggests that the difference in their intrinsic performance is not significant and a higher current density towards the OER can be achieved by $CoSb_2O_6$ when it is prepared as a higher surface area electrode.

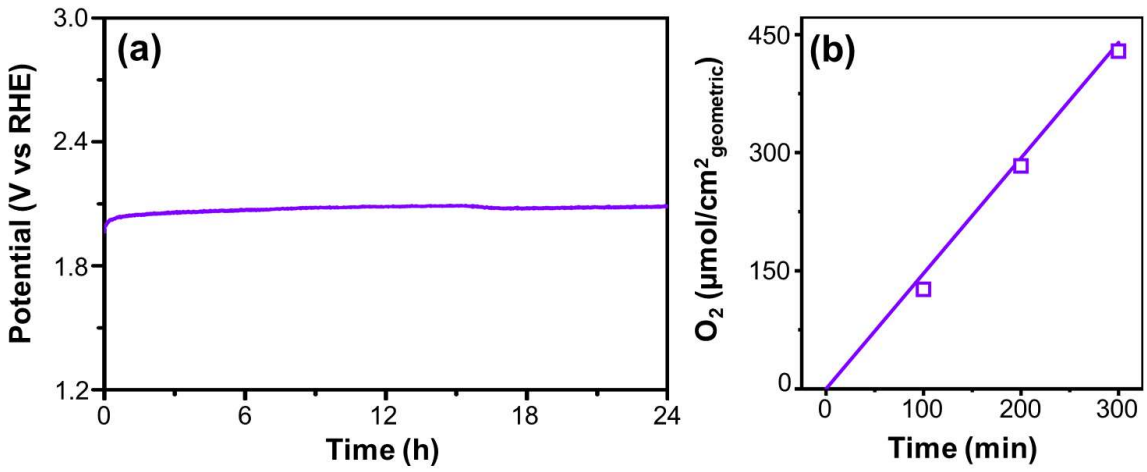

Figure 6. (a) The V-t plot of $CoSb_2O_6$ obtained for galvanostatic water oxidation at 10 mA/cm^2 in 0.5 M H_2SO_4 (pH 0.3). (b) Oxygen produced by $CoSb_2O_6$ electrodes during galvanostatic water oxidation at 10 mA/cm^2 in 0.5 M H_2SO_4 (pH 0.3) (open squares). The theoretically expected amount of oxygen assuming 100% FE is shown as a solid line.

The stability of $CoSb_2O_6$ during the OER in acidic media was first examined under galvanostatic water oxidation at 10 mA/cm^2 by recording the change in the potential required to maintain this current density over 24 h (**Figure 6a).** The result showed negligible change in the required potential for $CoSb_2O_6$. I confirmed that the current generated during this experiment was truly associated with O_2 production by calculating the Faradic efficiency (FE) for O_2 production

by comparing the amount of O_2 detected and the amount O_2 theoretically calculated assuming 100 % FE (**Figure 6b**). The FE for O_2 production of $CoSb_2O_6$ was 98% at 300 min. I note that the overpotentials required to achieve 10 mA/cm^2 by $CoSb_2O_6$ is significantly higher than that of state-of-the-art catalysts in acidic or basic conditions.[22,23] For example, iridium oxide-based OER catalysts can achieve 10 mA/cm^2 with an overpotential of 0.20 V – 0.35 V.[25,31-33]

3.3.2 Post OER Analysis.

Although the V-t plot suggested the stability of $CoSb_2O_6$ during the OER, the work done by Moreno-Hernandez *et al.* on other M-Sb_2O_6 compounds and the results on $MnSb_2O_6$ from Chapter Two clearly demonstrated that stable V-t performance does not necessarily mean that the catalyst is stable. The stochiometric, phase-pure $MnSb_2O_6$ from Chapter Two lost more than 50% of its Mn by dissolution during the V-t measurement but this severe corrosion did not affect the required potential to generate 10 mA/cm^2 over 24 h. Thus, I performed careful post analysis of the $CoSb_2O_6$ films using various techniques after the 24 h V-t measurement at 10 mA/cm^2 to examine for any possible signs of corrosion. **Figure 7** shows the XRD patterns before and after the V-t measurement, with an inset showing the lack of intensity change of the most representative and intense peak for $CoSb_2O_6$. The (110) peak of $CoSb_2O_6$ showed no difference in intensity before and after the V-t measurement. SEM images of these electrodes taken after the V-t measurement (**Figure 8**) agree well with the XRD patterns; no noticeable morphological changes were observed for $CoSb_2O_6$. The EDS analysis of $CoSb_2O_6$ showed that the Co:Sb ratio remained 1:2.

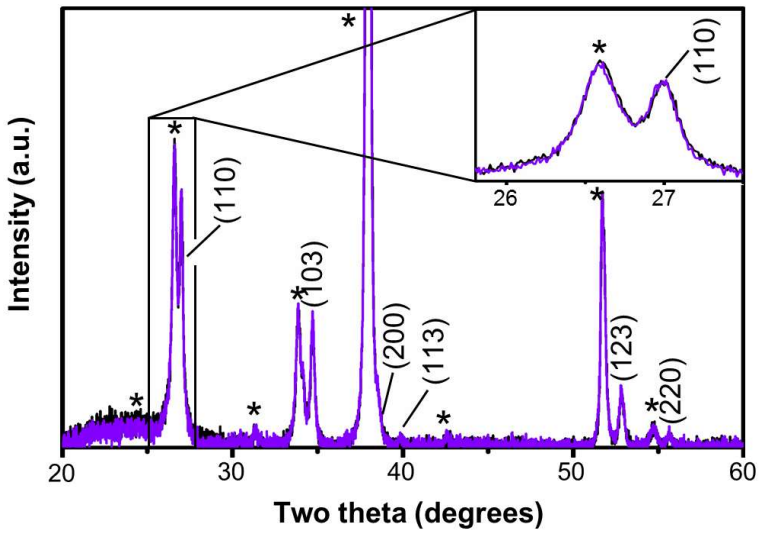

Figure 7. XRD pattern of $CoSb_2O_6$ electrodes after a 24 h V-t measurement (purple) at 10 mA/cm^2. The XRD pattern of the corresponding film before the V-t measurement is shown in black for comparison. An inset is provided to show the lack of change in peak intensity after the V-t measurement. The peaks corresponding to the FTO substrate are denoted by an asterisk.

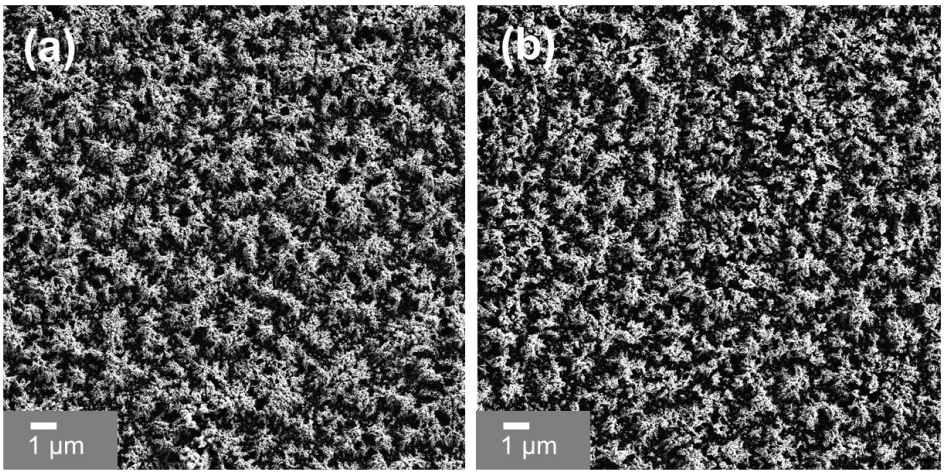

Figure 8. Top-vew SEM images of $CoSb_2O_6$ (a) before and (b) after the galvanostatic water oxidation at 10 mA/cm^2 for 24 h.

I also performed X-ray photoelectron spectroscopy (XPS) before and after the V-t measurement to probe for changes in the oxidation states of the constituent elements on the $CoSb_2O_6$ electrode surface. The Co 2p region of $CoSb_2O_6$ is shown in **Figure 9a** and is composed

of $2p_{2/3}$, $2p_{1/2}$, and their satellite peaks that have all been normalized with respect to the Sb 3d region. I used the $2p_{1/2}$ peak to examine the oxidation state of Co in $CoSb_2O_6$ because the position of the $2p_{1/2}$ peak and its satellite moves more drastically with changes in oxidation state than that of the $2p_{3/2}$ peak.[34,35] For an oxide containing only Co^{2+} the $2p_{1/2}$ peak is expected to appear at 796.6 eV, with a satellite feature at 802.3 eV, while one containing only Co^{3+} will have the $2p_{1/2}$ peak at 794.8 eV with a satellite feature at 804.3 eV. For the pristine $CoSb_2O_6$ electrode the $2p_{1/2}$ peak was centered at 796.7 eV and the satellite peak at 802.8 eV, indicating the presence of Co^{2+} at the surface, which is also the oxidation state of Co in the bulk $CoSb_2O_6$.[34,35]

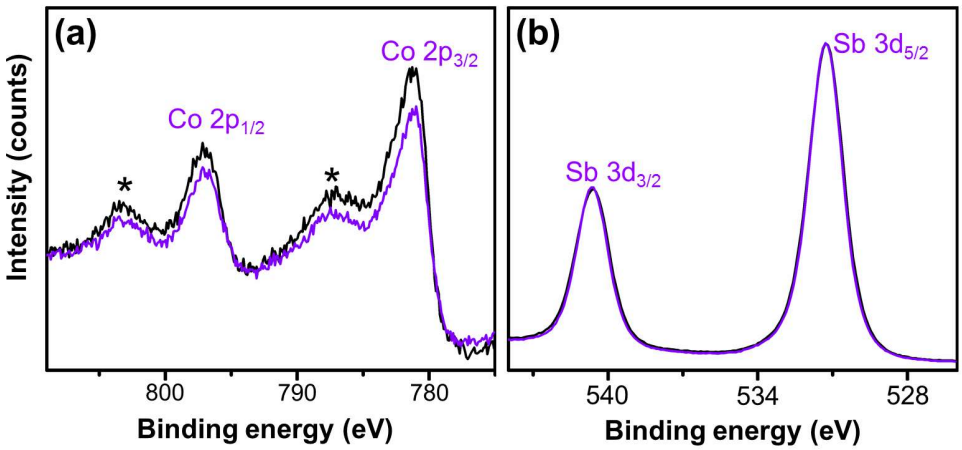

Figure 9. XPS of the (a) Co 2p and (b) Sb 3d regions of $CoSb_2O_6$ before (black) and after (purple) the V-t measurement at 10 mA/cm^2 for 24 h. The asterisks in the Co 2p spectra denote satellite peaks.

However, a small decrease in the Co 2p region intensity occurred, indicating a small decrease in the relative amount of Co on the surface compared to Sb. The surface Co:Sb ratio before the V-t measurement was 1:2.07, very close to the bulk elemental ratio of 1:2. After the V-t measurement, the surface Co:Sb ratio was 1:2.29 suggesting a slight loss of Co from the outer most surface layer. I note that this surface Co:Sb ratio is still close to the bulk Co:Sb ratio of

$CoSb_2O_6$. For comparison, the Co:Sb ratios of the Sb-rich $CoSb_2O_6$ prepared by Moreno-Hernandez *et al*. were 1:4.0 and 1:4.5 before and after the V-t measurements, respectively.[21]

The Sb 3d region of $CoSb_2O_6$ is shown in **Figure 9b.** The $3d_{5/2}$ peak in this plot overlaps with the O 1s peak.[36,37] Thus, the Sb $3d_{3/2}$ peak was used to examine the oxidation state of Sb on the $CoSb_2O_6$ surface. For the Sb $3d_{3/2}$ peak, Sb^{3+} oxides show a peak at a binding energy of 539.6 eV, Sb^{5+} oxides at 540.6 eV, and an even mixture ($Sb^{3+}Sb^{5+}O_2$) at a binding energy in-between at 540.0 eV. The Sb $3d_{3/2}$ peak of the pristine $CoSb_2O_6$ electrode is centered at 540.5 eV, which indicates a surface that is primarily Sb^{5+} in nature.[36,37] After the 24 hour V-t measurement, the Sb $3d_{3/2}$ peak shifted to 540.6 eV, indicating an increase of Sb^{5+} character to that of the pure Sb^{5+} oxide phase. I note that the as-prepared Sb-rich $CoSb_{2.2}O_6$ prepared by Moreno-Hernandez *et al* showed the Sb $3d_{3/2}$ peak at 539.7 eV, meaning that it contains a considerable amount of Sb^{3+} on the surface compared with the stoichiometric $CoSb_2O_6$ prepared here.[21]

When I examined the electrolyte used for the V-t measurement of $CoSb_2O_6$ using ICP-MS, I found only 8.1% of the Co and 2.2% of the Sb in $CoSb_2O_6$ electrode were dissolved during the V-t measurement. I think that this level of dissolution is caused by the dissolution of amorphous or less crystalline $CoSb_2O_6$ present at the surface of nanocrystalline $CoSb_2O_6$ electrodes, which explains why I observed no changes in the XRD patterns and SEM images of $CoSb_2O_6$ before and after the V-t measurement. Considering over 60% of the $MnSb_2O_6$ electrode from Chapter Two had dissolved during the same 24 hour V-t measurement, while the $CoSb_2O_6$ electrode had less than 10% Co loss, is indicative of significantly enhanced corrosion resistance when Mn is replaced with Co in the Sb^{5+} oxide lattice. This provides strong evidence that tuning the elemental composition of a Sb^{5+} containing metal oxide may lead to the development of a more active and stable material for use as an OER catalyst in acidic media.

The post OER analysis shows $CoSb_2O_6$ prepared as a stoichiometric, phase-pure compound appears to be stable. As I mentioned previously, the performance of $CoSb_2O_6$ is not good enough to replace state-of-the-art OER catalysts in acidic media, as to achieve realistic OER current densities that are used in state-of-the-art electrolyzers (>100 mA/cm2) even higher voltages are required (**Figure 10**). Thus, future work will focus on the identification of oxide compositions where the atomic ratio of catalytically active metal to metal that provides a structural stability can be increased while retaining the stability of the compound in acidic media.

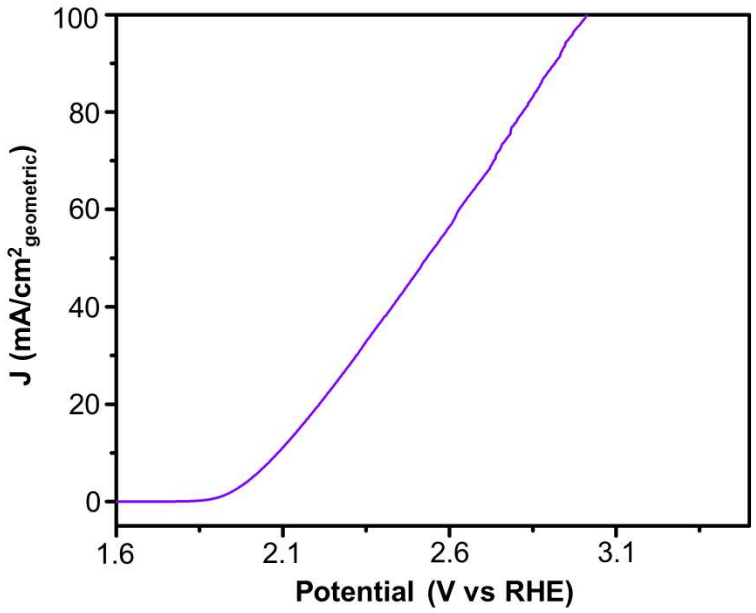

Figure 10. LSV of $CoSb_2O_6$ in 0.5 M H_2SO_4 (pH 0.3) demonstrating the required potential to reach 100 mA/cm^2 for the electrode, with the current density determined using the geometric surface area of the electrode.

2.3.3 Activity for the CER

The recent work by Moreno-Hernandez *et al.* also suggested the possibility of using $CoSb_{2.2}O_x$ for chloride oxidation to form chlorine gas (Cl_2 (g) + 2e$^-$ ⇌ 2Cl$^-$, E^o = 1.39 V vs SHE) using a 4 M NaCl solution adjusted to be slightly acidic (pH 2).[21] The optimum electrolyte for the chlorine evolution reaction (CER) requires high concentrations of Cl$^-$ ions (~4 M NaCl) and low

pH conditions (pH 2 - 4).[38,39] This combined with the anodic bias required for the CER significantly reduces the type of materials that can stably perform the CER.

In their study, $CoSb_{2.2}O_x$ was reported to be able to selectively generate 100 mA/cm^2 for chloride oxidation over 250 hours with minimal corrosion into solution.[21] $MnSb_{1.7}O_x$ also showed enhanced ability to oxidize chloride over water oxidation, however, it demonstrated significant water oxidation current before reaching 100 mA/cm^2 for chloride oxidation. Since the compounds used in this study did not have the same M:Sb stoichiometry, I wondered whether the observed difference in chloride oxidation performance was solely due to the difference in M or due to the Sb-rich and Sb-poor natures of $CoSb_{2.2}O_x$ and $MnSb_{1.7}O_x$, respectively.

Thus, I compared the CER and OER of my stoichiometric $CoSb_2O_6$ and $MnSb_2O_6$ electrodes using the conditions used by the previous study to provide a more comprehensive understanding of the composition-property relationship of the MSb_2O_6 system. The LSVs obtained in 4 M NaCl with the pH adjusted to 2 for chloride oxidation and pH 2 H_2SO_4 for water oxidation, respectively, are shown in **Figure 11**. Both $CoSb_2O_6$ and $MnSb_2O_6$ showed significantly enhanced activity towards chloride oxidation over water oxidation. $CoSb_2O_6$ also demonstrated an earlier onset and a higher current density than $MnSb_2O_6$ when either the geometric surface area or ECSA was used to calculate current density. This means that even when these electrodes are prepared as stoichiometric compounds, $CoSb_2O_6$ is more active for chloride oxidation than $MnSb_2O_6$. However, for the stoichiometric $CoSb_2O_6$ electrodes prepared here non-negligible water oxidation occurred at potentials required to reach 100 mA/cm^2 for chloride oxidation, while water oxidation was completely suppressed when $CoSb_{2.2}O_x$ was used to generate 100 mA/cm^2 for chloride oxidation in the previous study.[21] This is because my stoichiometric $CoSb_2O_6$ can perform water

oxidation better than the Sb-rich $CoSb_{2.2}O_x$. This result suggests that the surface non-stoichiometry of the $CoSb_{2.2}O_x$ electrode is critical for making this electrode more selective for the CER.

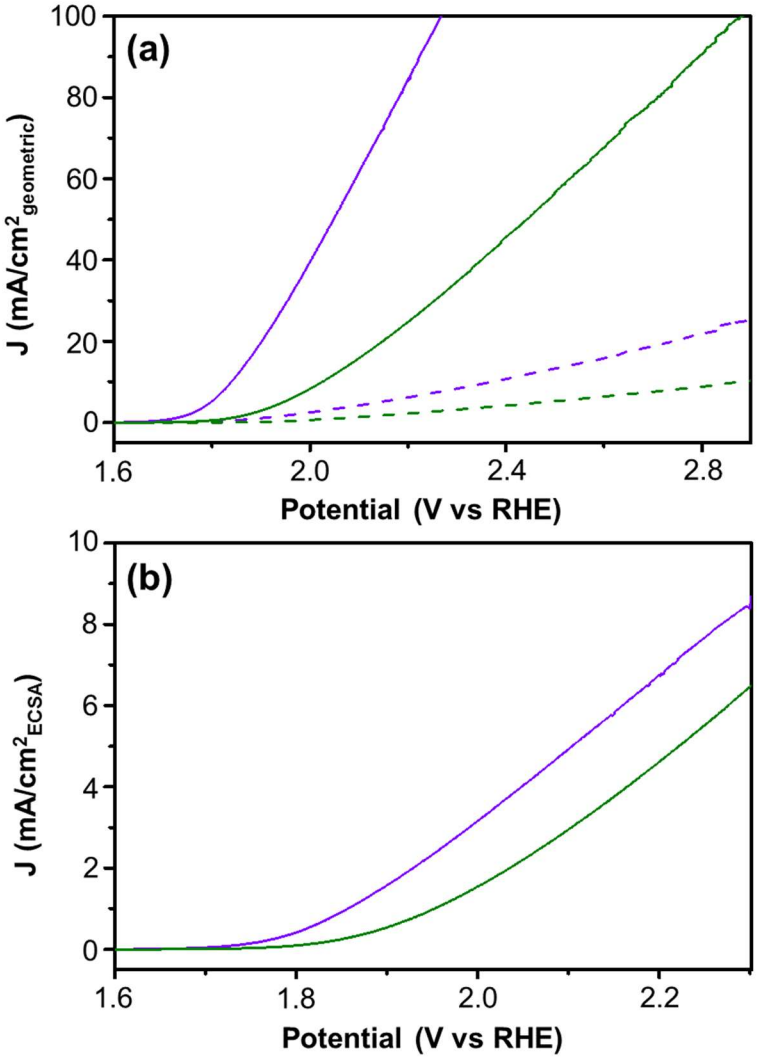

Figure 11. (a) LSVs of $CoSb_2O_6$ (purple) and $MnSb_2O_6$ (green) electrodes with the current density determined by the geometric surface area of the electrode obtained in pH 2, 4 M NaCl (solid) and in pH 2 H_2SO_4 (dashed). (b) Comparison of LSVs of $CoSb_2O_6$ (purple) and $MnSb_2O_6$ (green) with current density determined by the electrochemically active surface area.

3.4 Conclusion

A new electrochemical method to synthesize stoichiometric, phase-pure $CoSb_2O_6$ electrodes has been developed for investigation of their ability to oxidize water in acidic media. $CoSb_2O_6$ showed stable V-t performance during the OER at 10 mA/cm^2 over the course of a 24 hour V-t measurement. Careful post OER analysis that examined changes in morphology, crystallinity, and surface composition demonstrated that crystalline, phase-pure $CoSb_2O_6$ is stable with a minimal loss of Co and Sb from the less crystalline region on the surface that did not affect the bulk crystallinity and morphology. The catalytic performance of the stoichiometric, phase-pure $CoSb_2O_6$ is not sufficient to replace current state-of-the-art IrO_x and RuO_x catalysts in acidic media. However, the study of $CoSb_2O_6$ demonstrated a possibility of producing an acid-stable ternary oxide containing a non-noble, OER active element, encouraging further development of practical acid-stable OER catalysts. I also examined the CER performance of $CoSb_2O_6$ and found that it is more active for the CER than the OER in 4 M NaCl (pH 2), agreeing with a previous report on non-stoichiometric $CoSb_2O_6$. However, the stoichiometric, phase-pure compound exhibited appreciable water oxidation current under the potential required to generate 100 mA/cm^2 for the CER, indicating surface stoichiometry plays an important role in the activity towards the CER and OER.

3.5 References

1. Crabtree, G. W.; Dresselhaus, M. S., The Hydrogen Fuel Alternative. *MRS Bull.* **2011**, *33*, 421-428.

2. Formal, F. L.; Bourée, W. S.; Prévot, M. S.; Sivula, K., Challenges towards Economic Fuel Generation from Renewable Electricity: The Need for Efficient Electro-Catalysis. *Chimia* **2015**, *69*, 789-798.

3. Levene, J. I.; Mann, M. K.; Margolis, R. M.; Milbrandt, A., An analysis of hydrogen production from renewable electricity sources. *Sol. Energy* **2007**, *81*, 773-780.

4. Dau, H.; Limberg, C.; Reier, T.; Risch, M.; Roggan, S.; Strasser, P., The Mechanism of Water Oxidation: From Electrolysis via Homogeneous to Biological Catalysis. *ChemCatChem* **2010**, *2*, 724-761.

5. Man, I. C.; Su, H.-Y.; Calle-Vallejo, F.; Hansen, H. A.; Martínez, J. I.; Inoglu, N. G.; Kitchin, J.; Jaramillo, T. F.; Nørskov, J. K.; Rossmeisl, J., Universality in Oxygen Evolution Electrocatalysis on Oxide Surfaces. *ChemCatChem* **2011**, *3*, 1159-1165.

6. Jamesh, M.-I.; Sun, X., Recent progress on earth abundant electrocatalysts for oxygen evolution reaction (OER) in alkaline medium to achieve efficient water splitting – A review. *J. Power Sources* **2018**, *400*, 31-68.

7. Jung, S.; McCrory, C. C. L.; Ferrer, I. M.; Peters, J. C.; Jaramillo, T. F., Benchmarking nanoparticulate metal oxide electrocatalysts for the alkaline water oxidation reaction. *J. Mater. Chem. A* **2016**, *4*, 3068-3076.

8. Lee, Y.; Suntivich, J.; May, K. J.; Perry, E. E.; Shao-Horn, Y., Synthesis and Activities of Rutile IrO2 and RuO2 Nanoparticles for Oxygen Evolution in Acid and Alkaline Solutions. *J. Phys. Chem. Lett.* **2012**, *3*, 399-404.

9. Abbott, D. F.; Lebedev, D.; Waltar, K.; Povia, M.; Nachtegaal, M.; Fabbri, E.; Coperet, C.; Schmidt, T. J., Iridium Oxide for the Oxygen Evolution Reaction: Correlation between Particle Size, Morphology, and the Surface Hydroxo Layer from Operando XAS. *Chem. Mater.* **2016**, *28*, 6591-6604.

10. Reier, T.; Oezaslan, M.; Strasser, P., Electrocatalytic Oxygen Evolution Reaction (OER) on Ru, Ir, and Pt Catalysts: A Comparative Study of Nanoparticles and Bulk Materials. *ACS Catal.* **2012**, *2*, 1765-1772.

11. Cherevko, S.; Zeradjanin, A. R.; Topalov, A. A.; Kulyk, N.; Katsounaros, I.; Mayrhofer, K. J. J., Dissolution of Noble Metals during Oxygen Evolution in Acidic Media. *Chemcatchem* **2014**, *6*, 2219-2223.

12. Jovanovič, P.; Hodnik, N.; Ruiz-Zepeda, F.; Arčon, I.; Jozinović, B.; Zorko, M.; Bele, M.; Šala, M.; Šelih, V. S.; Hočevar, S.; Gaberšček, M., Electrochemical Dissolution of Iridium and Iridium Oxide Particles in Acidic Media: Transmission Electron Microscopy, Electrochemical Flow Cell Coupled to Inductively Coupled Plasma Mass Spectrometry, and X-ray Absorption Spectroscopy Study. *J. Am. Chem. Soc.* **2017**, *139*, 12837-12846.

13. Hodnik, N.; Jovanovič, P.; Pavlišič, A.; Jozinović, B.; Zorko, M.; Bele, M.; Šelih, V. S.; Šala, M.; Hočevar, S.; Gaberšček, M., New Insights into Corrosion of Ruthenium and Ruthenium Oxide Nanoparticles in Acidic Media. *J. Phys. Chem. C* **2015**, *119*, 10140-10147.

14. Carmo, M.; Fritz, D. L.; Mergel, J.; Stolten, D., A comprehensive review on PEM water electrolysis. *Int. J. Hydrog. Energy* **2013**, *38*, 4901-4934.

15. Pourbaix, M., *Atlas of Electrochemical Equilibria in Aqueous Solutions.* 2 ed.; National Association of Corrosion Engineers: Houston, Texas, **1974**; p 524-532.

16. Tigau, N.; Ciupina, V.; Prodan, G., Structural, optical and electrical properties of Sb_2O_3 thin films with different thickness. *J. Optoelectron. Adv. Mater.* **2006**, *8*, 37-42.

17. Ozawa, K.; Sakka, Y.; Amano, M., Preparation and electrical conductivity of three types of antimonic acid films. *J. Mater. Res.* **1998**, *13*, 830-833.

18. Herrmann, J. M. J.; Portefaix, J. L.; Forissier, M.; Figueras, F.; Pichat, P., Electrical Behavior of Powdered Tin-Antimony Mixed-Oxide Catalysts. *J. Chem. Soc. Faraday T. 1* **1979**, *75*, 1346-1355.

19. Moreno-Hernandez, I. A.; MacFarland, C. A.; Read, C. G.; Papadantonakis, K. M.; Brunschwig, B. S.; Lewis, N. S., Crystalline nickel manganese antimonate as a stable water-oxidation catalyst in aqueous 1.0 M H_2SO_4. *Energ. Environ. Sci.* **2017**, *10*, 2103-2108.

20. Zhou, L.; Shinde, A.; Montoya, J. H.; Singh, A.; Gul, S.; Yano, J.; Ye, Y.; Crumlin, E. J.; Richter, M. H.; Cooper, J. K.; Stein, H. S.; Haber, J. A.; Persson, K. A.; Gregoire, J. M., Rutile Alloys in the Mn–Sb–O System Stabilize Mn3+ To Enable Oxygen Evolution in Strong Acid. *ACS Catal.* **2018**, *8*, 10938-10948.

21. Moreno-Hernandez, I. A.; Brunschwig, B. S.; Lewis, N. S., Crystalline nickel, cobalt, and manganese antimonates as electrocatalysts for the chlorine evolution reaction. *Energ. Environ. Sci.* **2019**, *12*, 1241-1248.

22. McCrory, C. C. L.; Jung, S.; Peters, J. C.; Jaramillo, T. F., Benchmarking Heterogeneous Electrocatalysts for the Oxygen Evolution Reaction. *J. Am. Chem. Soc.* **2013**, *135*, 16977-16987.

23. Hunter, B. M.; Gray, H. B.; Müller, A. M., Earth-Abundant Heterogeneous Water Oxidation Catalysts. *Chem*. *Rev*. **2016**, *116*, 14120-14136.

24. Gerken, J. B.; McAlpin, J. G.; Chen, J. Y. C.; Rigsby, M. L.; Casey, W. H.; Britt, R. D.; Stahl, S. S., Electrochemical Water Oxidation with Cobalt-Based Electrocatalysts from pH 0–14: The Thermodynamic Basis for Catalyst Structure, Stability, and Activity. *J. Am. Chem. Soc.* **2011**, *133*, 14431-14442.

25. Mondschein, J. S.; Callejas, J. F.; Read, C. G.; Chen, J. Y. C.; Holder, C. F.; Badding, C. K.; Schaak, R. E., Crystalline Cobalt Oxide Films for Sustained Electrocatalytic Oxygen Evolution under Strongly Acidic Conditions. *Chemistry of Materials* **2017**, *29*, 950-957.

26. Yan, K.-L.; Chi, J.-Q.; Xie, J.-Y.; Dong, B.; Liu, Z.-Z.; Gao, W.-K.; Lin, J.-H.; Chai, Y.-M.; Liu, C.-G., Mesoporous Ag-doped Co3O4 nanowire arrays supported on FTO as efficient electrocatalysts for oxygen evolution reaction in acidic media. *Renew. Energy* **2018**, *119*, 54-61.

27. Yang, X.; Li, H.; Lu, A.-Y.; Min, S.; Idriss, Z.; Hedhili, M. N.; Huang, K.-W.; Idriss, H.; Li, L.-J., Highly acid-durable carbon coated Co3O4 nanoarrays as efficient oxygen evolution electrocatalysts. *Nano Energy* **2016**, *25*, 42-50.

28. Govindaraju, G. V.; Wheeler, G. P.; Lee, D.; Choi, K.-S., Methods for Electrochemical Synthesis and Photoelectrochemical Characterization for Photoelectrodes. *Chem. Mater.* 2017, *29*, 355-370.

29. Stevens, M. B.; Enman, L. J.; Batchellor, A. S.; Cosby, M. R.; Vise, A. E.; Trang, C. D. M.; Boettcher, S. W., Measurement Techniques for the Study of Thin Film Heterogeneous Water Oxidation Electrocatalysts. *Chem. Mater.* **2017**, *29*, 120-140.

30. Kang, D.; Kim, T. W.; Kubota, S. R.; Cardiel, A. C.; Cha, H. G.; Choi, K.-S., Electrochemical Synthesis of Photoelectrodes and Catalysts for Use in Solar Water Splitting. *Chem. Rev.* **2015**, *115*, 12839-12887.

31. Pearce, P. E.; Yang, C.; Iadecola, A.; Rodriguez-Carvajal, J.; Rousse, G.; Dedryvère, R.; Abakumov, A. M.; Giaume, D.; Deschamps, M.; Tarascon, J.-M.; Grimaud. Revealing the Reactivity of the Iridium Trioxide Intermediate for the Oxygen Evolution Reaction in Acidic Media. *Chem. Mater.* **2019**, *31*, 5845-5855.

32. Jiang, H.; Ge, S.; Zhang, Y.; Dong, M.; Wu, S.; Wu, M.; Zhang, J.; Ge, R.; Gua, Z., Self-Supported Iridum Oxide Nanostructures for Electrocatalytic Water Oxidation in Acidic Media. *J. Phys. Chem. C.* **2020**, *124*, 2-8.

33. Seitz, L. C.; Dickens, C. F.; Nishio, K.; Hikita, Y.; Montoya, J.; Doyle, A.; Kirk, C.; Vojvodic, A.; Hwang, H. Y.; Norskov, J. K.; Jaramillo, T. F., A highly active and stable $IrO_x/SrIrO_3$ catalyst for the oxygen evolution reaction. *Science*. **2016**, *353*, 1011-1014.

34. Biesinger, M. C.; Payne, B. P.; Grosvenor, A. P.; Lau, L. W. M.; Gerson, A. R.; Smart, R. S. C., Resolving surface chemical states in XPS analysis of first row transition metals, oxides and hydroxides: Cr, Mn, Fe, Co and Ni. *Appl. Surf. Sci.* **2011**, *257*, 2717-2730.

35. Foelske, A.; Strehblow, H.-H., Passivity of cobalt in borate buffer at pH 9.3 studied by x-ray photoelectron spectroscopy. *Surf. Interface Anal.* **2000**, *29*, 548-555.

36. Garbassi, F., XPS and AES study of antimony oxides. *Surf. Interface Anal.* **1980**, *2*, 165-169.

37. Izquierdo, R.; Sacher, E.; Yelon, A., X-ray photoelectron spectra of antimony oxides. *Appl. Surf. Sci.* **1989**, *40*, 175-177.

38. Brinkmann, T.; Giner-Santonja, G.; Schorcht, F.; Roudier, S.; Delgado Sancho, L., *Best Available Techniques (BAT) Reference Document for the Production of Chlor-alkali.* 2014, 13-17.

39. Karlsson, R. K. B.; Cornell, A. Selectivity between Oxygen and Chlorine Evolution in the Chlor-Alkali and Chlorate Processes. *Chem. Rev.* 2016. *116*, 2982-3028.

Chapter Four: Electrochemical Synthesis and Investigation of Bi- and Sb-containing Quaternary Metal Oxides as Photoelectrodes for Solar Water Splitting

4.1 Introduction

Photoelectrochemical (PEC) water splitting can provide a sustainable and environmentally benign route for the production of hydrogen gas for usage in fuel cells to generate electricity, for the synthesis of ammonia for fertilizer, and as a combustion fuel itself.[1-3] Ever since Honda and Fujishima demonstrated the PEC splitting of water using TiO_2 in 1972, significant effort has been put into the development of semiconductor electrodes to effectively capture the sun's energy to split water.[4] Through this effort, almost all of the simplest, binary metal oxides have been investigated for use as a photoelectrode in a PEC device. However, to this date, no binary metal oxide material has been able to effectively meet all the necessary requirements to be utilized in a wide-spread, commercially viable PEC device.

This lack of a suitable binary metal oxide material primarily stems from the difficulty in achieving a small enough bandgap, having rapid charge separation and transport and having good charge injection into the solution with the aid of a catalyst all in one electrode that is also chemically stable towards degradation from the electrolyte. Because binary oxides possess only one metal, the corresponding properties of the material are completely dependent on the nature of that one metal as an oxide, making it inherently difficult to optimize a material to possess the desired bandgap, charge separation and transport. CuO is a prime example of a binary metal oxide photoelectrode that possesses a small bandgap (~1.2 eV) and good absorption characteristics, however, it rapidly degrades through photocorrosion because of a lack of fast enough charge transport to prevent the material from destroying itself.[5,6] On the other hand, the binary metal oxide TiO_2 shows excellent resistance to chemical and photocorrosion in a variety of conditions, but has too large of a bandgap (~3.1 eV) to be used as a large scale viable photoelectrode.[7]

While many different methods have been investigated to improve the performance or stability of binary metal oxide systems to overcome the challenge of creating a stable and highly active photoelectrode, it is slowly becoming clear that more complex systems containing two or more metal ions may be required in order to achieve the necessary activity and stability profile for a commercially viable PEC device.[8-11] These ternary and quaternary metal oxide systems allow for more design flexibility in achieving both a stable and active material by using specific elements and their relative amounts within the material for specific roles, such as photon absorption and transport or as a stabilizing matrix. However, the multitude of possible combinations for a particular set of elements also leads to the primary challenge of designing a synthesis method to reliably produce the target stochiometric, phase pure compound while also avoiding producing undesired oxide phases as impurities. This is particularly true for quaternary species where it is possible to not only form multiple binary metal oxide impurities but also to form a variety of ternary metal oxide species impurities.

The many possible impurities within quaternary materials leads to an inherent difficulty in synthesizing a stochiometric and phase pure material. This has led to a very limited number of cursory reports on using quaternary metal oxide materials in solar water splitting.[12-14] These reports also commonly use solid state synthetic methods to manipulate the elemental ratios and thermodynamics of the synthesis. While this has the benefit of carefully controlling the reaction conditions to form the desired quaternary phase and avoid impurities, it typically leads to long synthesis times and requires the additional step of electrode preparation which can lead to issues of poor adhesion and conductivity.

To expand upon the limited library of synthetic methods and the number of quaternary metal oxides investigated for their solar water splitting capabilities, I report in this chapter a new

electrochemical preparation of a high surface area BiSb precursor film that can be used to prepare multiple quaternary metal oxides for investigation as photoelectrodes. Electrochemical deposition allows for good adhesion and effective charge transport properties by depositing the precursor film directly onto a conductive substrate. A Bi- and Sb-containing precursor was selected because of the cooperative stability profile that Bi and Sb oxides can provide. Based upon the Pourbaix diagram of Bi,[15] Bi-containing oxides can be stable under a wide range of neutral and basic pH conditions, lending good corrosion resistance in neutral and alkaline media for a quaternary photoelectrode. However, Bi oxides dissolve readily in acidic media. To circumvent this issue, Sb is used in tandem with Bi, as Sb(V)-containing oxides can be stable in acidic media.[15] This combination allows for a wide range of possible pH conditions that may be used to investigate a material's PEC performance.

Using the as-prepared metallic BiSb precursor film, a desired quaternary metal oxide phase can then be synthesized by drop-casting a target element on top followed by annealing in air. Seven different quaternary phases that contain Bi and Sb were investigated based upon their known existence in the literature: $MoBi_{1.1}Sb_{0.9}MoO_6$, Bi_2SbVO_6, $Mn_2Bi_3Sb_3O_{14}$, $WBiSbO_6$, $Zn_2Bi_3Sb_3O_{14}$, Fe_2BiSbO_7, and $Cu_2Bi_3Sb_3O_{14}$.[16-22] All but $MoBi_{1.1}Sb_{0.9}MoO_6$ and Bi_2SbVO_6 were successfully synthesized using this method. However, only $Cu_2Bi_3Sb_3O_{14}$ was able to be investigated for use as a photoelectrode and while its optical absorbance was promising, its low PEC performance indicates significant challenges exist to use these materials for solar water splitting.

4.2 Experimental

4.2.1 Materials

The following chemicals are grouped into three different sections: used for the synthesis of the BiSb precursor films, used for the drop-casting solutions and removal of residual oxide after annealing, or used for the characterization of the photoelectrodes. For the synthesis of the BiSb precursor films nitric acid (HNO_3, 70%), bismuth(III) nitrate ($Bi(NO_3)_3 \cdot 5H_2O$, ≥98.0%), and potassium antimony tartrate ($K_2Sb_2(C_4H_2O_6)_2 \cdot H_2O$, 99%) were purchased from Sigma-Aldrich, and L-(+)-tartaric acid ($C_4H_6O_6$, >99.5%) was purchased from Fluka. For the drop-casting of elements on the BiSb precursor films and the removal of the residual oxides hydrochloric acid (HCl, 37%), sulfuric acid (H_2SO_4, 95.0-98.0%), sodium hydroxide (NaOH, ≥97.0%), N,N-dimethylformamide ($(CH3)_2NC(O)H$, ≥99.8%), ammonium tetrathiomolybdate ($(NH_4)_2MoS_4$, 99.97%), ammonium tetrathiotungstate ($(NH_4)_2WS_4$, ≥99.9%), manganese chloride ($MnCl_2 \cdot 4H_2O$, ≥99%), and vanadyl acetylacetonate ($VO(C_5H_7O_2)_2$, 98%) were purchased from Sigma-Aldrich; iron(II) chloride ($FeCl_2 \cdot 4H_2O$, 98%) and zinc chloride ($ZnCl_2$, 98+%) were purchased from Alfa Aesar; copper(II) nitrate ($Cu(NO_3)_2 \cdot 3H_2O$, 99%) was purchased from Acros Organics; and dimethyl sulfoxide ($(CH_3)_2SO$, 99.9%) was purchased from VWR. For the characterization of the films, sodium sulfate (Na_2SO_4, >99%) was purchased from Dot Scientific, potassium phosphate monobasic (KH_2PO_4, >99.0%) was purchased from Electron Microscopy Sciences, and potassium hydroxide (KOH, ≥85%), sodium sulfite (Na_2SO_3, 98%) were purchased from Sigma-Aldrich. All of the above chemicals were used as received without further purification. Fluorine-doped tin oxide (FTO) on soda lime glass (Hartford Glass Co) was used as a working electrode for BiSb electrodeposition. FTO substrates were cleaned before the deposition by gently rubbing the surface with soapy water followed by four sonication steps for 15 min each using isopropyl alcohol, acetone and then two subsequent DI water solutions, after which the FTO slides was dried under

an air stream. A platinum counter electrode was prepared by e-beam evaporating a 20 nm layer of titanium as an adhesion layer on a glass slide, followed by a 100 nm thick layer of platinum. All solutions (unless otherwise stated) were prepared using deionized (DI) water with a resistivity of 18.2 MΩ·cm.

4.2.2 Synthesis of BiSb

The electrodeposition of BiSb was carried out using a VMP2 multichannel potentiostat (Princeton Applied Research) in an undivided three-electrode cell comprised of an FTO working electrode, a double junction Ag/AgCl (4 M KCl) reference electrode, and a Pt counter electrode. A double junction reference electrode was specifically used because the deposition was carried out in 1 M HNO_3, which can dissolve the AgCl in the reference electrode. The FTO working electrode was masked off to 0.5 cm^2 using insulating tape (3M, electroplating tape).[23] This masking helped to improve the uniformity of the film and reduce inhomogeneities associated with edge effects. A 1 M HNO_3 solution containing 100 mM tartaric acid, 20 mM $Bi(NO_3)_3 \cdot 5H_2O$, and 11 mM $K_2Sb_2(C_4H_2O_6)_2 \cdot H_2O$ was used as the plating solution. The precursor films were then deposited by passing 0.6 C per cm^2 at a potential of -0.7 V vs Ag/AgCl. Up to twelve BiSb films, each with a geometric surface area of 0.5 cm^2, were able to be deposited from a single 40 mL plating solution.

4.2.3 Synthesis of quaternary metal oxides

To synthesize the quaternary metal oxides, a 35 µL aliquot of a solution containing a metal salt was drop-casted onto a BiSb precursor film and then annealed at 650 °C for 3 h with a ramp rate of 2.1 °C per minute. Depending on the target quaternary species, a different metal salt was used. **Table 1** shows the composition of each drop-casting solution used to target a specific quaternary metal oxide. Because excess of the drop-casting element was used to ensure full conversion of the precursor film, the surplus of the drop-casted element that didn't react with the

BiSb precursor film formed a layer of binary metal oxide on the surface. **Table 2** shows the solution conditions used to remove the excess binary metal oxide that formed during the annealing process. All solutions were gently stirred at ~100 rpm with a magnetic stirbar during the soaking process. In an effort to enhance the PEC properties of the $Cu_2Bi_3Sb_3O_{14}$ electrodes, hybrid microwave annealing was performed in a conventional microwave oven using 600 watts of power with a graphite susceptor.

Table 1. The target quaternary phase and corresponding solvent and metal salt composition of each solution drop-casted onto the BiSb electrodes to achieve the desired phase.

Target quaternary phase	**Drop-casting solvent**	**Metal salt concentration**
$MoBi_{1.1}Sb_{0.9}MoO_6$	N,N-dimethylformamide	50 mM $(NH_4)_2MoS_4$
Bi_2SbVO_6	dimethyl sulfoxide	50 mM $VO(C_5H_7O_2)_2$
$Mn_2Bi_3Sb_3O_{14}$	N,N-dimethylformamide	50 mM $MnCl_2 \cdot 4H_2O$
$WBiSbO_6$	N,N-dimethylformamide	50 mM $(NH_4)_2WS_4$
$Zn_2Bi_3Sb_3O_{14}$	N,N-dimethylformamide	50 mM $ZnCl_2$
$FeBiSbO_7$	N,N-dimethylformamide	50 mM $FeCl_2 \cdot 4H_2O$
$Cu_2Bi_3Sb_3O_{14}$	N,N-dimethylformamide	50 mM $Cu(NO_3)_2 \cdot 3H_2O$

Table 2. The soaking solutions used to dissolve the excess binary metal oxides formed during the annealing process to form the quaternary metal oxide phases.

Target quaternary phase	**Binary oxide identity**	**Soaking solution**	**Time/temperature**
$MoBi_{1.1}Sb_{0.9}MoO_6$	MoO_3(?)	NA	NA
Bi_2SbVO_6	V_2O_5	NA	NA
$Mn_2Bi_3Sb_3O_{14}$	Mn_2O_3/Mn_3O_4	1-12 HCl or H_2SO_4	0.5h to >24 h

$WBiSbO_6$	WO_3	0.1-1 M NaOH	1 h, 50 °C
$Zn_2Bi_3Sb_3O_{14}$	ZnO	0.05 M H_2SO_4	1 h, RT
$FeBiSbO_7$	Fe_2O_3	0.1 M Oxalic acid	1 h, 60 °C
$Cu_2Bi_3Sb_3O_{14}$	CuO	0.1 M H_2SO_4	30 min, RT

4.2.4 Characterization

The crystalline nature of the materials at each step of the synthesis procedure was investigated using powder X-ray diffraction (PXRD, D8 Discover, Bruker, Ni-filtered Cu Kα radiation, $\lambda = 1.5418$ Å). The elemental composition and morphology were examined using energy dispersive X-ray spectroscopy (EDS; Noran System Seven, Thermo-Fisher, ultra-dry silicon drift detector) and scanning electron microscopy (SEM; LEO Supra55 VP) using an accelerating voltage of 2 keV for SEM and 22 keV for EDS. The bulk elemental ratios were calculated using the Thermo Scientific NSS software package (Filter without Standards Quant Fit method and the Proza correction method).

4.2.5 Photoelectrochemical characterization

Photoelectrochemical measurements of the quaternary metal oxides were performed using an SP-200 potentiostat/EIS (BioLogic Science Instruments) in an undivided three-electrode setup with a quartz glass cell. The working electrode was masked to ~0.02 cm^2 with lacquer before being used. To simulate sunlight, light from a 300 W Xe arc lamp (Ushio America. Inc.) was first directed through a water filter (IR filter), neutral density filters and an AM 1.5G filter. After passing through these filters, the light was collected with a fused silica fiber optic cable (Newport Instruments) and focused with a collimating lens (Newport Instruments) for uniform illumination. All samples were illuminated through the back side of the FTO substrate. The incident light power density was

calibrated using a thermopile detector (International Light, SED 623/HNK 15) connected to a research radiometer (International Light, IL 1700). The incident light intensity was calibrated to match that of the solar spectrum using an NREL-certified Si reference cell (Photo Emission Tech. Inc.).

Photoelectrochemical measurements were performed in 0.1 M H_2SO_4 (pH 1), 0.1 M KH_2PO_4 buffer (pH 7), or 0.1 M NaOH (pH 13). Na_2SO_3 (0.1 M) was used as a hole scavenger. The performance of each electrode was examined by linear sweep voltammetry (LSV) in the positive or negative direction from the open circuit potential (OCP) at a sweep rate of 10 mV/s. A Pt counter electrode and Ag/AgCl reference electrode were used in all cases. Although all measurements were taken using a Ag/AgCl reference electrode, all results are shown using the reversible hydrogen electrode (RHE) for ease of comparison in different pH conditions. The following equations illustrate the conversion of potential vs Ag/AgCl to potential vs RHE.

$$E_{(vs\ RHE)} = E_{(vs\ Ag/AgCl)} + E_{(Ag/AgCl)}(\text{reference, 4 M KCl}) + 0.0591\ V \times pH(\text{at } 25\ ^\circ C)$$

$$E_{Ag/AgCl}(\text{reference, 4 M KCl}) = 0.1976\ V \text{ vs NHE at } 25\ ^\circ C$$

The same three electrode undivided cell setup and potentiostat was used to acquire capacitance measurements to generate Mott-Schottky plots. The measurements were taken in a 0.1 M KH_2PO_4 (pH~7) buffer solution using a ~0.10 cm^2 surface area. A sinusoidal modulation of 10 mV was applied at frequencies of 0.5 kHz, 1 kHz, 2.3 kHz, and 5 kHz.

4.3 Results and Discussion

4.3.1 Synthesis of BiSb precursor films

The BiSb precursor films were synthesized via an electrochemical co-deposition of Sb^0 and Bi^0 in a 1 M nitric acid aqueous plating solution containing tartaric acid, bismuth nitrate, and

potassium antimony tartrate. This highly acidic solution is used to dissolve the bismuth precursor as bismuth readily forms insoluble oxides under non-acidic conditions unless properly complexed.[15] The potassium antimony tartrate precursor is a readily water soluble species that is used within Chapters 2, 3, and 5 of this dissertation to obtain a plating solution containing antimony. However, it was found that under these highly acidic conditions, the solution turned cloudy and remained cloudy after addition of the antimony precursor. This likely arises from the oxidation of soluble Sb^{3+} to insoluble Sb^{5+} that occurs under oxidizing acidic conditions[24] such as those of concentrated nitric acid solutions. However, by adding in tartaric acid, the precipitated antimony species could dissolve, providing a clear solution with a well-known concentration of precursor species. Then, by applying a negative enough potential, both $Sb^{3+/5+}$ and Bi^{3+} ions in solution were reduced to their insoluble Sb^0 and Bi^0 states, precipitating out at the electrode surface. The as-deposited BiSb films were removed from the deposition solution immediately upon cessation of the applied potential and were carefully dipped into DI water to remove excess plating solution on the surface. The oxidizing power of nitrate and the acidic nature of the solution can cause damage to the as-deposited films by oxidizing and re-dissolving the Sb and Bi metals unless the films are quickly removed.

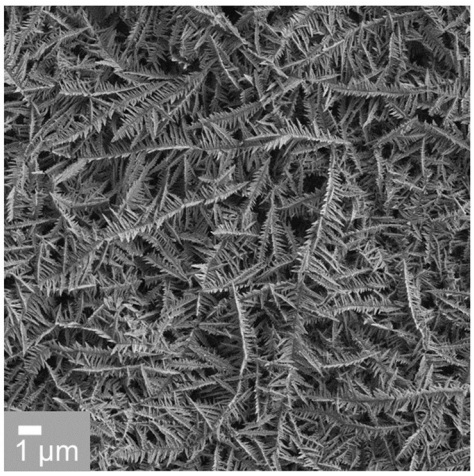

Figure 1. SEM image of as-deposited BiSb on FTO.

The as-deposited films were examined by SEM (**Figure 1**) and show a high surface area and porous dendritic "fern-like" morphology. Using EDS, the target 1:1 elemental ratio of the as-deposited BiSb was confirmed. Antimony and bismuth metals both adopt a rhombohedral crystal lattice with only slight differences in their lattice constants; therefore, Sb and Bi have been shown to be able to form a solid solution ranging from 100% Sb to 0% Sb.[25] Because of this, a 1:1 mixture of Bi and Sb should contain a set of x-ray diffraction (XRD) peaks that lie directly between the peaks that correspond to Bi metal and Sb metal. **Figure 2** shows the obtained XRD pattern for the as deposited BiSb films. The peak positions match a BiSb solid solution alloy with a 1:1 BiSb ratio, further confirming the 1:1 ratio of the as-deposited films.

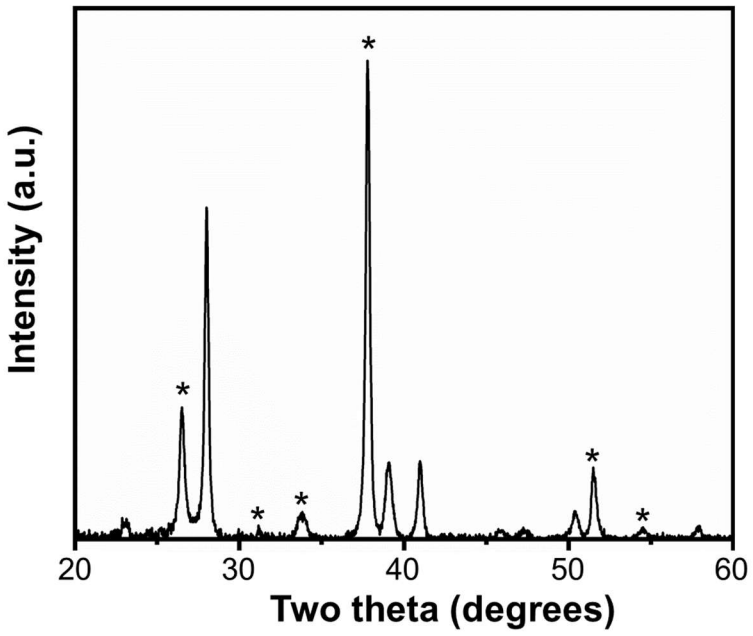

Figure 2. XRD pattern of the as-deposited BiSb electrode on FTO. The peaks corresponding to the FTO substrate are denoted by an asterisk.

4.3.2 Conversion of the precursor BiSb into quaternary metal oxides

The synthesis of the quaternary metal oxides followed the general scheme of drop-casting a metal salt dissolved in a non-aqueous solvent onto the BiSb precursor film and annealing at 650

°C in air for 3 h, followed by soaking in a solution to selectively remove the excess binary metal oxide that formed on the surface. Using a film containing well-mixed Bi^0 and Sb^0 is advantageous in that two of the three desired metals are already in close contact with one another and do not need to diffuse large distances to form the target compound. Using Bi and Sb in their non-oxidized, metallic states also simplifies the synthesis by increasing their reactivity with the third metal element, as their Bi and Sb oxides are very stable and would require higher temperatures and longer annealing time to allow for metal ion diffusion to form a new species.

The removal of impurity binary metal oxides that formed on the surface was necessary as excess of the drop-casted metal was used to ensure full conversion of the BiSb precursor film. This general procedure was applied to attempt to synthesize all seven of the target compounds: $MoBi_{1.1}Sb_{0.9}MoO_6$, Bi_2SbVO_6, $Mn_2Bi_3Sb_3O_{14}$, $WBiSbO_6$, $Zn_2Bi_3Sb_3O_{14}$, $Cu_2Bi_3Sb_3O_{14}$, and Fe_2BiSbO_7. To confirm that each of the target quaternary phases were successfully synthesized, XRD was performed on each film before the excess binary metal oxide was removed as this removal process could damage or destroy the underlying quaternary film.

Figure 3 contains XRD patterns of each of the systems post-annealing with the observed diffraction peaks indexed to the species present. Neither $MoBi_{1.1}Sb_{0.9}MoO_6$ nor Bi_2SbVO_6 formed even as minor impurity phases and only $BiSbO_4$ and Sb_2O_3 or $BiVO_4$, V_2O_5, and Sb_2VO_5 appeared in their XRD patterns respectively. $Mn_2Bi_3Sb_3O_{14}$, $WBiSbO_6$, $Zn_2Bi_3Sb_3O_{14}$, Fe_2BiSbO_7, and $Cu_2Bi_3Sb_3O_{14}$ were successfully synthesized and demonstrated the crystalline quaternary phase in their XRD patterns. I therefore investigated the removal of the excess binary metal oxides present on top of the quaternary metal oxides using Pourbaix diagrams and the CRC Handbook of Chemistry and Physics as guides for the stability and solubility of the binary oxide species.[15,26]

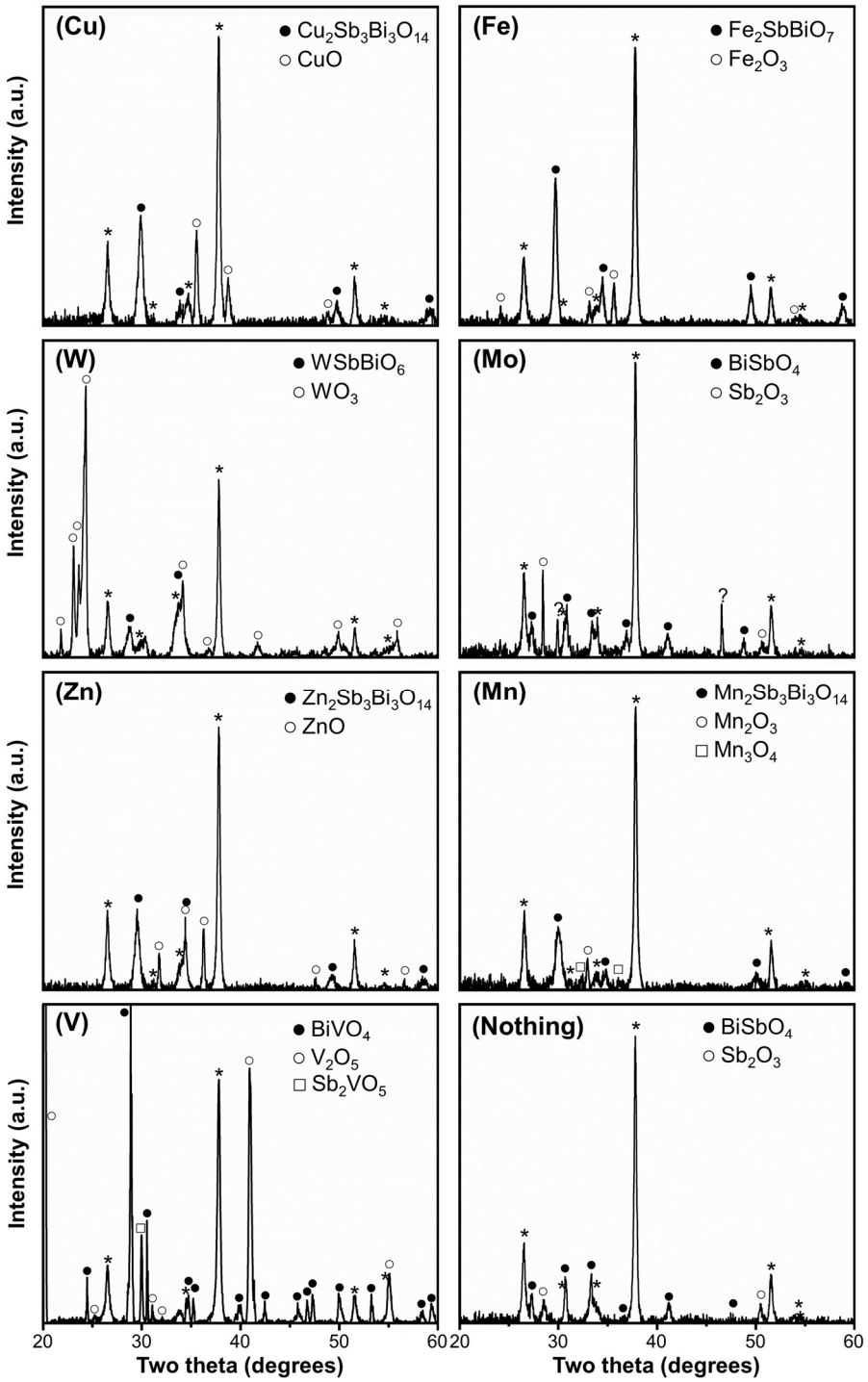

Figure 3. XRD patterns of the BiSb electrodes after drop-casting a metal salt solution on top and annealing. The metal contained in each solution is displayed in the upper left of each pattern. The peaks corresponding to the FTO substrate are denoted by an asterisk in each pattern.

The XRD pattern of $Mn_2Bi_3Sb_3O_{14}$ showed the presence of Mn_2O_3 and Mn_3O_4, both of which are known to be soluble under acidic conditions. Therefore, I tried using varying concentrations (1-12 M) of sulfuric or hydrochloric acid to remove the excess manganese oxides, but I was unable to find a condition where the quaternary phase would remain stable and the binary oxides would dissolve. While it may be possible to develop a condition to selectively remove the Mn_xO_y binaries from the $Mn_2Bi_3Sb_3O_{14}$ film, I decided to not pursue this process further. This decision was guided by the white color of the $Mn_2Bi_3Sb_3O_{14}$ underneath the Mn_xO_y binaries. **Figure 4** provides a picture of the different quaternary films after annealing and before soaking. The $Mn_2Bi_3Sb_3O_{14}$ that appeared underneath the brown binary oxides appeared white, indicating that it reflects all visible light and does not absorb within the visible spectrum, meaning it is not suitable as a visible-light-absorbing photoelectrode. I therefore discontinued trying to remove the binaries from atop the quaternary $Mn_2Bi_3Sb_3O_{14}$.

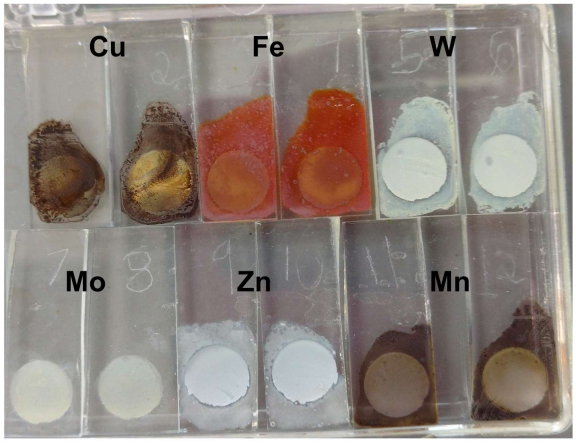

Figure 4. Photograph of annealed BiSb films in pairs after drop-casting a metal salt solution on top and annealing. In the top row from left to right the BiSb films had Cu, Fe, and W drop-casted on them. In the bottom row from left to right the BiSb films had Mo, Zn, and Mn drop-casted on them.

Examining the XRD pattern of $WBiSbO_6$, the excess W from the drop-casting solution crystallized into WO_3 during the annealing process. WO_3 dissolves under basic conditions, so different concentrations of sodium hydroxide solutions (0.1-1 M) were used to remove the excess

WO_3. However, a condition was unable to be determined in which the excess binary oxide was removed but the underlying quaternary species was retained. Similar to the $Mn_2Bi_3Sb_3O_{14}$ species, the $WBiSbO_6$ underneath the excess WO_3 appeared white in color (**Figure 4**), indicating it does not absorb in the visible spectrum, limiting its ability as a photoelectrode. Therefore, it was not investigated further.

On top of the Fe_2BiSbO_7 material was the characteristic brown-red color of rust (**Figure 4**) which was confirmed via the XRD pattern to be crystalline Fe_2O_3. Based upon the Pourbaix diagram for Fe, acidic solutions should be suitable to dissolve the excess iron oxide on top of the quaternary species. However, concentrations ranging from 0.1 to 1 M of HCl or H_2SO_4 were unable to selectively remove the overlaying iron oxide layer without damaging the underlying quaternary phase by also dissolving Fe out of the Fe_2BiSbO_7 phase. Rust is so ubiquitous within modern society because of the heavy usage iron containing materials, there actually exists, within general stores, solutions that are used to remove rust from iron containing objects. These solutions can have a variety of active ingredients including oxalic acid. It is well established in the literature that oxalic acid is an effective complexing agent that is able to selectively remove iron oxide from iron containing materials such as clays.[27] Therefore, solutions of oxalic acid between 0.01 and 0.1 M heated to ~60 °C were investigated as a method to remove the excess iron oxide on top of the quaternary phase. These solutions did succeed in removing the excess iron oxide on the surface, however, they still stripped away some of the Fe present within the quaternary phase, leaving behind an Fe deficient material. Based upon the color (yellow) of the material underneath the excess Fe_2O_3 it does appear that the Fe_2BiSbO_7 phase absorbs some visible light, making it suitable to continue to investigate as a photoelectrode. However, a yellow colored material is expected to have a bandgap of ~2.5 eV. This is a relatively large bandgap and thus, in the interest of time,

further investigation into the removal of the excess iron oxide was not performed in favor of examining the other quaternary phases. However, this material may be returned to at a later time if a suitable condition can be identified to remove the excess iron oxide.

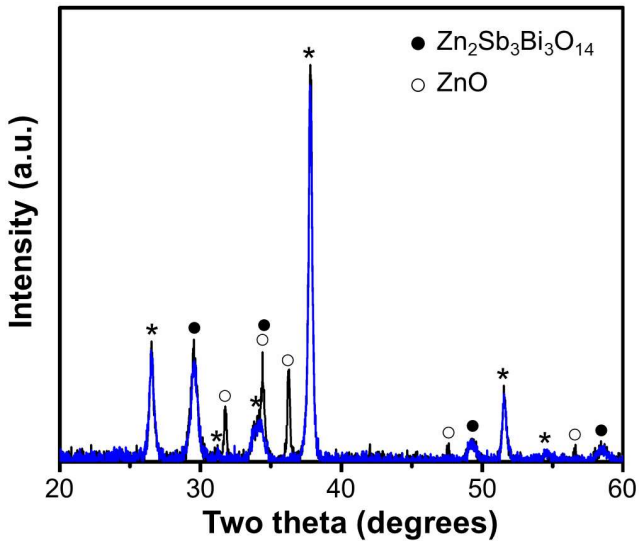

Figure 5. XRD patterns of annealed $Zn_2Bi_3Sb_3O_{14}$ (black) and the soaked $Zn_2Bi_3Sb_3O_{14}$ (blue) film, showing the loss of the binary ZnO phase after soaking. The peaks corresponding to the FTO substrate are denoted by an asterisk.

I was successful in removal of the excess ZnO from the as-synthesized $Zn_2Bi_3Sb_3O_{14}$ electrode. ZnO is soluble under a variety of different conditions, notably acidic, so to remove the excess ZnO, the electrodes were soaked in 0.05 M sulfuric acid for 1 h with 100 rpm stirring. The XRD pattern of the soaked $Zn_2Bi_3Sb_3O_{14}$ electrode is shown in **Figure 5**, demonstrating the phase-pure nature of the material. The absorbance spectrum of $Zn_2Bi_3Sb_3O_{14}$ was recorded using UV-vis spectroscopy and is shown in **Figure 6**. The absorbance edge at ~450 nm indicates the material does not absorb within the visible spectrum, which matches well with the observed white color of the pristine electrode. So, while I was able to successfully synthesize a phase-pure electrode of $Zn_2Bi_3Sb_3O_{14}$, the large bandgap severely limits its ability as a photoelectrode. I therefore focused my attention on the remaining material, $Cu_2Bi_3Sb_3O_{14}$.

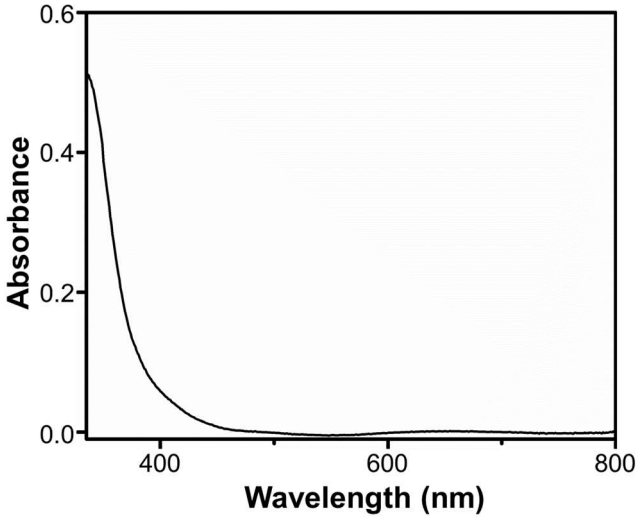

Figure 6. UV-Vis absorbance spectrum of $Zn_2Bi_3Sb_3O_{14}$ after soaking.

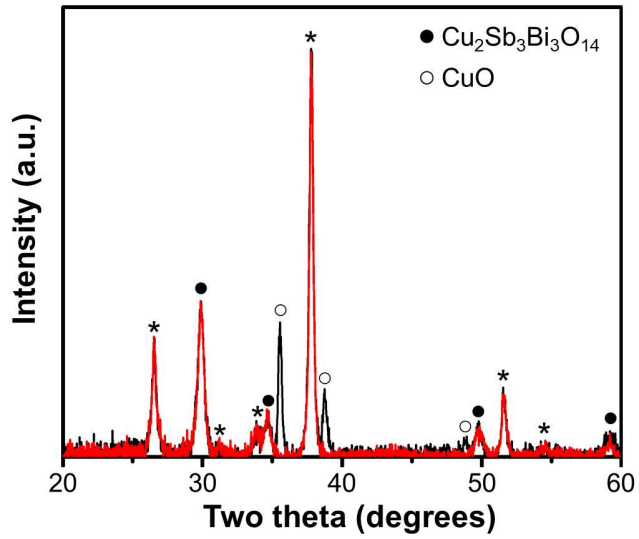

Figure 7. XRD patterns of annealed $Cu_2Bi_3Sb_3O_{14}$ (black) and the soaked $Cu_2Bi_3Sb_3O_{14}$ (red) film, showing the loss of the binary CuO phase after soaking. The peaks corresponding to the FTO substrate are denoted by an asterisk.

Excess CuO was removed from the $Cu_2Bi_3Sb_3O_{14}$ electrodes by soaking the films in 0.1 M sulfuric acid for 30 min with 100 rpm stirring, leaving an orange-yellow film behind. **Figure 7** shows the XRD pattern before and after soaking, demonstrating the selective removal of the CuO binary phase and the retention of the $Cu_2Bi_3Sb_3O_{14}$ phase. The selective removal of CuO was further confirmed through SEM images of the electrode (**Figure 8**). Before the soak it is covered

in a thick layer of CuO (**Figure 8a**) and after the soak the underlying dendritic morphology of the $Cu_2Bi_3Sb_3O_{14}$ is observed (**Figure 8b**).

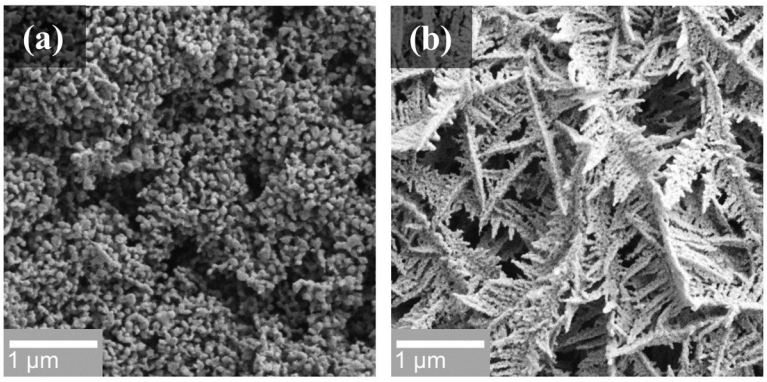

Figure 8. SEM images of the annealed (a) $Cu_2Bi_3Sb_3O_{14}$ and the soaked (b) $Cu_2Bi_3Sb_3O_{14}$ electrode, showing the loss of the binary CuO phase on the surface of the electrode after soaking.

4.3.3 Characterization of $Cu_2Bi_3Sb_3O_{14}$

With the successful removal of the binary oxide on the surface and retention of the pure $Cu_2Bi_3Sb_3O_{14}$ phase, I first used UV-Vis spectroscopy to measure the absorbance of the $Cu_2Bi_3Sb_3O_{14}$. Absorbance measurements provide a way to measure the bandgap of a material, which in turn can shed light on how suitable it is for use as a photoelectrode. If the bandgap is too large to absorb visible light, then it is likely not worth further investigating as a photoelectrode. The $Cu_2Bi_3Sb_3O_{14}$ electrodes showed an absorption edge at ~600 nm, and the band gap was determined to be ~2.1 eV via a Tauc plot for a direct band gap, which is well within the range of absorption for visible light indicating it has a band gap suitable for use as a visible light absorbing photoelectrode.

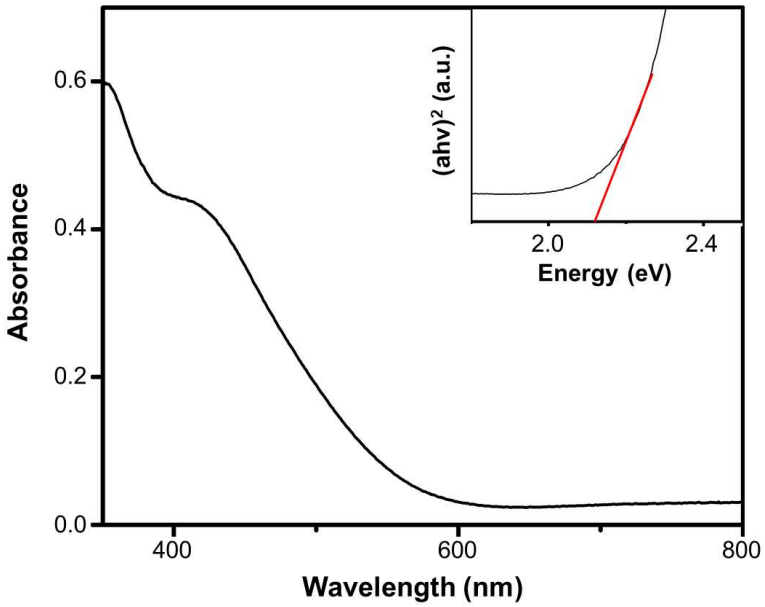

Figure 9. UV-Vis absorbance spectrum of $Cu_2Bi_3Sb_3O_{14}$ after soaking. The inset shows a Tauc plot calculated for a material with a direct band gap.

Before measuring the photoelectrochemical performance of $Cu_2Bi_3Sb_3O_{14}$ the chemical stability of the material was examined in three different pH conditions: acidic (0.1 M sulfuric acid, pH 1), neutral (0.1 M KH_2PO_4, pH 7), and alkaline (0.1 M NaOH, pH 13) to determine whether or not the predicted combination of Sb and Bi will stabilize the material in both acidic and basic conditions respectively. Electrodes were placed in one of the above conditions and then examined for changes in morphology and crystallinity after 24 hours. **Figure 10** shows the SEM images before and after the chemical stability test, where only minor changes in the shape of the dendrites for each film were observed but overall the porous, dendritic morphology was retained after the test. No changes in crystallinity were observed in the films after the chemical stability test for each pH condition (**Figure 11**). Based upon the above observations, $Cu_2Bi_3Sb_3O_{14}$ appears to be stable under a wide range of pH conditions (1-13), giving great flexibility in choice of electrolyte for use as a photoelectrode.

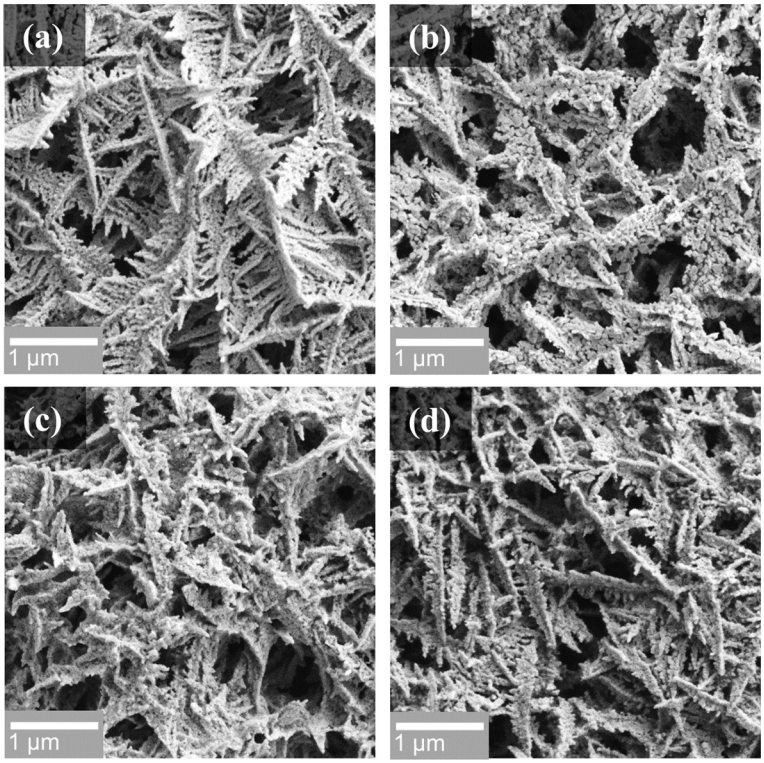

Figure 10. Top down SEM images of the pristine (a) $Cu_2Bi_3Sb_3O_{14}$ and the soaked $Cu_2Bi_3Sb_3O_{14}$ electrodes after the chemical stability test in (b) 0.1 M H_2SO_4, pH 1, (c) 0.1 M KH_2PO_4, pH 7, and (d) 0.1 M NaOH, pH 13.

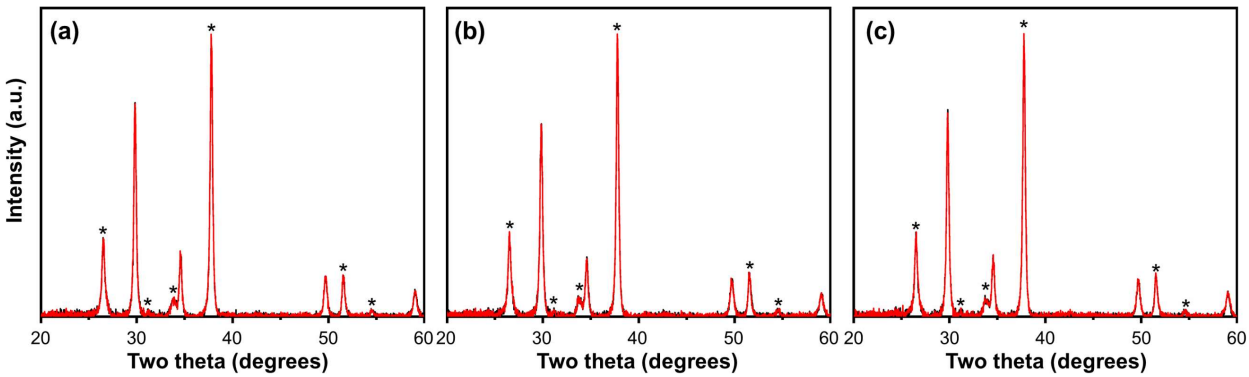

Figure 11. XRD patterns of $Cu_2Bi_3Sb_3O_{14}$ before (black) and after (red) the chemical stability test in (b) 0.1 M H_2SO_4, pH 1, (c) 0.1 M KH_2PO_4, pH 7, and (d) 0.1 M NaOH, pH 13. The peaks corresponding to the FTO substrate are denoted by an asterisk in each pattern.

The optimized conditions for photoelectrochemical (PEC) measurements on $Cu_2Bi_3Sb_3O_{14}$ have not been investigated in any previous literature. Therefore, chopped light linear sweep voltammetry (LSV) using 1 sun illumination (AM 1.5G, 100 mW/cm^2) was performed in acidic (0.1 M sulfuric acid, pH 1), neutral (0.1 M KH_2PO_4, pH 7), and alkaline (0.1 M NaOH, pH 13) media to determine which condition was most favorable for the photo response of $Cu_2Bi_3Sb_3O_{14}$. Back illumination was used for all samples measured. Because it has also not been reported whether $Cu_2Bi_3Sb_3O_{14}$ is n-type or p-type, I obtained linear sweep voltammograms (LSVs) swept in both the positive and negative directions from the open circuit potential of the electrodes. However, upon sweeping in the negative direction, the onset of negative dark current was observed under all pH conditions, likely arising from an electrochemical process occurring at the surface of the electrode. An example of this behavior in 0.1 M H_2SO_4 is shown in **Figure 12**. If the sweep was continued in the negative direction, significant dark current was observed, and the exposed electrode turned black. This black color likely arises from the reduction of Bi or Sb within the electrode, as Cu metal is red-orange in color. This reduction of Sb^{5+} and Bi^{3+} ions in the oxide lattice to Bi^0 or Sb^0 likely destroys the quaternary phase in the process. Because of this destructive behavior, the electrodes were not further examined for p-type behavior.

Figure 13 shows LSVs of $Cu_2Bi_3Sb_3O_{14}$ swept in the positive direction in each pH condition where a positive, n-type photocurrent was observed. The 0.1 M phosphate, pH 7 solution showed the highest photocurrent and had the most negative onset potential at ~0.55 V vs RHE. A more negative onset is preferred for photoanodes as it corresponds to a larger photovoltage (i.e. the difference between the photocurrent onset and the thermodynamic potential of water oxidation),[23] which can be thought of as the additional voltage gained when using a semiconductor to absorb light instead of having to apply a bias in conventional electrocatalysis.

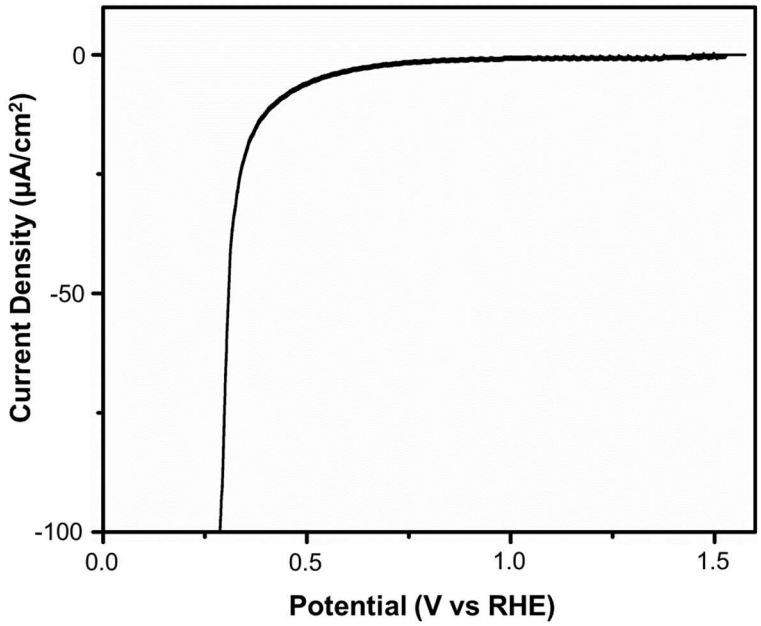

Figure 12. LSV of $Cu_2Bi_3Sb_3O_{14}$ in 0.1 M H_2SO_4 (pH 1.3) swept towards the negative direction under 1 sun illumination (AM 1.5G, 100 mW/cm^2), illustrating the lack of p-type photocurrent for water reduction and the strong onset of dark current at potentials past 0.4 V vs RHE.

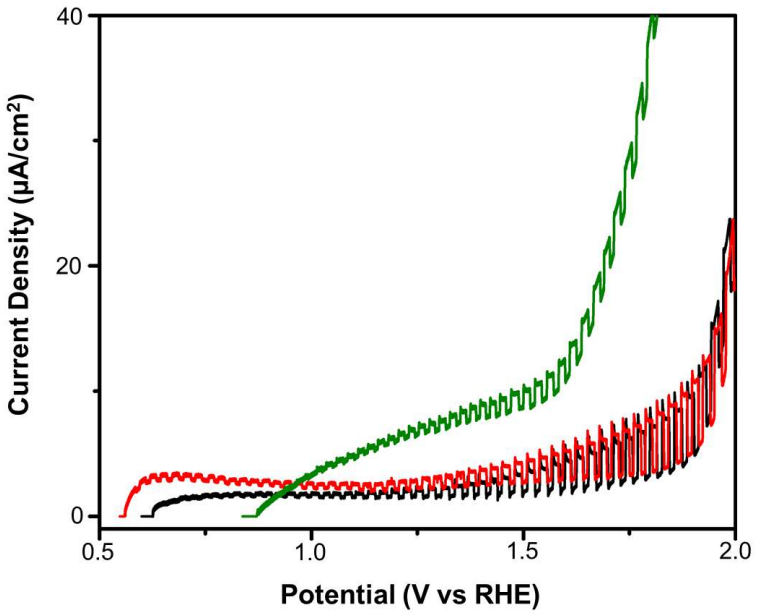

Figure 13. LSVs of $Cu_2Bi_3Sb_3O_{14}$ in 0.1 M H_2SO_4, pH 1.3 (black), 0.1 M KH_2PO_4, pH 7 (red), and 0.1 M NaOH, pH 13 (green) swept to the positive direction under 1 sun illumination (AM 1.5G, 100 mW/cm^2) demonstrating anodic photocurrent for the oxidation of water.

However, the total photocurrent in pH 7 was still very low (~2 uA/cm^2 at 1.23 V vs RHE), and the onset potential is relatively positive (~0.55 V vs RHE) when compared to state-of-the-art metal oxide photoanodes such as $BiVO_4$ which possesses an onset potential of ~0.2 V vs RHE and can have photocurrent that exceeds 5 mA/cm^2 at 1.23 V vs RHE.[28] To examine the possible causes of this poor performance, consider the three primary components that determine the photocurrent of a photoelectrode,[23] as outlined in the equation below:

$$J_{PEC} = J_{abs} \times \Phi_{sep} \times \Phi_{inj}$$

J_{PEC} is the measured photocurrent density. J_{abs} is the photon absorption rate expressed as a current density and can be calculated assuming all absorbed photons are used to generate photocurrent. This value is typically expressed as current density and is the maximum possible photocurrent a photoelectrode can obtain based on the percentage of light it can absorb from the solar spectrum at each wavelength. Φ_{sep} is the percentage of photo generated carriers that are able to reach the surface without recombining, and Φ_{inj} is the percentage of surface-reaching minority carriers that are able to be injected into the solution. The band gap and absorbance spectrum of these $Cu_2Bi_3Sb_3O_{14}$ electrodes were used to calculate a J_{abs} of ~4.5 mA/cm^2. However, less than 0.5% of that was observed, which means that the other two factors of charge separation and/or charge injection into the solution are inhibiting $Cu_2Bi_3Sb_3O_{14}$ from oxidizing water. In addition to charge separation and charge injection, the amount of charge carriers, for a n-type material the majority carriers are electrons and the minority carriers are holes, within the material itself may be a limiting factor. If there are too few charge carriers then the conductivity of the material will correspondingly be low and thus the performance of $Cu_2Bi_3Sb_3O_{14}$ will suffer.

To help separate the effect of each process, sulfite, a facile 1-electron transfer hole scavenger for an n-type electrode, that provides a kinetically fast oxidation reaction at the surface of the electrode can be used.[29] By doing so, Φ_{inj} can be effectively set to ~1,[23] allowing the separation of the effects of charge separation and carrier density from that of charge injection, providing clues to whether it is charge injection inhibiting the performance of $Cu_2Bi_3Sb_3O_{14}$. It is also expected that the photocurrent onset will shift in the negative direction for sulfite when compared to water oxidation as less driving force is required for the 1 e^- oxidation of sulfite over the 4 e^- oxidation of water. This means that the conduction and valence bands do not need to be as bent to drive the oxidation of sulfite. This can provide information about the possible flatband location of $Cu_2Bi_3Sb_3O_{14}$ which, with the calculated band gap from absorbance measurements (**Figure 9**), may also provide clues as to the rough location of the conduction and valence band.[23] This information can tell us if $Cu_2Bi_3Sb_3O_{14}$ has band positions suitable for full unassisted water splitting or what kind of photocathode pairing is necessary in a tandem device using $Cu_2Bi_3Sb_3O_{14}$ as the photoanode.[23]

The chopped light LSV of $Cu_2Bi_3Sb_3O_{14}$ in a 0.1 M phosphate, pH 7 solution containing 0.1 M sulfite is shown in **Figure 14**. The large dark current observed at ~1.2 V vs RHE is attributed to the electrochemical oxidation of sulfite. However, before this electrochemical process occurred, there was no enhancement of the anodic photocurrent or negative shift in the photocurrent onset, indicating charge injection into the solution may not be the primary limiting factor for this material. This suggests that $Cu_2Bi_3Sb_3O_{14}$ may suffer significantly in separating the charges generated by photon absorption or has low conductivity on account of its potentially low charge carrier density. These are commonly observed challenges with metal oxide semiconductor electrodes.[32,33]

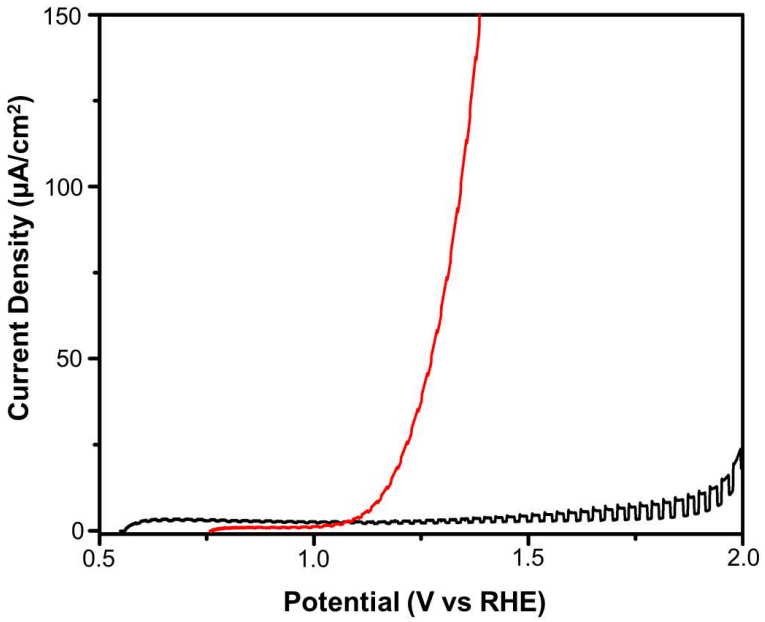

Figure 14. LSVs of $Cu_2Bi_3Sb_3O_{14}$ in 0.1 M KH_2PO_4, pH 7 without sulfite (black) and with sulfite (red) swept towards the positive direction. The steep increase in current when in the presence of sulfite (red) is attributed to the electrochemical reduction of sulfite.

Because no negative shift in photocurrent onset was observed using sulfite and water is a kinetically complex process which will inadvertently shift the photocurrent onset to a value more positive than the flatband potential, it is not possible to determine an estimate of the flatband position using the LSVs in **Figure 14**. In an attempt to elucidate the position of the flatband potential, Mott-Schottky measurements at different frequencies were performed on $Cu_2Bi_3Sb_3O_{14}$ electrodes in 0.1 M KH_2PO_4, pH 7 (**Figure 15**). The linear region of each is then used to extrapolate to the x-intercept, which is then assumed to be the flatband potential if they all converge at the same value.[30,31] (See reference 31 for the full derivation and explanation and reference 30 for an overview.) However, for $Cu_2Bi_3Sb_3O_{14}$ each frequency was observed to have its own different x-intercept. This is not unexpected as the surface of $Cu_2Bi_3Sb_3O_{14}$ is not considered ideal in order to determine a reliable flatband potential.[30,31] Numerous potential factors may be influencing this frequency dependence,[30,31] but for $Cu_2Bi_3Sb_3O_{14}$ the likely factors include the non-flat, porous morphology, surface states creating different capacitive environments at the surface than the bulk

material, and multiple possible donor states creating capacitive environments that are not uniform, making it not possible to derive meaningful data about the position of the flatband potential from the Mott-Schottky data. Therefore, based upon the location of the start of the water oxidation photocurrent in 0.1 KH_2PO_4, pH 7 (**Figure 14**) the only possible claim that I can make is that the flatband potential is at least more negative than ~0.55 V vs RHE.

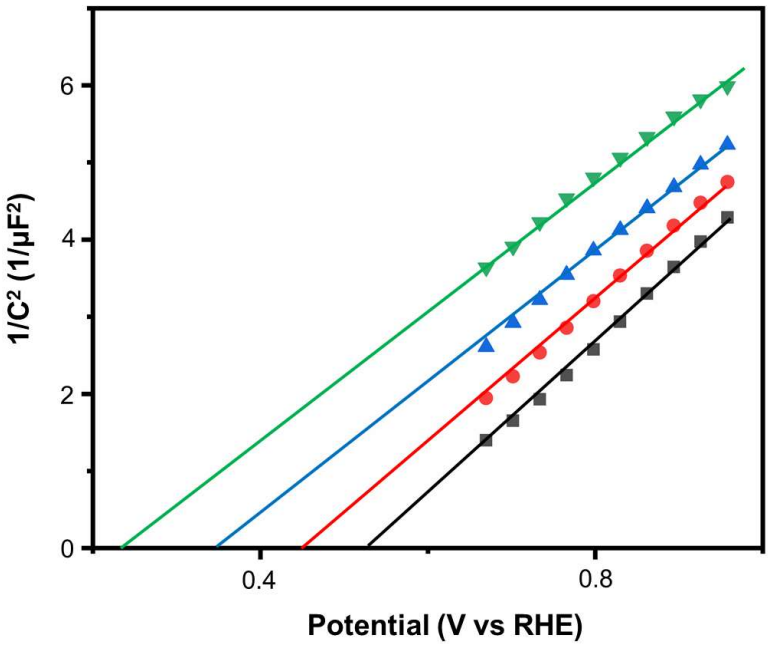

Figure 15. Mott-Schottky measurements of $Cu_2Bi_3Sb_3O_{14}$ in 0.1 M KH2PO4 (pH 7) in the dark measured at 5 kHz (green triangle), 2.3 kHz (blue triangle), 1 kHz (red circle), and 0.5 kHz (black square) frequencies.

4.3.4 Hybrid microwave annealing treatment of $Cu_2Bi_3Sb_3O_{14}$

In an effort to improve the charge carrier separation efficiency and reduce the recombination rate of holes and electrons, I investigated using a hybrid microwave annealing (HMA) treatment on $Cu_2Bi_3Sb_3O_{14}$ electrodes. HMA has been shown to enhance the photocurrent of metal oxide materials by improving the bulk charge carrier separation and charge carrier injection into solution by increasing the crystallinity and passivation of defect sites by heating the material to very high temperatures for short periods of time.[34] This method uses a simple

microwave oven and a susceptor, such as silicon or carbon. The microwaves are absorbed by both the sample and the susceptor. The sample then heats up both internally from the absorbed microwaves and externally from the heat radiated by the susceptor. The term "hybrid" arises from this combination of internal and external heating.[35] Using a graphite powder susceptor, HMA was performed on $Cu_2Bi_3Sb_3O_{14}$ electrodes.

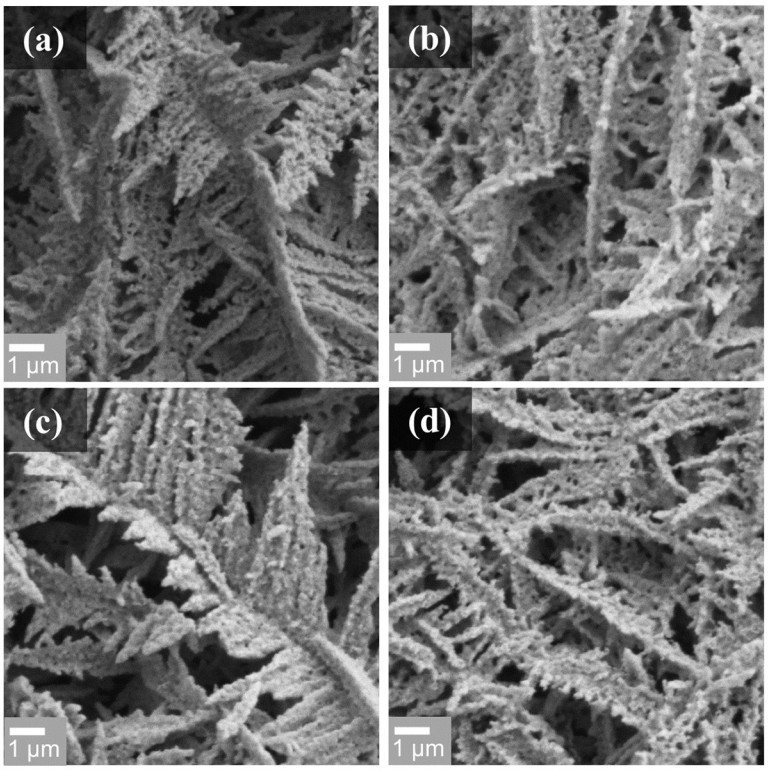

Figure 16. Top down SEM images of the $Cu_2Bi_3Sb_3O_{14}$ electrodes (a) before and after the HMA treatment for (b) 1 minute, (c) 2 minutes, and (d) 4 minutes.

The morphology and crystallinity were unchanged after 1, 2, and 4 min of HMA as shown in **Figure 16** and **Figure 17** respectively. This is not surprising as the material is already crystalline and the temperature does not remain high for long enough to cause large changes in bulk morphology. However, passivation of defects and local changes to structure may have still occurred. I examined the photocurrent response of the HMA-treated $Cu_2Bi_3Sb_3O_{14}$ electrodes in

0.1 M phosphate (pH 7) for water oxidation as shown in **Figure 18**. No increase in photocurrent was observed after HMA, and the photocurrent onset shifted to a more positive value, an undesirable effect for a photoanode. This lack of photocurrent suggests that HMA either did not reduce the number of bulk or surface defects that may be contributing to charge carrier recombination or that another factor is at play, such as an inherent limitation to the material like charge diffusion length, similar to the binary Fe_2O_3 or too few charge carriers which lead to low conductivity and thus low photocurrent.[36-38]

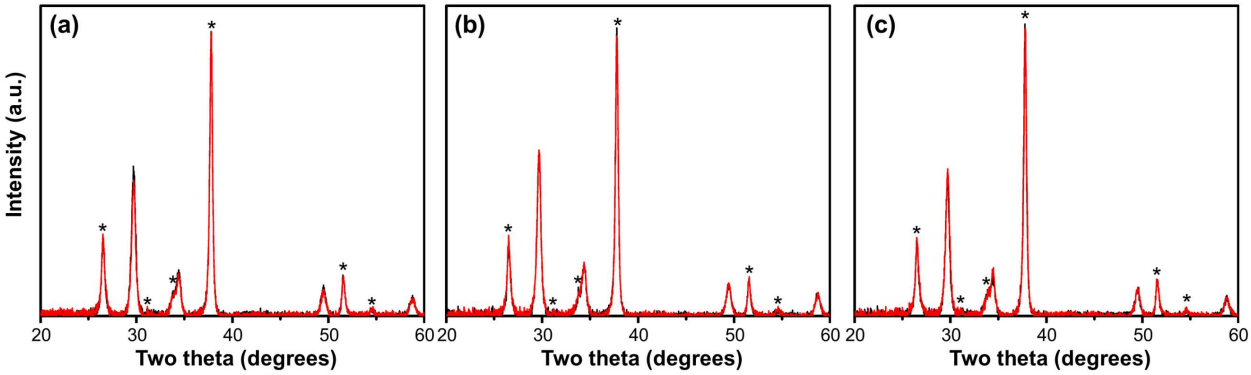

Figure 17. XRD patterns of $Cu_2Bi_3Sb_3O_{14}$ before (black) and after (red) the HMA treatment for (a) 1 min, (b) 2 min, and (c) 4 min. The peaks corresponding to the FTO substrate are denoted by an asterisk in each pattern.

While $Cu_2Bi_3Sb_3O_{14}$ shows promise in terms of its relatively small bandgap of 2.1 eV, significant challenges must be overcome before it can be used as a photoelectrode. I have outlined possible solutions to these challenges within Section 4.4 of this chapter.

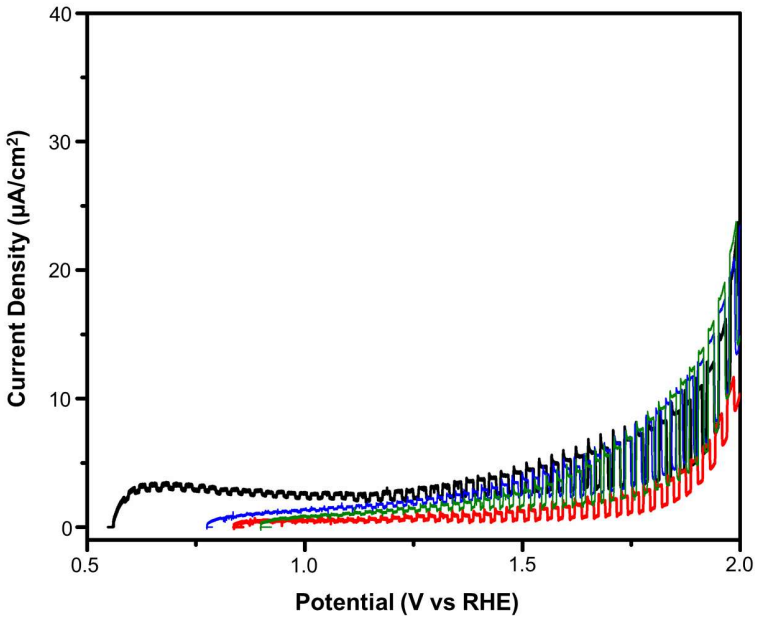

Figure 18. LSVs of $Cu_2Bi_3Sb_3O_{14}$ in 0.1 M KH_2PO_4 (pH 7) swept towards the positive direction treated either without (black) HMA treatment, for (red) 1 minute, (blue) 2 minute, or (green) 4 minute HMA treatment.

4.4 Conclusions

Five target quaternary metal oxides were successfully synthesized by drop-casting a metal species on top of a precursor BiSb film and annealing. The excess binary metal oxide(s) formed during annealing were successfully removed from two of these target materials, $Zn_2Bi_3Sb_3O_{14}$, and $Cu_2Bi_3Sb_3O_{14}$. The band gap of $Zn_2Bi_3Sb_3O_{14}$ was too large to absorb visible light, but $Cu_2Bi_3Sb_3O_{14}$ showed light absorption in the visible range and was investigated as a photoelectrode. It showed good chemical stability but low performance under all pH conditions for water oxidation and sulfite oxidation, leading to the conclusion that it possibly suffers from severe bulk recombination or low charge carrier density or both, limiting its ability as a photoelectrode.

I recommend the following for each material to improve upon their properties as well as their synthetic process. For the two compounds that were not successfully synthesized $MoBi_{1.1}Sb_{0.9}MoO_6$ and Bi_2SbVO_6 I recommend modifying the elemental ratios in the BiSb plating solution to better match the final target Bi:Sb ratios in the quaternary species by adjusting the concentrations of Bi or Sb precursors. Both $MoBi_{1.1}Sb_{0.9}MoO_6$ and Bi_2SbVO_6 have more Bi relative to Sb, and this should be accounted for in the precursor films. In the interest of time, the BiSb precursor films had not been modified to accommodate this as neither of the species appeared even as minor phases in the XRD patterns. This suggests that the annealing conditions for both $MoBi_{1.1}Sb_{0.9}MoO_6$ and Bi_2SbVO_6 will also need to be modified in terms of temperature and time spent annealing to create the target quaternary phase. The $Mn_2Bi_3Sb_3O_{14}$ and $WBiSbO_6$ phases both require additional experimentation to develop a procedure to remove the excess binary oxides on top of the electrode. Investigating the use of heat or complexing agents instead of acid or base may prove useful. However, I caution further investigating either of these compounds as they appear white underneath the binary oxides, indicating their visible light absorption is likely very limited.

I recommend no further PEC work be completed on the $Zn_2Bi_3Sb_3O_{14}$ phase as it was white and showed no absorption in the visible range. For Fe_2BiSbO_7, the yellow color underneath the excess iron oxides indicates the material may absorb visible light, however, selective removal of the excess iron oxide is critical before more in-depth analysis can be performed. For this material, I recommend further investigating other complexing agents that can selectively remove the iron oxide species from the surface. Many possibly candidates exist within both general stores and in the literature, including muriatic acid, citric acid, acetic acid, sodium hydrosulfite, or potentially

more biological-based compounds that contain a heme group, which is the same complexing group that strongly binds Fe in the blood of animals.

For $Cu_2Bi_3Sb_3O_{14}$ I recommend first investigating an alternative hole scavenger such as H_2O_2 or the organic radical species TEMPOL to check whether or not the reason I observed no photocurrent enhancement when using sulfite was because of poor sulfite oxidation kinetics. If no enhancement in photocurrent is observed, then it is possible bulk recombination due to a very short charge diffusion length or the presence of many defect sites acting as charge recombination centers limits the performance of $Cu_2Bi_3Sb_3O_{14}$. A possible way to overcome a short diffusion length is by creating even smaller morphological features, which will allow for the charges to get to the surface of the material before recombining. Defect sites can potentially be decreased by adjusting the annealing conditions and the soaking conditions, as soaking could be damaging the material by creating extra surface defect sites in a way that does not affect its crystallinity. Another possible limitation is an inherently low carrier density within the material leading to low conductivity. A potential solution for this is the addition of dopants within the material to increase the p-type character. This can be done during the annealing portion of the synthesis method by addition of other metal salts into the drop-casting solution. For all of the materials, I highly recommend checking the elemental ratios after annealing and after soaking to ensure the stochiometric compound is present for each film. I observed that the elemental ratios would vary between films after annealing and soaking even when the crystallinity was observed to be the same.

Overall, I expect this work to help provide a new synthetic tool to synthesize stochiometric, phase-pure quaternary metal oxides as photoelectrodes for water splitting devices. While the materials investigated in this study did not outperform state-of-the-art metal oxides present in the literature, the ability to synthesize stochiometric, phase-pure materials in less than 24 h without

extensive heating and mechanical processing as is typical to synthesize quaternary materials by solid state methods provides a facile route to investigate a whole class of Bi-and Sb-containing quaternary metal oxides.

4.5 References

1. Lewis, N. S.; Nocera, D. G. Powering the planet: Chemical challenges in solar energy utilization. *Proc. Natl. Acad. Sci. U.S.A.* **2006**, *103*, 15729−15735.
2. Li, Z.; Luo, W.; Zhang, M.; Feng, J.; Zou, Z. Photoelectrochemical cells for solar hydrogen production: current state of promising photoelectrodes, methods to improve their properties, and outlook. *Energy Environ. Sci.* **2013**, *6*, 347−370.
3. Pinaud, B. A.; Benck, J. D.; Seitz, L. C.; Forman, A. J.; Chen, Z.; Deutsch, T. G.; James, B. D.; Baum, K. N.; Baum, G. N.; Ardo, S.; et al. Technical and economic feasibility of centralized facilities for solar hydrogen production via photocatalysis and photoelectrochemistry. *Energy Environ. Sci.* **2013**, *6*, 1983−2002.
4. Fujishima, A.; Honda, K. Electrochemical Photolysis of Water at a Semiconductor Electrode. *Nature* **1972**, *238*, 37−38.
5. Jang, Y. J.; Jang, J.-W.; Choi, S. H.; Kim, J. Y.; Kim, J. H.; Youn, D. H.; Kim, W. Y.; Han, S.; Sung Lee, J. Tree Branch-Shaped Cupric Oxide for Highly Effective Photoelectrochemical Water Reduction. *Nanoscale* **2015**, *7*, 7624−7631.
6. Paracchino, A.; Laporte, V.; Sivula, K.; Grätzel, M.; Thimsen, E. Highly Active Oxide Photocathode for Photoelectrochemical Water Reduction. *Nat. Mater.* **2011**, *10*, 456−461.
7. Chen, X.; Mao, S. S. Titanium Dioxide Nanomaterials: Synthesis, Properties, Modifications, and Applications. *Chem. Rev.* **2007**, *107*, 2891−2959.
8. Kang, D.; Kim, T. W.; Kubota, S. R.; Cardiel, A. C.; Cha, H. G.; Choi, K.-S., Electrochemical Synthesis of Photoelectrodes and Catalysts for Use in Solar Water Splitting. *Chem. Rev.* **2015**, *115*, 12839-12887.
9. He, H. C.; Liao, A. Z.; Guo, W. L.; Luo, W. J.; Zhou, Y.; Zou, Z. G., State-of-the-art progress in the use of ternary metal oxides as photoelectrode materials for water splitting and organic synthesis. *Nano Today* **2019**, *28*, 22.
10. Lee, D. K.; Lee, D.; Lumley, M. A.; Choi, K. S., Progress on ternary oxide-based photoanodes for use in photoelectrochemical cells for solar water splitting. *Chem. Soc. Rev.* **2019**, *48*, 2126-2157.

11. Lumley, M. A.; Radmilovic, A.; Jang, Y. J.; Lindberg, A. E.; Choi, K.-S., Perspectives on the Development of Oxide-Based Photocathodes for Solar Fuel Production. *J. Am. Chem. Soc.* **2019**, *141*, 18358-18369.

12. Liu, H.,; Nakamura, R.; Nakato, Y., Bismuth–Copper Vanadate $BiCu_2VO_6$ as a Novel Photocatalyst for Efficient Visible-Light-Driven Oxygen Evolution. *ChemPhysChem*, **2005**, *6*, 2499-2502.

13. Luan, J.; Cai, Hongling, C.; Zheng, S.; Hao, X.; Luan, G.; Wu, X.; Zou, Z., Structural and photocatalytical properties of novel Bi_2GaVO_7. *Mater. Chem. Phys.*, **2007**, *104*, 119-124.

14. Munawar, K.; Perveen, F.; Shahid, M. M.; Basirun, W. J.; Misran, M. B.; Mazhar, M., Synthesis, characterization and computational study of an ilmenite-structured $Ni_3Mn_3Ti_6O_{18}$ thin film photoanode for solar water splitting. *New J. Chem.*, **2019**, *43*, 11113-11124.

15. Pourbaix, M., *Atlas of Electrochemical Equilibria in Aqueous Solutions.* 2 ed.; National Association of Corrosion Engineers: Houston, Texas, 1974; p 524-532.

16. Bégué, P.; Enjalbert, R.; Castro, A., The Upper Limit of the Solid Solution $Bi_{2-x}Sb_xMoO_6$: Structure Refinement of $Bi_{1.1}Sb_{0.9}MoO_6$. *J. Solid State Chem.* **2001**, *159*, 72-79.

17. Castro, A.; Millan, P.; Enjalbert, R., Structural evolution of the Aurivillius framework in the solid solutions Bi_2WO_6-Sb_2WO_6. *Mater. Res. Bull.* **1995**, *30*, 871-882.

18. Sellami, M.; Caignaert, V.; Hamdad, M.; Bekka, A.; Bettahar, N., Synthesis and characterization of new pyrochlore solid solution $Bi_{1.5}Sb_{1.5}Cu_{1-x}Mn_xO_7$. *J. Alloy. Compd.* **2009**, *482*, 13-18.

19. Sellami, M.; Caignaert, V.; Hanni, F. Z. K.; Bettahar, N.; Benhadria, N.; Sari-Mohammed, E.; Imine, S.; Bahmani, A., Synthesis and characterization of new pyrochlore solid solution $Bi_{1.5}Sb_{1.5-x}Nb_xCuO_7$. *Cr. Chim.* **2014**, *17*, 899-904.

20. Luan, J.; Pan, B.; Paz, Y.; Li, Y.; Wu, X.; Zou, Z., Structural, photophysical and photocatalytic properties of new Bi_2SbVO_7 under visible light irradiation. *Phys. Chem. Chem. Phys.* **2009**, *11*, 6289-6298.

21. Miles, G. C.; West, A. R., Pyrochlore Phases in the System ZnO–Bi_2O_3–Sb_2O_5: I. Stoichiometries and Phase Equilibria. *J. Am. Ceram. Soc.* **2006**, *89*, 1042-1046.

22. Luan, J.; Hu, Z., Synthesis, Property characterization, and photocatalytic activity of novel visible light-responsive photocatalyst Fe_2BiSbO_7. *Int. J. Photoenergy* **2011**, *2012*, 1-11.

23. Govindaraju, G. V.; Wheeler, G. P.; Lee, D.; Choi, K.-S., Methods for Electrochemical Synthesis and Photoelectrochemical Characterization for Photoelectrodes. *Chem. Mater.* **2017**, *29*, 355-370.

24. Patnaik, P., *Handbook of Inorganic Chemicals*. McGraw-Hill, 2002, ISBN 0-07-049439-8

25. Ehret, W. F.; Abramson, M. B., The Nature of the Solid Phase in the System Antimony—Bismuth1. *J. Am. Chem. Soc.* **1934**, *56*, 385-388.

26. *CRC Handbook of Chemistry and Physics*, 94th ed.; Haynes, W. M.; Ed.; CRC Press: Boca Raton, FL, 2013; Sections 4.43−4.101.

27. Sultana, U. K.; Kurny, A. S. W. Dissolution kinetics of iron oxides in clay in oxalic acid solutions. *Int. J. Min. Met. Mater.* **2012**. *19*, 1083-1087.

28. Lee, D. K.; Choi, K.-S. Enhancing Long-Term Photostability of $BiVO_4$ Photoanodes for Solar Water Splitting by Tuning Electrolyte Composition. *Nat. Energy* **2018**, *3*, 53−60.

29. Sarala, R.; Islam, M. A.; Rabin, S. B.; Stanburg, D. M. Aromatic sulfonation by sulfite and the reduction potential of the sulfite radical: oxidation of sulfite by the tetraammine(phenanthroline)ruthenium- (II) cation. *Inorg. Chem.* **1990**, *29*, 1133−1142.

30. Cardon. F.; Gomes, W. P. On the determination of the flat-band potential of a semiconductor in contact with a metal or an electrolyte from the Mott-Schottky plot. *J. Phys. D: Appl. Phys.* **1978**, *11*, L63.

31. Cardon. F.; Gomes, W. P. Electron Energy Levels in Semiconductor Electrochemistry. *Prog. Surf. Sci.* **1982**, *12*, 155-216.

32. Abdi, F. F. & Berglund, S. P. Recent developments in complex metal oxide photoelectrodes. *J. Phys. D Appl. Phys.* **2017**, *50*.

33. Rettie, A. J. E., Chemelewski, W. D., Emin, D. & Mullins, C. B. Unravelling small polaron transport in metal oxide photoelectrodes. *J. Phys. Chem. Lett.* **2016**, *7*, 471–479.

34. Kim, J. H.; Kim, J. H.; Jang, J.-W.; Kim, J. Y.; Choi, S. H.; Magesh, G.; Lee, J.; Lee, J. S., Awakening Solar Water-Splitting Activity of $ZnFe_2O_4$ Nanorods by Hybrid Microwave Annealing. *Adv. Energy. Mater.* **2015**, *5*, 1401933.

35. Oghbaei, M.; Mirzaee, O., Microwave versus conventional sintering: A review of fundamentals, advantages and applications. *J. Alloy. Compd.* **2010**, *494*, 175-189.

36. Katz, M. J.; Riha, S. C.; Jeong, N. C.; Martinson, A. B. F.; Farha, O. K.; Hupp, J. T. Toward Solar Fuels: Water Splitting with Sunlight and ″Rust”? *Coord. Chem. Rev.* **2012**, *256*, 2521−2529.

37. Dotan, H.; Sivula, K.; Grätzel, M.; Rothschild, A.; Warren, S. C. Probing the Photoelectrochemical Properties of Hematite (α-Fe_2O_3) Electrodes Using Hydrogen Peroxide as a Hole Scavenger. *Energy Environ. Sci.* **2011**, *4*, 958−964.

38. Hamann, T. W. Splitting Water with Rust: Hematite Photoelectrochemistry. *Dalton Trans.* **2012**, *41*, 7830−7834.

Chapter Five: Investigation of Bi, Sb and BiSb for the electrochemical nitrogen reduction reaction

5.1 Introduction

The synthesis of ammonia (NH_3) using nitrogen (N_2) and hydrogen (H_2) developed by Fritz Haber in 1909 and scaled up by Carl Bosch in 1910 to produce artificial fertilizers provided the groundwork for the explosive growth of human populations around the world in the last one hundred years.[1] While Haber's initial experimental setup could only produce 0.09 kg of NH_3 per hour (~0.8 tonnes of NH_3 per year),[2] today's optimized Haber-Bosch process produces 171 million tonnes of NH_3 per year around the globe with conversion efficiencies of 97%.[3] The process is so ubiquitous that approximately 50% of the nitrogen atoms in all humans today originated from synthetically produced NH_3 using the Haber-Bosch process.[4] However, this process is also environmentally taxing by consuming large amounts of fossil fuels to produce the necessary H_2 via steam reforming as well as to achieve the high temperatures (400-500 °C) and high pressures (150-250 bar) required for optimal efficiency.[5,6] This not only releases large amounts of CO_2 (~1.9 metric tons of CO_2 per metric ton of NH_3),[5,6] but also requires centralization and proximity to natural gas feedstocks, which increases transportation costs to those in remote areas that require ammonia-based fertilizers and restricts NH_3 production to large industrial complexes requiring high amounts of capital.

In contrast, the electrochemical nitrogen reduction reaction (ENRR) provides an environmentally benign pathway to produce NH_3 under ambient temperatures and pressures, using water as the hydrogen source. Coupled with reduced electricity costs because of renewable energy,[7] this process can also be decentralized and produced in variably-sized units to suit the needs of those in remote areas, leading to reduced transportation and investment costs. However, the commercialization of the ENRR process is currently impeded by the low faradaic efficiency (FE) achieved for the conversion of N_2 to NH_3. This low FE stems primarily from the standard

reduction potential of N_2 to NH_3 ($N_2(g) + 8H^+ + 6e^- \rightleftharpoons 2NH_4^+(aq)$, $E^0 = 0.275$ V vs. SHE) being close to the standard reduction potential of the hydrogen evolution reaction ($2H^+ + 2e^- \rightleftharpoons H_2(g)$, $E^0 = 0$ V vs. SHE).[8] This coupled with N_2 reduction to NH_3 being a much more kinetically complex process than the HER leads to the HER dominating under the applied potentials required for the ENRR, thus many metal catalysts demonstrate FE values for the ENRR below 1%.

There have been some reports using noble metal catalysts that are able to demonstrate FEs over 10% towards NH_3 production under ambient conditions.[9-11] However, noble metals in general are able to perform many reactions effectively, including the HER, which is main competing reaction for the ENRR. So while noble metals like Au and Pd show relative promise towards the ENRR with FEs above 10%, the complete suppression of the HER on these materials is unlikely. This in conjunction with the cost prohibitive nature of noble metals necessitates the development of non-noble metal containing materials for the ENRR.

There are many reports within the literature detailing the investigation of non-noble metal electrodes as catalysts for the ENRR. Like their noble metal counterparts, many of these systems still suffer from HER dominating at the electrode surface leading to low FEs for NH_3 production. However, within the past couple of years there has been innovative work using novel electrode designs to enhance the ENRR such as a report using a molten hydroxide electrolyte and a Fe based electrode capable of achieving a remarkable FE of 35%.[12] Several recent studies have also investigated the coating of noble metal electrodes with a metal organic framework (MOF) or zeolitic imidazolate framework (ZIF) layer to suppress the HER leading to an increased selectivity of the ENRR by limiting the number of protons that have access to the electrode surface.[13-15] While some of these new system designs may contain noble metals as the active material or contain non-ambient reaction conditions, they are likely not the final form of an ENRR cell and instead provide

innovative and stimulating results to further investigate novel systems containing non-noble metals to improve the FE of ENRR.

Recently, there have been exciting developments using electrodes containing the p-block element Bi for the ENRR, demonstrating FEs up to 66% in aqueous media.[16-18] While the exact mechanism for the impressive performance of Bi is not well understood, it is known that Bi is a relatively poor HER catalyst because of its predicted proton binding affinity being outside the ideal range for hydrogen evolution.[19] Proposed qualitative relationships between the rate of the HER and the rate of ENRR with respect to the proton concentration and electron concentration also suggest that Bi may be a promising candidate. Here the authors do not suggest "electron concentration" as a physical representation of the true electron concentration but instead as a way to account for when the electron transfer is rate limiting.[20] Their work proposes that the rate of the HER is approximately first order with respect to the electron concentration (i.e. electron transfer rate) of the electrode, while the ENRR is zeroth order. This means that as the electron concentration decreases, the ENRR rate will not be strongly affected while the HER rate will decrease exponentially. As a semi-metal Bi has a relatively low amount of electrons available and lower conductivity when compared to a metal like Cu,[21] and based upon the proposed rate relationships described above, this decreased electron concentration and conductivity helps suppress the HER while not affecting the ENRR.[20] It has also been demonstrated through DFT calculations that Bi 6p orbitals may be advantageously positioned to interact with the N 2p orbitals, allowing for effective back bonding into the N_2 triple bond, weakening the bond overall and allowing for a stronger interaction between the N_2 molecule and the Bi surface.[16] These inherent properties make Bi a promising potential candidate for the ENRR in aqueous media.

Another recent report exploring surface-modified Bi containing systems by Jang *et al* showed increased selectivity in the low bias region for ENRR by creation of a thin layer of $BiPO_4$ on the surface by cyclic voltammetry in 0.5 M phosphate buffer (pH 7.5).[22] Without this $BiPO_4$ layer the highest FE they could achieve was 3.7%, but with the $BiPO_4$ layer the FE increased to 5.6%, and with the incorporation of V ions within the $BiPO_4$ layer the FE increased even further to 13.2%. While they do not directly elucidate the mechanism by which the incorporation of V and P at the surface enhances the ENRR, they do provide a possible hypothesis based upon their linear sweep voltammetry's. The presence of V and P ions as vanadate and phosphate may inhibit the reduction of Bi^{3+} to Bi^0 during the reductive conditions of the ENRR. This inhibition allows for the possibly increased presence of Bi^{3+} during the ENRR, which may provide a more active site towards N_2 reduction.

The success of Bi materials showing high selectivity for the ENRR provoked me to wonder if Sb, another semi-metal directly above Bi in the periodic table, may show similar or even better performance for the ENRR when compared to Bi. Sb has seen very little attention within the ENRR field compared to Bi. A handful of reports from the past several years using complex systems containing Sb (e.g. antimony sulfide/tin oxide, antimony/antimony oxide, antimony phosphate/carbon) have demonstrated high performance for the ENRR (up to 34% FE),[23-25] however, the reasoning for the high performance and role of Sb and its oxides is unclear. No theoretical investigations examining the binding affinities for either protons or N-containing species have been performed for Sb and while it is possible to assume that Sb will possess similar properties to Bi on account of being in the same column and also possessing semi-metallic properties, it is unknown how Sb alone may perform for the ENRR. This relative lack of understanding provides ample room for investigations into how well Sb and Sb-containing

materials perform the ENRR and how they compare to relatively high performing catalysts such as Bi.

Understanding the individual properties and performance of an element like Sb or Bi for the ENRR is critical to developing guidelines for future materials. However, it is unlikely that any singular element will be able to provide the required performance for widespread commercialization of the ENRR because of unsatisfactory activity or restrictive rate relationships between the HER and ENRR.[20,26] To overcome these challenges, metal alloy phases have been reported in the literature demonstrating improved performance for the ENRR when compared to their individual elements.[27-29] Wang et al. synthesized a AuCo catalyst that demonstrated a FE of 22.03% even though the individual elements of Au or Co showed less than 10% FE towards NH_3 production. They state that the increased surface area exposed more active sites for their alloy material which improved the FE% but also that their DFT calculations suggest that the transition state energy to protonate the adsorbed N_2 molecule on the surface was decreased for the AuCo alloy when compared to Au and Co metals alone.[27] Similarly, Zhang et al. synthesized a series of Ag_2X_1 (X = Au, Pt, Pd) alloys to investigate how the nature of the X element affected the ENRR performance. They found that the Ag_2Au alloy performed the best and explained this with their DFT calculations showing that electrons from the Ag atoms localized onto the Au atoms as expected from Au's higher electronegativity, generating partially positive Ag atoms and partially negative Au atoms which they said enhances the activity of the ENRR on the Au atoms.[28] These studies, and others,[29,30] have demonstrated that by combining two (or more) elements into an alloy phase, enhancements in the ENRR performance over a single element can be achieved.

In this chapter, I investigate the ENRR performance of Bi, Sb and BiSb, in collaboration with Dr. Youn Jeong Jang who was a postdoctoral scholar in our group and possessed expertise in

investigating the ENNR properties of materials. The goal of this work was two-fold. First was to examine the ENRR performances of Bi, Sb and BiSb to determine if any showed enhanced ENRR capabilities. To accurately compare each of these materials, it was critical to optimize the electrochemical synthetic procedure of each material to prepare electrodes with the same surface area and morphological features, ensuring the observed ENRR performances originated from only their compositional differences. The second goal was to determine if the performance of any of these materials can be improved through the use of a gas diffusion electrode (GDE). In a GDE, N_2 gas, not dissolved N_2, can be electrochemically reduced at the interface between N_2 gas, electrolyte and catalyst. For this reason, Bi, Sb, and BiSb were deposited onto a carbon felt electrode that can serve as both a regular electrode and as a pseudo-GDE.

Therefore, I developed an electrochemical method to synthesize thin, smooth, and conformal coatings of Bi, Sb, and BiSb on carbon felt electrodes to investigate their ability to electrochemically reduce N_2 to NH_3 in pH 9.3 borate buffer both as regular electrodes and as pseudo-GDEs. Neither Bi or Sb demonstrate FEs over 1.5% when used alone, however, by combining them into the BiSb alloy phase, a four-fold enhancement in the ENRR was observed.

5.2 Experimental

5.2.1 Materials

Potassium antimony tartrate ($K_2Sb_2(C_4H_2O_6)_2 \cdot H_2O$, 99%), bismuth(III) nitrate ($Bi(NO_3)_3 \cdot 5H_2O$, ≥98.0%), sodium hydroxide (NaOH, ≥97.0%), ethylenediaminetetraacetic acid (EDTA, 99.4-100.6%), boric acid (H_3BO_3, ≥99.5%), potassium pyrophosphate ($K_4P_2O_7$, 97%), tartaric acid ($C_4H_6O_6$, ≥99.5%), hydrochloric acid (HCl, 37%), 4-(dimethylamino)benzaldehyde ($C_9H_{11}NO$, 99%), hydrazine hydrate (N_2H_4 x H_2O, 50-60%), phosphoric acid (H_3PO_4, 85%),

deuterated water (D_2O, 99.9%) and ammonium chloride (NH_4Cl, 99%) were all purchased from Millipore-Sigma. All chemicals were used as received and without further purification. Carbon felt (AvCarb C100) was purchased from Fuel Cell Store and was cut into one cm by five cm sized strips for use as the working electrode. Deionized (DI) water with a resistivity of >18.0 MΩ·cm was used to prepare all solutions.

5.2.2 Synthesis of Sb, Bi, and BiSb

Electrodeposition was carried out in an undivided three electrode cell composed of a carbon felt working electrode, a Ag/AgCl (4 M KCl) reference electrode and a carbon rod counter electrode using a VMP2 multichannel potentiostat (Princeton Applied Research). The carbon felt electrodes were prepared by tightly wrapping the center of the 5 cm long carbon felt strip with teflon tape (J.V. Converting Company) so that only the bottom two cm of the strip was exposed to the solution. The tight wrapping of the tape also had the effect of preventing solution from traveling up the carbon felt and making contact with the alligator clip connecting the electrode to the potentiostat.

Before deposition of any species onto the carbon felt electrodes, an LSV in a separate solution containing just the tartaric acid adjusted to pH ~ 7 was performed from the open circuit potential (OCP) to -1.7 V vs Ag/AgCl. This had the effect of increasing the hydrophilicity of the carbon substrate which provided more uniform coverage of the deposited metals on the carbon felt fibers. For Sb deposition, the aqueous plating solution contained 10 mM $K_2Sb_2(C_4H_2O_6)_2 \cdot H_2O$ and 1 M tartaric acid with the pH adjusted to 7 with NaOH. The films were deposited onto carbon felt by applying -1.4 V vs Ag/AgCl for 20 seconds, passing approximately 1.6 C of charge. For Bi deposition, the aqueous plating solution contained 20 mM $Bi(NO_3)_3 \cdot 5H_2O$ and 1 M tartaric acid with the pH adjusted to 6 with NaOH. The films were deposited using a pulsed deposition by

applying a potential of -0.9 V vs AgCl for five seconds and then letting the potential return to the OCP for ten seconds. This was repeated 24 times to pass approximately 1.6 C of charge. For the deposition of BiSb, an aqueous plating solution containing 20 mM $Bi(NO_3)_3 \cdot 5H_2O$, 30 mM $K_2Sb_2(C_4H_2O_6)_2 \cdot H_2O$, and 1 M tartaric acid with the pH adjusted to 5.6 with NaOH was used. The films were deposited by applying -1.5 V vs Ag/AgCl for 20 seconds to pass approximately 1.6 C of charge.

5.2.3 Characterization

Powder x-ray diffraction (PXRD, D8 Discover, Bruker, Ni-filtered Cu Kα radiation, λ = 1.5418 Å) was used to examine the crystal structure of the electrodes. Scanning electron microscopy with an accelerating voltage of 2 keV (SEM; LEO Supra55 VP) and energy dispersive spectroscopy with an accelerating voltage of 22 keV (EDS; Noran System Seven, Thermo-Fisher, ultra-dry silicon drift detector) were used to investigate the morphology and bulk elemental ratios respectively. X-ray photoelectron spectroscopy (XPS) using a Thermo Scientific K-α X-ray photoelectron spectrometer equipped with an Al Kα excitation source was used to determine surface elemental compositions.

5.2.4 Electrochemical characterization

All J-V and J-t measurements were performed in an undivided three electrode gas-tight stainless-steel cell. To remove any impurities in the N_2 gas flow, the $^{15}N_2$ gas (98 %) was first passed through a Cu/SAPO trap as recommended in the literature.[31] The purity of the isotopically labelled $^{15}N_2$ gas is 98% ^{15}N and ≥ 99.0% N2 ($^{15}N_2$ +$^{14}N_2$) with the remaining <1% impurities identified by the manufacturer (Sigma-Aldrich) as Ar, O_2, CO_2, N_2O, and C_2H_6. Either Sb, Bi or BiSb on carbon felt was used as the working electrode, with a Ag/AgCl (3 M KCl) reference electrode and a carbon rod counter electrode. Before the measurement, the solution was purged

with N_2 gas for thirty minutes before continuous purging during the measurement. Solutions used for control experiments with Ar (99.999%) went through the same procedure. J-t measurements were performed by holding a constant potential to pass 10 C. Before any measurements, a potential of -0.6 V vs RHE for 1 minute was applied to reduce the naturally formed oxide passivation layer on the metal surfaces. All measurements were repeated with Ar flow instead of N_2 to confirm the produced NH_3 came from the reduction of N_2 gas.

All faradaic efficiency (FE) measurements were quantified using isotopically labeled $^{15}N_2$. Proton nuclear magnetic resonance (^{1}H-NMR) was used to quantify the produced $^{15}NH_3$ on a Bruker Advance III HD 600 MHz spectrometer (Bruker Biospin Corp., Billerica, MA) equipped with a TCI-F cryoprobe with z-gradient. After the J-t measurement, the electrolyte was collected and acidified to pH ~3 using H_3PO_4 and then condensed to 6 mL using reduced pressure distillation. After this, 5 v% D_2O with trimethylsilylpropanoic acid (TSP) was mixed with the solution to act as the internal reference for locking. The ^{1}H signal from the water was removed using water suppression with excitation sculpting. The quantification of $^{15}NH_3$ was not affected by water suppression because the $^{15}NH_4^+$ signal appears at 7 ppm. Spectra were acquired using 1024 scans, a relaxation delay of 1.5 s and an acquisition time of 3 s. A calibration curve was prepared using solutions of known concentration of $^{15}NH_4Cl$ in the same electrolyte used for the J-t measurements followed by the above acidification and mixing with D_2O containing TSP for locking and integrating the observed $^{15}NH_4^+$ signal for each.

The ENRR can also produce N_2H_4, therefore the Watt and Crisp method was used to determine if any N_2H_4 formed during the ENRR.[32] After the ENRR, 2 mL of the electrolyte was collected in a centrifuge tube and 2 mL of ethanol solution containing 0.7 M HCl and 0.12 M 4-(dimethylamino)benzaldehyde was added. The solution was left to react for 1 hour at room

temperature and then the absorbance was measured at 455 nm using a UV-VIS spectrophotometer. The concentration of N_2H_4 was determined by comparing the measured absorbance to a calibration curve generated using standard solutions of N_2H_4 prepared by adding N_2H_4 x H_2O into the electrolyte used in J-t measurements. No N_2H_4 was detected for any of the J-t measurements. The FE was determined using the following equation where F is Faraday's constant (96485.33 C/mol):

$$\text{FE (\%)} = \frac{3 \text{ x } n_{NH_3}\text{(mol) x F (C mol}^{-1}\text{)}}{\text{Total charged passed (C)}} \text{ x } 100$$

While a Ag/AgCl reference was used in each experiment performed, all results within this report are presented against the reversible hydrogen electrode (RHE) for direct comparison to other reports in aqueous solution but that contain different pH values. The conversion between Ag/AgCl and RHE reference electrode values can be done via the following equation:

$$E_{(\text{vs RHE})} = E_{(\text{vs Ag/AgCl})} + E_{(\text{Ag/AgCl})}\text{(reference)} + 0.0591 \text{ V x pH(at 25 °C)}$$

$$E_{\text{Ag/AgCl}}\text{(reference, 4 M KCl)} = 0.1976 \text{ V vs NHE at 25 °C}$$

$$E_{\text{Ag/AgCl}}\text{(reference, 3 M KCl)} = 0.209 \text{ V vs NHE at 25 °C}$$

5.3 Results and Discussion

5.3.1 Synthesis and Characterization of Bi, Sb, and BiSb

Carbon felt provides a high surface area substrate to deposit uniform coatings of the Bi, Sb, and BiSb catalysts onto because of the many interwoven fibers that comprise the carbon felt (**Figure 1**). It also enables the creation of a pseudo-gas diffusion electrode (pseudo-GDE) by virtue of its porous and permeable nature. This is important because a major limiting factor for the ENRR is the relatively low concentration of N_2 molecules dissolved in aqueous solution (1.4 mM N_2 at 20 °C). This low concentration is part of the reason many materials show poor ENRR performance

and overall low faradaic efficiencies (FE) when compared to hydrogen evolution. To overcome this challenge we turned to the field of CO_2 reduction, where recent research has demonstrated that by using a GDE the concentration of reactant gas molecules at the surface of the electrode can be artificially increased beyond their normal solubility in aqueous solutions.[33]

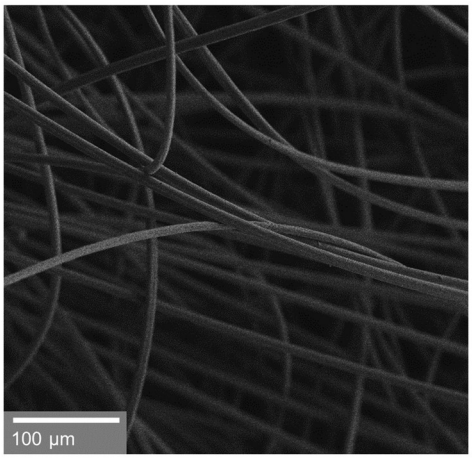

Figure 1. SEM image of the carbon fibers that make up the carbon felt electrode.

A more holistic description of the operation of a GDE can be found elsewhere,[33] however, the basic setup for a GDE is as follows. The electrolyte is separated from the gas phase by a hydrophobic, high surface material with a hydrophilic catalyst embedded on the surface which has access to both the solution and the internal structure of the polymeric material. Instead of bubbling gas into solution to dissolve N_2 within the electrolyte as is done in traditional electrochemical gas reduction experiments, the gas is instead permeated inside the polymeric material from the other side of the electrode that is not exposed to the solution. The polymeric layer is composed of a hydrophobic, porous structure that prevents electrolyte from penetrating into the porous structure. The catalyst is typically hydrophilic though, so it can interact with water in the electrolyte. This creates a three-way interface between the solid hydrophilic catalyst, liquid phase electrolyte, and gas phase N_2 molecules from the hydrophobic, porous structure (**Figure 2a**). This is advantageous

as the gas in question (N_2) can therefore be at much higher concentrations within the polymeric material than it would be in the aqueous solution, and because the catalyst has access to both the high concentration of N_2 gas and the electrolyte, it should be able to evolve NH_3 more efficiently.

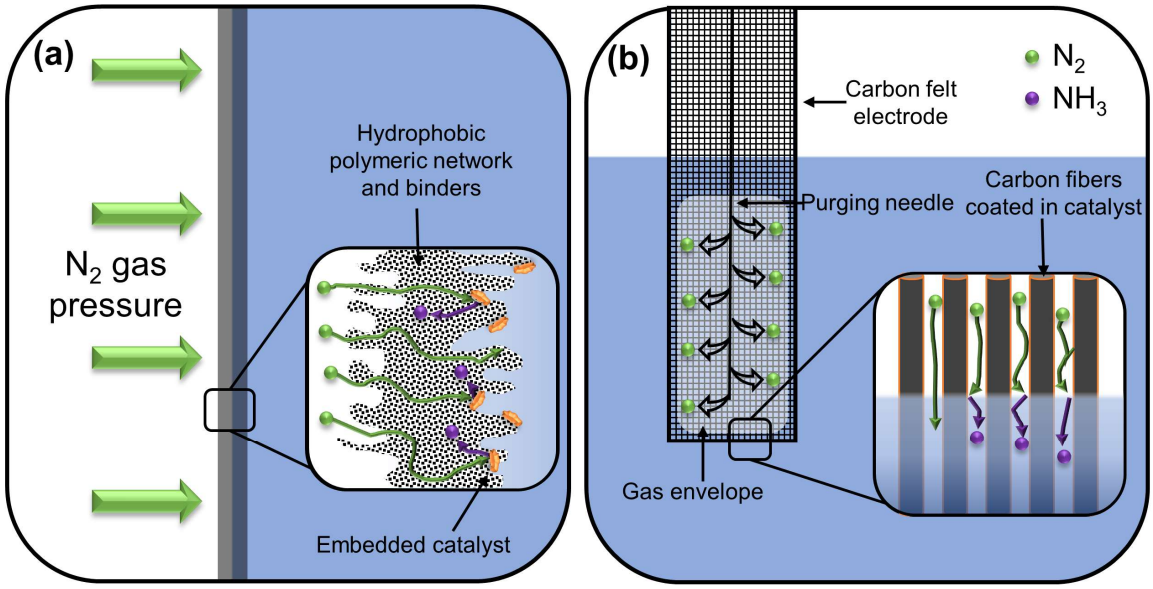

Figure 2. An illustration of how a (a) true GDE works compared to the (b) pseudo-GDE used in this study. Both demonstrate the three-way interface between the catalyst, electrolyte and gas phase N_2 in an effort to improve the ENRR performance.

The primary difference between the pseudo-GDE used in this study and a true one as described above is how the creation of this three-way interface forms. For the carbon felt electrode it is not normally hydrophobic and thus electrolyte is able to permeate throughout it, which allows for its use as a high surface area, normal electrode. To create the pseudo-GDE, a needle is inserted into the carbon felt electrode and N_2 gas flows through the needle. The gas then exits the needle through the various side openings present and moves through the void spaces within the carbon felt (**Figure 1**), expelling the solution to create a gas envelope within the carbon felt electrode (**Figure 2b**). By adjusting the pressure of N_2 gas coming from the needle, the three-way interface between the N_2 gas envelope, solid catalyst on the carbon fibers and liquid electrolyte can be achieved. The pseudo-GDE used in this study and a true GDE both enjoy increased concentration

of gas to use as a reactant, however, the creation of a true GDE requires the use of binders, a conductive polymeric network, and a particulate catalyst necessitating a more complex synthesis process and a special cell designed for gas flow and product collection,[33] while the pseudo-GDE used here simply requires a needle and a carbon felt electrode, greatly simplifying the process to examine how increased concentration of reactant gas may improve the ENRR.

The goal of the synthetic approach for the electrodes used in this study is to produce a morphology that is relatively comparable between each material on carbon felt. This removes the potentially complicating factors that different morphologies may introduce with respect to different surface areas and possibly different exposed crystal sites when comparing their ENRR performance. While Chapter Four demonstrated the ability to produce homogenous BiSb on FTO through the use of an acidic plating solution containing nitric acid to solvate the Bi precursor, this procedure was unable to be used to deposit the metals onto carbon felt without producing variable and non-uniform morphologies. Therefore, I sought to investigate the electrodeposition of Bi, Sb, and BiSb using neutral or basic conditions. However, because of Bi's insolubility under neutral or basic conditions,[8] a complexing agent was required to prevent the precipitation of Bi and thus I first optimized a plating solution that was able to reliably solvate Bi and deposit a uniform Bi layer on carbon felt electrodes.

Several complexing agents are known within the literature to solvate Bi under neutral and basic conditions including tartrate, potassium pyrophosphate, and EDTA.[34] I found that all three were able to dissolve bismuth nitrate at pH 10 with EDTA dissolving Bi within one hour, tartrate within three hours, and potassium pyrophosphate taking over ten hours to completely dissolve the Bi precursor. However, I settled on using a tartrate containing solution as EDTA and potassium pyrophosphate both caused a normally water soluble antimony precursor, potassium antimony

tartrate, to precipitate out of the solution, while the tartrate plating solution was able to successfully solvate both Sb and Bi precursors. The optimized plating solution to deposit Bi onto carbon felt contained bismuth nitrate and tartaric acid with the pH adjusted to 6 using sodium hydroxide. A pulsed deposition with the application of a potential negative enough to reduce Bi^{3+} to Bi^{0}, which then precipitated out onto the carbon felt, was applied, followed by a longer rest period which allowed for Bi^{3+} ions to be replenished at the electrode surface. I found this to produce a more uniform morphology with good coverage (**Figure 3a**) when compared to a non-pulsed deposition.

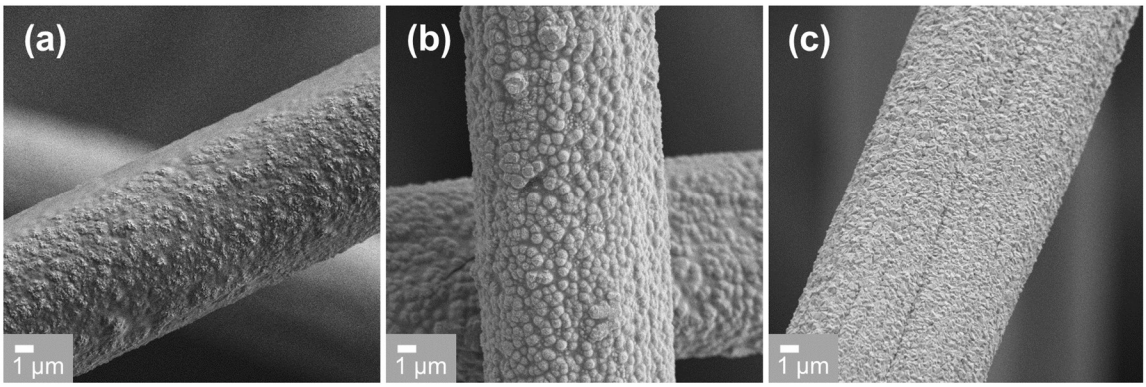

Figure 3. SEM images of (a) Bi, (b) Sb, and (c) BiSb deposited onto a carbon fiber within the carbon felt.

Utilizing the same plating solution but switching out bismuth nitrate for potassium antimony tartrate and applying a negative enough potential to reduce Sb^{3+} to Sb^{0}, Sb was deposited onto carbon felt. A pulsed deposition was not necessary for Sb to produce a uniform morphology with good coverage (**Figure 3b**). The deposition of Bi and Sb together as BiSb on carbon felt (**Figure 3c**) was achieved by dissolving both bismuth nitrate and potassium antimony tartrate into the tartrate plating bath and applying a constant potential that was negative enough to reduce Bi^{3+} to Bi^{0} and also reduce Sb^{3+} to Sb^{0}. X-ray diffraction (XRD) was used to determine the crystalline nature of Sb, Bi, and BiSb on carbon felt (**Figure 4**). For Sb and Bi alone, peaks corresponding to a single crystalline phase of Sb or Bi metal were observed in **Figures 4a and 4b** respectively. Both

Bi and Sb possess the same crystal structure and therefore they are expected to show the same crystal pattern, except that Sb has peaks shifted to slightly higher two theta values because of a smaller atomic size. Because the BiSb crystal structure is the same as that of Bi and Sb, its unit cell is an average of the two unit cells for Bi and Sb leading to the peak positions being an average of Bi and Sb.[35] The 1:1 phase will therefore have peaks that appear directly in-between that of pure Bi and pure Sb. For my prepared BiSb electrode, diffraction peaks in the middle of Bi and Sb were observed corresponding to the desired 1:1 BiSb alloy phase, but also peaks corresponding to crystalline Bi metal. This matched with the energy dispersive spectroscopy (EDS) results showing a bulk elemental ratio of 2:1 Bi:Sb, indicating excess Bi deposited onto the carbon felt along with the desired 1:1 phase.

The identity of this excess crystalline Bi phase can be elucidated by examining the standard reduction potentials of Bi and Sb, as well as the corresponding LSVs of each plating solution (**Figure 5**). The excess Bi is deposited onto the carbon felt electrodes during the very beginning of the BiSb deposition because it is easier to reduce Bi in the tartrate plating solution than Sb. This can be observed by examining the relative current onset in the LSVs of the plating solutions containing Sb alone, Bi alone and BiSb together **(Figure 5)**, where the plating solutions containing Bi show a significantly earlier reduction peak than that of the solution containing only Sb. This means that when a potential is first applied, Bi^{3+} ions have a higher driving force than Sb^{3+} ions to be reduced and precipitate first at the electrode surface. The Bi^{3+} ions closest to the electrode surface are therefore deposited first, but once they are depleted and Bi deposition is limited by diffusion from the surrounding bulk solution, Sb^{3+} ions are now able to be reduced in tandem with the Bi^{3+} ions diffusing to the electrode surface, producing the desired 1:1 phase on top of a Bi rich layer.

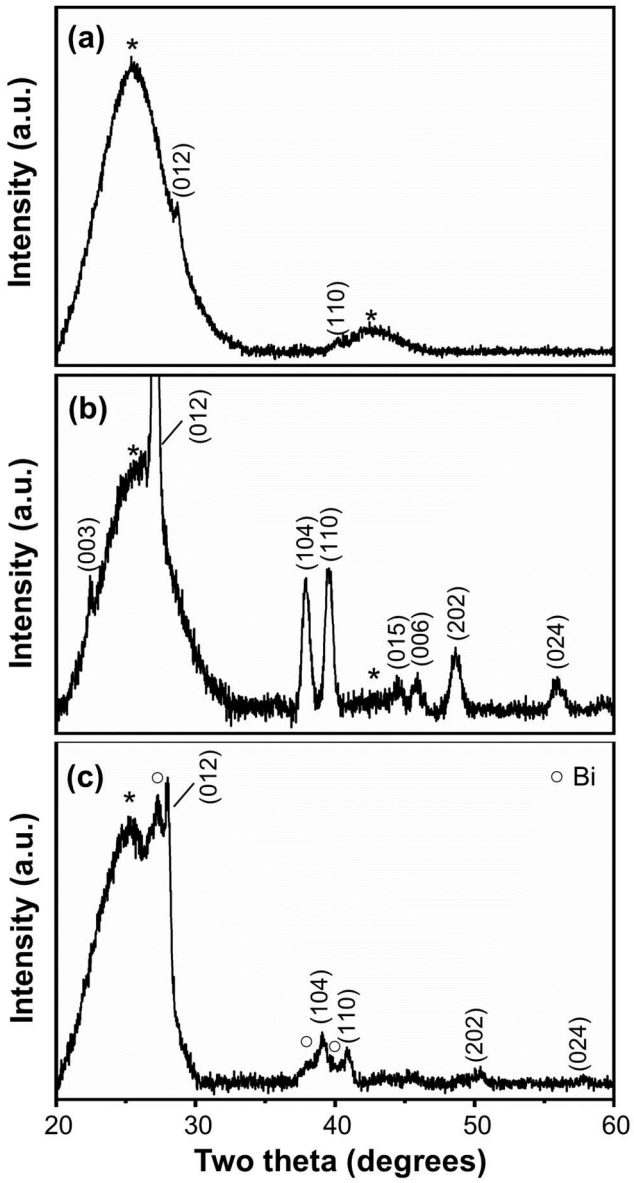

Figure 4. XRD patterns of as deposited (a) Sb, (b) Bi, and (c) BiSb on carbon felt. The (hkl) indices are assigned from the PDF cards for Sb (35-0732) and Bi (44-1246). The broad peaks corresponding to the carbon felt are denoted by an asterisk.

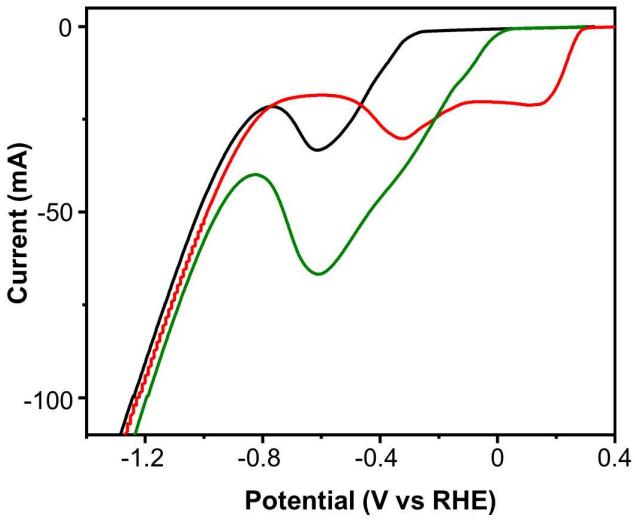

Figure 5. LSVs at a scan rate of 10 mV/sec using a carbon felt electrode in Bi (red), Sb (black) and BiSb (green) plating solutions. The Bi solution contained 20 mM Bi, the Sb solution contained 20 mM Sb, the BiSb solution contained 20 mM Bi and 20 mM Sb and each contained 1 M tartrate with the pH adjusted to pH 6 using NaOH.

To determine the validity of this hypothesis, the surface layer of the BiSb electrodes was examined with x-ray photoelectron spectroscopy (XPS). A 1:1 surface elemental ratio between Bi and Sb was calculated from the Bi and Sb regions, confirming that the surface is composed of the desired 1:1 Bi:Sb alloy phase. Therefore, while the bulk of the electrode is not composed of one homogenous phase, the surface layer where the ENRR is occurring is composed of a single, pure 1:1 BiSb phase, which is critical to be able to accurately compare each material with one another.

5.3.2 ENRR performance of Bi and Sb

The ENRR performances of Bi and Sb were investigated through a series of LSVs and J-t measurements. **Figure 6a** shows LSVs in 0.5 M borate (pH 9.3) for the Bi-coated carbon felt electrode when using Ar or N_2 as the gas, as well as, bubbling outside of the carbon felt electrode treating the carbon felt electrode as a standard high surface electrode and then inserting the needle inside the carbon felt electrode to examine the effect of creating a pseudo-GDE. Ar gas is used as a control in which the only expected reaction is the HER. A change in current density when using

N_2 instead of Ar therefore indicates an interaction of the electrode with N_2, however, this does not directly correlate with the performance of a material. For the Bi electrodes, little difference is observed when using N_2 gas over Ar, although this does not mean that the Bi electrode is inert towards N_2 reduction as electrons that was originally going towards the HER may now by being used for the ENRR. An overall decrease in current density for both Ar and N_2 is observed when the gas needle is inserted into the carbon felt electrode to create the pseudo-GDE. The gas envelope inside the carbon felt electrode effectively decreases the surface area of the catalyst that is in direct contact with the electrolyte, which will decrease the total area that performs the HER.

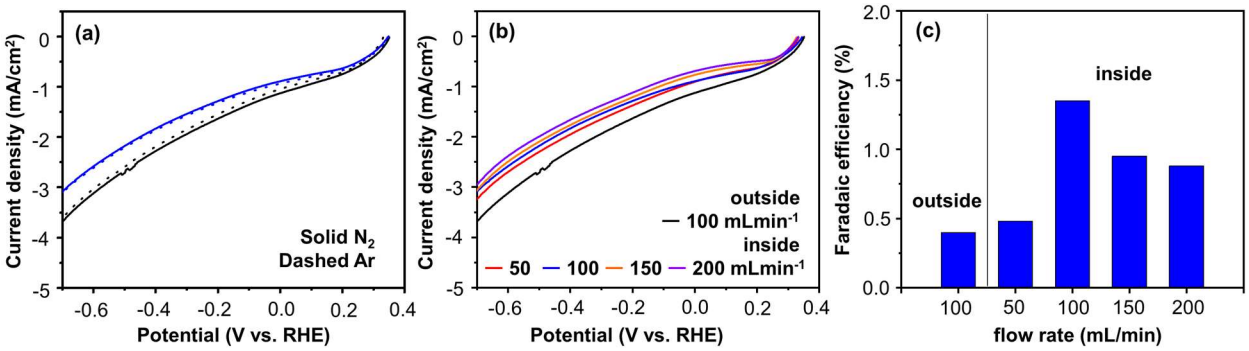

Figure 6. (a) LSVs of Bi while using Ar or N_2 gas outside (black) or inside (blue) the carbon felt electrode. (b) LSVs with N_2 both outside and inside the carbon felt electrode using different gas flow rates. (c) Faradaic efficiency for Bi electrodes for NH_3 production at -0.6 V vs RHE using different flow rates of N_2 gas. All measurements were performed in 0.5 M borate (pH 9.3). Data collected by Dr. Youn Jeong Jang.

Figure 6b shows that as the gas flow rate is increased when the needle inside the electrode the observed current density decreases. This is expected as the gas moving through the void space inside the carbon felt electrode displaces the electrolyte solution as it escapes, which decreases the total active surface area exposed to solution, thereby decreasing the observed current density. To determine how the pseudo-GDE affects the ENRR performance of Bi coated on the carbon felt, a series of J-t measurements at -0.6 V vs RHE were performed using different gas flow rates inside the carbon felt electrode and the FE for NH_3 production was measured (**Figure 6c**). The FE was

higher in all cases of flowing N_2 inside the electrode indicating that our pseudo-GDE did indeed improve the observed ENRR performance of the Bi electrode when compared to placing the needle outside the electrode. A sweet spot that optimizes the amount of catalyst that is exposed to the three-way interfacial area of N_2 gas, catalyst, and electrolyte in conjunction with the exposure of the catalyst to dissolved N_2 in the electrolyte was determined at a flow rate of 100 mL/min where the FE was almost tripled when compared to the needle bubbling N_2 to dissolve into the electrolyte outside the electrode at the same flow rate, while increasing the flow rate past this value decreased the observed FE.

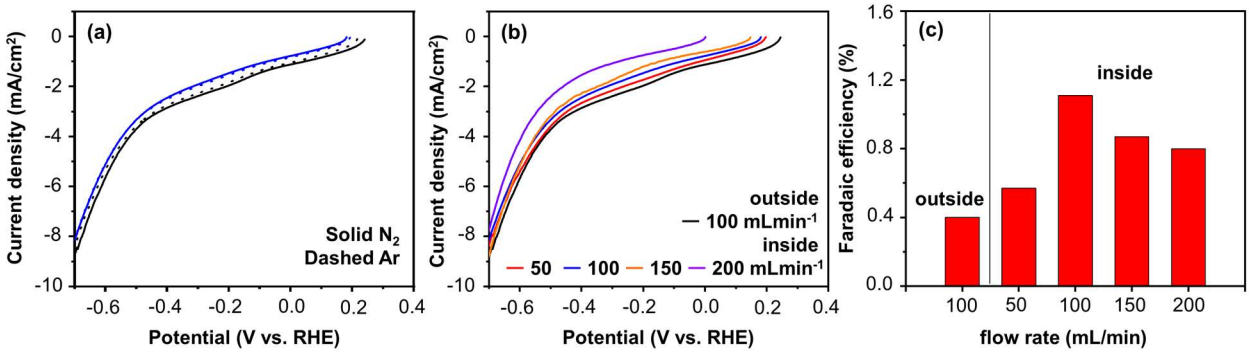

Figure 7. (a) LSVs of Sb while using Ar or N_2 gas outside (black) or inside (blue) the carbon felt electrode. (b) LSVs with N_2 both outside and inside the carbon felt electrode using different gas flow rates. (c) Faradaic efficiency for Sb electrodes for NH_3 production at -0.6 V vs RHE using different flow rates of N_2 gas. All measurements were performed in 0.5 M borate (pH 9.3). Data collected by Dr. Youn Jeong Jang.

These results were very exciting, indicating that a relatively simple pseudo-GDE can improve the FE of Bi electrodes significantly. Therefore, the same series of experiments were also performed on the Sb-coated carbon felt electrodes in 0.5 M borate (pH 9.3) (**Figure 7**). The Sb electrodes demonstrated a similar pattern as the Bi electrodes where no noticeable change occurred when using N_2 instead of Ar and the overall current decreased when the gas needle was inside the carbon felt (**Figure 7a,b**). Like with the Bi electrodes, creating the three way interfacial area inside the carbon felt demonstrated a higher ENRR performance for the Sb electrodes with the observed

FE almost tripling at a 100 mL/min flow rate (**Figure 7c**). The carbon felt electrode itself was also tested for ENRR capabilities, as well as to determine if it may contribute trace amounts of N-containing species as the precursor material (poly-acrylonitrile) for the carbon fiber synthesis contains N. No NH_3 was observed after J-t measurements were performed under the same conditions used for the Bi and Sb FE measurements. The N_{1s} region of the XPS spectrum (**Figure 8**) of the carbon felt before the J-t measurement also shows no peak associated with N, indicating a lack of possible trace N contaminants in the underlying carbon felt, further verifying the observed NH_3 comes from the reduction of N_2 gas on the Bi or Sb surfaces.

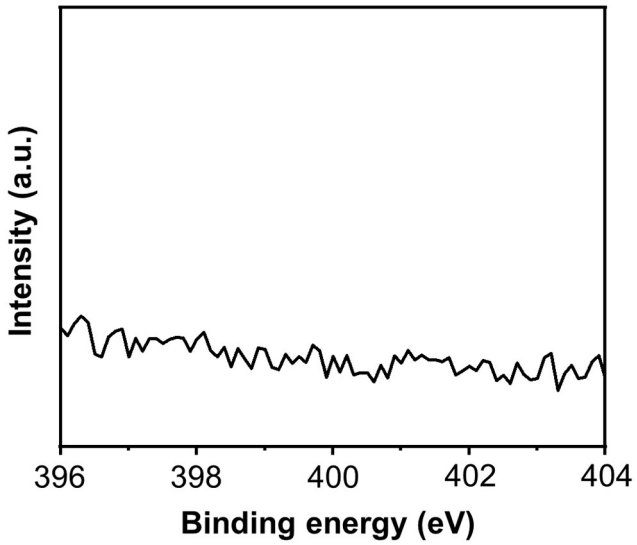

Figure 8. XPS spectrum of the N 1s region for bare carbon felt before a J-t measurement. Data collected by Dr. Youn Jeong Jang.

Overall, the pseudo-GDE demonstrates significantly improved ENRR performance for both Bi and Sb deposited on the carbon felt, with an almost tripled FE observed for creating the three-way interfacial region inside the carbon felt. While the maximum observed FEs for both Sb and Bi in this study were not exceptional, by synthesizing electrodes with uniform, smooth morphologies and similar surface areas a more accurate comparison can be made between these two elements. The FEs for Bi and Sb were observed to be relatively similar (~1.1% for Sb and

~1.4% for Bi) under the same conditions, suggesting that Sb could potentially demonstrate the same remarkable FE observed for optimized Bi electrodes in the literature.

5.3.3 ENRR performance of BiSb

The ENRR performance of the alloy phase BiSb was examined in the same manner as Bi and Sb alone. **Figure 9a,b** shows the LSVs of the BiSb electrode in 0.5 borate (pH 9.3). The same trends were observed for BiSb as was seen for Bi and Sb alone, where there is no difference in the LSVs between using Ar or N_2 gas and that inserting the gas needle inside the electrode decreases the current density because of displacement of solution inside the electrode by the gas. However, upon measuring the NH_3 production after the J-t measurement under different flow rates, a remarkably increased FE is observed for the BiSb electrode (**Figure 9c**) when compared to the Bi and Sb electrodes alone. Even when the gas needle is used outside the electrode to dissolve N_2 into solution, the FE for BiSb (~1.0%) is almost as high as that observed for Bi (1.4%) and Sb (1.1%) when the gas needle is inside the carbon felt electrode. When using the pseudo-GDE setup for BiSb, the FE reaches ~5.1% at a 100 mL/min flow rate of N_2 gas, an almost 4x increase of FE for NH_3 production when compared to Bi or Sb alone. A series of J-t measurements was performed to determine if this significantly improved FE was universally observed at different applied potentials. The measured FE values are presented in **Figure 10**. While the relative increase of the FE for BiSb compared to Bi or Sb varies across the different applied potentials, it is always higher than Bi or Sb with a maximum FE towards NH_3 of 5.1% at -0.6 V vs RHE. Applied potentials higher than -0.6 V lead to a decrease in the measured FE for all materials, likely arising from the increased competition of the HER.

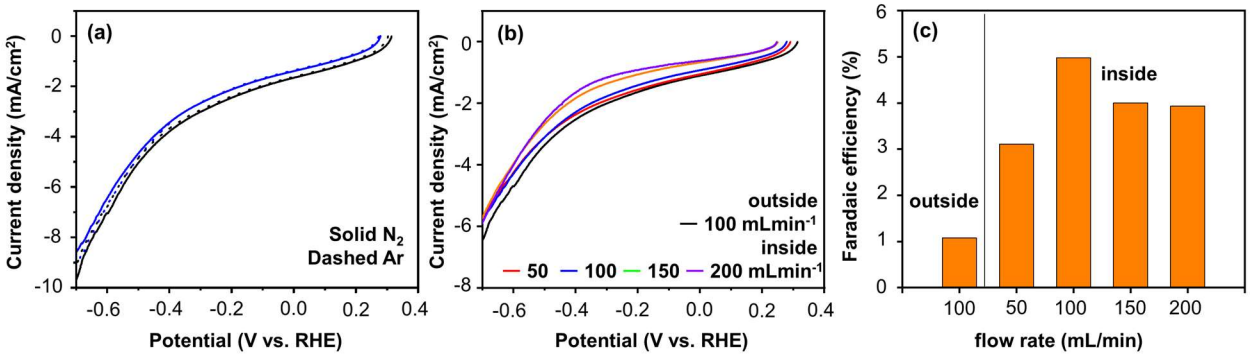

Figure 9. (a) LSVs of BiSb while using Ar or N_2 gas outside (black) or inside (blue) the carbon felt electrode. (b) LSVs with N_2 both outside and inside the carbon felt electrode using different gas flow rates. (c) Faradaic efficiency for BiSb electrodes for NH_3 production at -0.6 V vs RHE using different flow rates of N_2 gas. All measurements were performed in 0.5 M borate (pH 9.3). Data collected by Dr. Youn Jeong Jang.

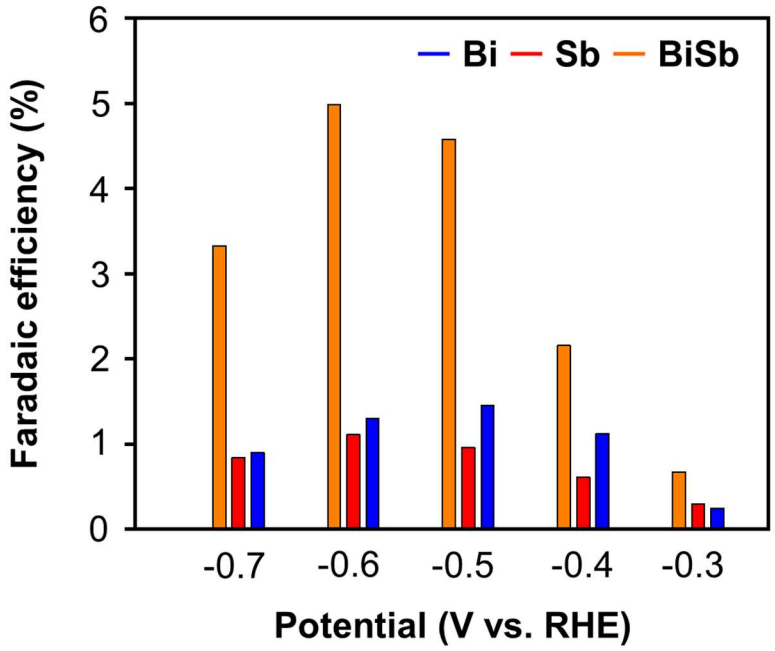

Figure 10. The Faradaic efficiencies for NH_3 production for each material at different applied potentials in 0.5 M borate (pH 9.3). Data collected by Dr. Youn Jeong Jang.

While the understanding of the ENRR mechanism and what affects the production of NH_3 is overall in its infancy, several studies have suggested that the more active sites for Bi or Sb containing electrodes are not composed of the metallic species but instead of the oxides.[22,24] However, the oxides are readily reduced under the conditions used to perform the ENRR, limiting their ability to participate in the ENRR. Interestingly, a very recent report has demonstrated the

ability to retain more Bi^{3+} during the ENRR in the form of phosphates and vanadates even under reductive bias conditions where Bi^{3+} in Bi_2O_3 is expected to be reduced. By retaining more Bi^{3+} the authors observed a dramatically improved performance towards the ENRR.[22] Therefore, we wondered if a similar effect could possibly be occurring here between Sb and Bi whereby the formation of the alloy BiSb phase resulted in the development of partial charges on Bi or Sb or both that enhance the adsorption of N_2 onto the electrode surface.

In order to probe this hypothesis, we returned to the XPS spectra originally obtained to verify that the BiSb electrode had an elemental surface ratio of 1:1 Bi:Sb. When originally collected, nothing seemed out of the ordinary for either the Bi or Sb regions in the BiSb electrode and quantification proceeded smoothly, however, it was not until they were compared with the Bi and Sb alone XPS spectra that a curious observation was made. The binding energies for the Sb metal peaks in the BiSb electrode were shifted slightly in the negative direction when compared to Sb alone, indicating the Sb in BiSb had a slight partial negative charge. Correspondingly, the binding energies for the Bi metal peaks in the BiSb electrode were shifted slightly in the positive direction when compared to Bi alone, indicating the Bi in BiSb had a slight partial positive charge.

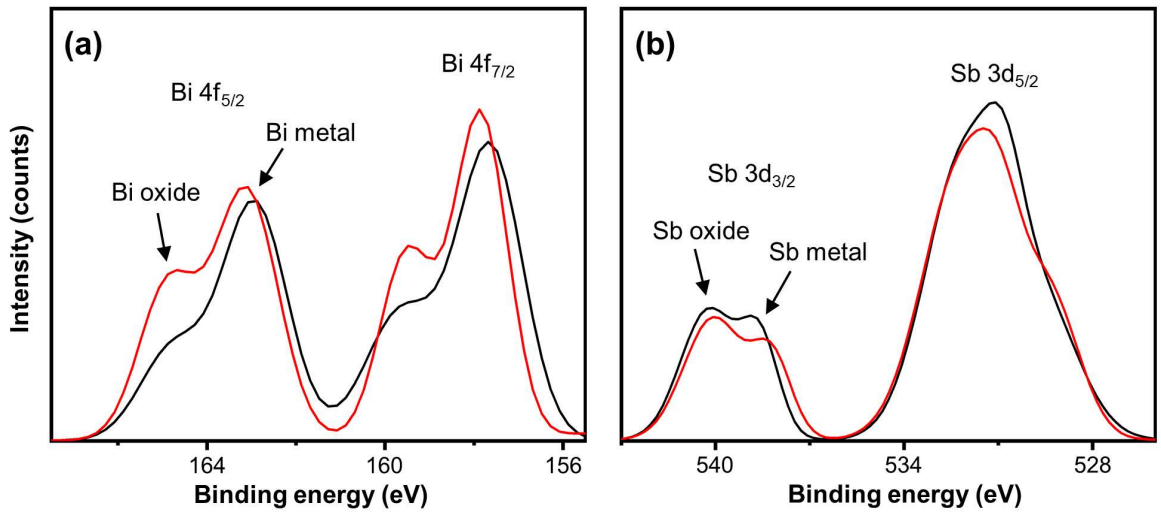

Figure 11. XPS spectra of the (a) Bi 4f region and (b) Sb 3d region representing either Bi or Sb alone (black) or Bi and Sb together in BiSb (red). Data collected by Dr. Youn Jeong Jang.

Figure 11 shows overlaid spectra of Bi in BiSb and Bi alone, and Sb in BiSb and Sb alone that demonstrate this slight shift in binding energies. These observations provide strong evidence that a slight charge transfer is occurring between the Bi and Sb atoms, which may be influencing their ability to perform the ENRR. The presence of Bi and Sb oxides in the XPS spectra is expected as neither are noble metals and will react with oxygen in the air to form surface oxides. These oxides are purposefully reduced to their metallic form before any J-t measurement is performed (see the experimental section) otherwise they would be reduced during the J-t measurement, potentially convoluting the observed results.

Whether it is the partial positive on Bi, the partial negative on Sb, or both elements possessing a partial charge improving the ENRR performance is unclear. Work by Jang et al. and Bat-Erdene et al. suggest that Bi^{3+} and Sb^{3+} respectively are the more active sites when compared to just Bi^{0} and Sb^{0} for the ENRR leading to the notion that it is positively charged species improving the ENRR performance.[21,23] However, work by Zhang et al. suggests that partially negative Au atoms in an Ag_2Au alloy are the active sites for the ENRR indicating that the more anionic species in the material is the more active site for the ENRR.[27] It is also unknown the origin of these partial charges, as the difference in electronegativity for these two elements is less than 0.02,[36] suggesting another effect is causing the partial charges on Bi and Sb. In order to confirm the XPS results and elucidate the origin and effect on the ENRR of these partial charges a theoretical collaboration was recently started with Professor Fredrickson's group here at UW-Madison. Their preliminary results do demonstrate that Sb develops a partial negative charge and that Bi develops a partial positive charge upon creation of an alloy phase between the two elements, helping to confirm the validity of the XPS results. This collaboration is currently ongoing to help

understand the origin of these partial charges as well as which element, or both, is acting as the active site.

Furthermore, to understand whether it is the partially negative Sb or partially positive Bi species (or if both are) affecting the ENRR performance, a library of alloys is proposed to be synthesized. The goal of this is to create alloys that demonstrate higher partial charges on either Sb or Bi to determine if having more of a partial charge will increase the ENRR performance of the resulting material. For example, by alloying Bi with a more electronegative metal to form a more electropositive Bi and then examining its ENRR performance one could elucidate if it is the partial positive charge on Bi that is the main active site, as a more partial positive Bi would lead to an even greater ENRR performance. An ideal candidate would be the most electronegative metal, Au, which is known to form several alloys with Bi including $AuBi_3$ and Au_2Bi.[37,38] On the other hand, if it is the partially negative Sb that is the more active site, alloying Sb with a more electropositive metal could improve the ENRR performance. Examples include Zn which forms numerous alloys with Sb including ZnSb and Zn_3Sb_2 or Mn which also forms a multitude of alloys including Mn_2Sb and MnSb.[39-41] Combining these proposed experiments with theoretical calculations of the lowest energy states for ENRR intermediates on Bi, Sb and BiSb can illuminate what the active site may be and whether it is the partially positive Bi or partially negative Sb or that both are critical to the improved performance.

5.4 Conclusions

In summary, the performance of Bi, Sb, and BiSb has been investigated in 0.5 M borate (pH 9.3) for the ENRR using a novel pseudo-GDE. By creating a three-way interface between the solid catalyst, liquid electrolyte, and gas phase N_2 inside the carbon felt electrode the FEs of Sb

and Bi increased by approximately three-fold while the FE of the BiSb electrode increased by approximately five-fold. This demonstrates a relatively simple electrode system change can dramatically improve the ENRR performance of a material which enables ease of testing the effect of increasing the gas concentration has on a system without the complexities associated with a real GDE. Bi and Sb themselves showed comparable FEs (1.4% and 1.1%) towards NH_3 production indicating that Sb performs the ENRR on a similar level as Bi, suggesting that with improved morphological and surface area modifications it may be able to achieve the same high FE values of Bi as observed in the literature. The incredible four-fold increase of FE when using the BiSb alloy over the individual elements of Bi and Sb highlights how combining different elements can improve the ENRR. The XPS results show that Bi and Sb metal species in BiSb no longer have a neutral charge and are partially charged positively and negatively respectfully, which could be increasing the absorption of N_2 which leads to an enhancement in the ENRR. However, it is not clear from this work alone whether it is the partially positive Bi or partially negative Sb that improve the FE. Further experimental work investigating other alloy phases that produce a more partial charge on either Sb or Bi is required to determine which metal is playing a more active role in the ENRR. Finally, theoretical calculations of the binding energies of ENRR intermediates on Bi, Sb, and BiSb surfaces may provide clues as to which of the elements is the active site and how combining them dramatically improves the ENRR.

5.5 References

1. Smil, V. Detonator of the population explosion. *Nature*. **1999**, *400*, 415.

2. Haber, Fritz (**1905**). Thermodynamik technischer Gasreaktionen (in German) (1st ed.). Paderborn: Salzwasser Verlag. ISBN 9783864448423.

3. U.S. Geological Survey, **2020**, Mineral commodity summaries 2020: U.S. Geological Survey, 200 p., https://doi.org/10.3133/mcs2020

4. Erisman, J.; Sutton, M.; Galloway, J.; Klimont, Z.; Winiwarter, W. How a century of ammonia synthesis changed the world. *Nature*. *Geosci*., **2008**, *1*, 636–639).

5. Rafiqul, I.; Weber, C.; Lehmann, B.; Voss, A. Energy efficiency improvements in ammonia production—perspectives and uncertainties. *Energy,* **2002**, *30*, 2487-2504.

6. Chen, J. G.; Crooks, R. M.; Seefeldt, L. C.; Bren, K. L.; Bullock, R. M.; Darensbourg, M. Y.; Holland, P. L.; Hoffman, B.; Janik, M. J.; Jones, A. K.; Kanatzidis, M. G.; King, P.; Lancaster, K. M.; Lymar, S. V.; Pfromm, P.; Schneider, W. F.; Schrock, R. R., Beyond fossil fuel–driven nitrogen transformations. *Science* **2018**, 360, eaar6611.

7. Smith, C.; Hill, A. K.; Torrente-Murciano, L., Current and future role of Haber–Bosch ammonia in a carbon-free energy landscape. *Energ. Environ. Sci.* **2020,** *13*, 331-344.

8. Pourbaix, M., *Atlas of Electrochemical Equilibria in Aqueous Solutions.* 2 ed.; National Association of Corrosion Engineers: Houston, Texas, 1974; p 524-532.

9. Bao, D.; Zhang, Q.; Meng, F.-L.; Zhong, H.-X.; Shi, M.-M.; Zhang, Y.; Yan, J.-M.; Jiang, Q.; Zhang, X.-B., Electrochemical Reduction of N_2 under Ambient Conditions for Artificial N_2 Fixation and Renewable Energy Storage Using N2/NH3 Cycle. *Adv. Mater.* **2017,** *29*, 1604799.

10. Nazemi, M.; Panikkanvalappil, S. R.; El-Sayed, M. A., Enhancing the rate of electrochemical nitrogen reduction reaction for ammonia synthesis under ambient conditions using hollow gold nanocages. *Nano Energy* **2018,** *49*, 316-323.

11. Li, S.-J.; Bao, D.; Shi, M.-M.; Wulan, B.-R.; Yan, J.-M.; Jiang, Q., Amorphizing of Au Nanoparticles by CeO_x–RGO Hybrid Support towards Highly Efficient Electrocatalyst for N_2 Reduction under Ambient Conditions. *Adv. Mater.* **2017,** *29*, 1700001.

12. Licht, S.; Cui, B.; Wang, B.; Li, F.-F.; Lau, J.; Liu, S., Ammonia synthesis by N_2 and steam electrolysis in molten hydroxide suspensions of nanoscale Fe_2O_3. *Science* **2014,** *345*, 637-640.

13. Koh, C. S. L.; Lee, H. K.; Fan Sim, H. Y.; Han, X.; Phan-Quang, G. C.; Ling, X. Y., Turning Water from a Hindrance to the Promotor of Preferential Electrochemical Nitrogen Reduction. *Chem. Mater.* **2020,** *32*, 1674-1683.

14. Lee, H. K.; Koh, C. S. L.; Lee, Y. H.; Liu, C.; Phang, I. Y.; Han, X.; Tsung, C.-K.; Ling, X. Y., Favoring the unfavored: Selective electrochemical nitrogen fixation using a reticular chemistry approach. *Sci. Adv.* **2018,** *4*, eaar3208.

15. Yang, Y.; Wang, S.-Q.; Wen, H.; Ye, T.; Chen, J.; Li, C.-P.; Du, M., Nanoporous Gold Embedded ZIF Composite for Enhanced Electrochemical Nitrogen Fixation. *Angew. Chem. Int. Edit.* **2019,** *58*, 15362-15366.

16. Hao, Y. C.; Guo, Y.; Chen, L. W.; Shu, M.; Wang, X. Y.; Bu, T. A.; Gao, W. Y.; Zhang, N.; Su, X.; Feng, X.; Zhou, J. W.; Wang, B.; Hu, C. W.; Yin, A. X.; Si, R.; Zhang, Y. W.; Yan, C. H., Promoting nitrogen electroreduction to ammonia with bismuth nanocrystals and potassium cations in water. *Nat. Catal.* **2019,** *2*, 448-456.

17. Wang, Y.; Shi, M.-m.; Bao, D.; Meng, F.-l.; Zhang, Q.; Zhou, Y.-t.; Liu, K.-h.; Zhang, Y.; Wang, J.-z.; Chen, Z.-w.; Liu, D.-p.; Jiang, Z.; Luo, M.; Gu, L.; Zhang, Q.-h.; Cao, X.-z.; Yao, Y.; Shao, M.-h.; Zhang, Y.; Zhang, X.-B.; Chen, J. G.; Yan, J.-m.; Jiang, Q., Generating Defect-Rich Bismuth for Enhancing the Rate of Nitrogen Electroreduction to Ammonia. *Angew. Chem. Int. Edit.* **2019,** *58*, 9464-9469.

18. Li, L.; Tang, C.; Xia, B.; Jin, H.; Zheng, Y.; Qiao, S.-Z., Two-Dimensional Mosaic Bismuth Nanosheets for Highly Selective Ambient Electrocatalytic Nitrogen Reduction. *ACS Catal.* **2019,** *9*, 2902-2908.

19. Trasatti, S. Work function, electronegativity, and electrochemical behaviour of metals: III. Electrolytic hydrogen evolution in acid solutions. *J. Electroanal. Chem.* **1972**, *39*, 163–184.

20. Singh, A. R.; Rohr, B. A.; Schwalbe, J. A.; Cargnello, M.; Chan, K.; Jaramillo, T. F.; Chorkendorff, I.; Nørskov, J. K., Electrochemical Ammonia Synthesis—The Selectivity Challenge. *ACS Catal.* **2017,** *7*, 706-709.

21. Issi. J. P. Low Temperature Transport Properties of Group V Semimetals *Aust. J. Phys.* **1979**, *32*, 585-628.

22. Jang, Y. J.; Choi, K.-S. Enabling electrochemical N_2 reduction to NH_3 in the low overpotential region using non-noble metal Bi electrodes via surface composition modification. *J. Mater. Chem. A.* **2020**, *8*, 13842-13851.

23. Di, L.; Chen, X.; Liu, Y.-T.; Yu, J.; Ding, B., Sb_2S_3 nanoparticles anchored on SnO_2 nanofibers: a high-performance hybrid electrocatalyst toward ammonia synthesis under ambient conditions. *Chem. Commun.* **2019,** *55*, 13892-13895.

24. Bat-Erdene, M.; Xu, G.; Batmunkh, M.; Bati, A. S. R.; White, J. J.; Nine, M. J.; Losic, D.; Chen, Y.; Wang, Y.; Ma, T.; Shapter, J. G., Surface oxidized two-dimensional antimonene nanosheets for electrochemical ammonia synthesis under ambient conditions. *J. Mater. Chem. A* **2020,** *8*, 4735-4739.

25. Liu, X.; Jang, H.; Li, P.; Wang, J.; Qin, Q.; Kim, M. G.; Li, G.; Cho, J., Antimony-Based Composites Loaded on Phosphorus-Doped Carbon for Boosting Faradaic Efficiency of the Electrochemical Nitrogen Reduction Reaction. *Angew. Chem. Int. Edit.* **2019,** *58*, 13329-13334.

26. Montoya, J. H.; Tsai, C.; Vojvodic, A.; Nørskov, J. K., The Challenge of Electrochemical Ammonia Synthesis: A New Perspective on the Role of Nitrogen Scaling Relations. *ChemSusChem* **2015,** *8*, 2180-2186.

27. Wang, Q.; Zheng, G.; Hao, S.; Liu, X.; Zheng, J.; Wang, Y.; Su, Z.; Xu, N.; He, Y.; Lei, L.; Zhang, X., Au_1Co_1 Alloy Supported on Graphene Oxide with Enhanced Performance for Ambient Electrolysis of Nitrogen to Ammonia. *ACS Sustain. Chem. Eng.* **2020,** *8*, 44-49.

28. Zhang, Q.; Shen, Y.; Hou, Y.; Yang, L.; Chen, B.; Lei, Z.; Zhang, W. Composition-dependent electrochemical activity of Ag-based alloy nanotubes for efficient nitrogen reduction under ambient conditions. *Electrochim. Acta* **2019,** *321*, 134691.

29. Pang, F.; Wang, Z.; Zhang, K.; He, J.; Zhang, W.; Guo, C.; Ding, Y., Bimodal nanoporous Pd_3Cu_1 alloy with restrained hydrogen evolution for stable and high yield electrochemical nitrogen reduction. *Nano Energy* **2019,** *58*, 834-841.

30. Yu, H.; Wang, Z.; Yang, D.; Qian, X.; Xu, Y.; Li, X.; Wang, H.; Wang, L., Bimetallic Ag_3Cu porous networks for ambient electrolysis of nitrogen to ammonia. *J. Mater. Chem. A* **2019,** *7*, 12526-12531.

31. Andersen, S. Z.; Čolić, V.; Yang, S.; Schwalbe, J. A.; Nielander, A. C.; McEnaney, J. M.; Enemark-Rasmussen, K.; Baker, J. G.; Singh, A. R.; Rohr, B. A.; Statt, M. J.; Blair, S. J.; Mezzavilla, S.; Kibsgaard, J.; Vesborg, P. C. K.; Cargnello, M.; Bent, S. F.; Jaramillo, T. F.; Stephens, I. E. L.; Nørskov, J. K.; Chorkendorff, I., A rigorous electrochemical ammonia synthesis protocol with quantitative isotope measurements. *Nature* **2019,** *570*, 504-508.

32. Watt, G. W.; Chrisp, J. D., Spectrophotometric Method for Determination of Hydrazine. *Anal. Chem.* **1952,** *24*, 2006-2008.

33. Higgins, D.; Hahn, C.; Xiang, C.; Jaramillo, T. F.; Weber, A. Z., Gas-Diffusion Electrodes for Carbon Dioxide Reduction: A New Paradigm. *ACS Energy Lett.* **2019,** *4*, 317-324.

34. Mccarthy J. A. and the United States Steel Corp **1962**, Method of electroplating bismuth on steel and electrolyte therefor, US3256160A.

35. Berger, J.; Christ, B.; Troschke, J., Lattice Parameter Study in the $Bi_{1-x}Sb_x$ Solid-solution System. *Crystal Res. & Technol.* **1982**, *17*, 1233-1239.

36. Pauling, L., The Nature of the Chemical Bond, Third Edition, Cornell University Press, Ithaca, New York, 1960.

37. Giessen, B.; Wolff, U.; Grant, N., Metastable simple cubic phases based on antimony and bismuth. *TRANS MET SOC AIME* **1968,** *242*.

38. Jurriaanse, T., The Crystal Structure of Au_2Bi. *Z Krist-Cryst. Mater.* **1935,** *90*, 322-329.

39. Mozharivskyj, Y.; Pecharsky, A. O.; Bud'ko, S.; Miller, G. J., A Promising Thermoelectric Material: Zn_4Sb_3 or $Zn_{6-\delta}Sb_5$. Its Composition, Structure, Stability, and Polymorphs. Structure and Stability of Zn_1-δSb. *Chem. Mater.* **2004,** *16*, 1580-1589.

40. Boström, M.; Lidin, S., The incommensurably modulated structure of ζ-$Zn_{3-x}Sb_2$. *J. Alloy. Compd.* **2004,** *376*, 49-57.

41. Kainzbauer, P.; Richter, K. W.; Ipser, H., Experimental Investigation of the Binary Mn-Sb Phase Diagram. *J. Phase. Equilib.* **2016,** *37*, 459-468.